TIME-DOMAIN ELECTROMAGNETIC IMAGING OF COASTAL AQUIFERS AT MALTA AND NEW ZEALAND WITH IMPLICATIONS FOR THEIR ONSHORE-OFFSHORE CONNECTIVITY

A Dissertation

by

POTPREECHA PONDTHAI

Submitted to the Office of Graduate and Professional Studies of
Texas A&M University
in partial fulfillment of the requirements for the degree of

DOCTOR OF PHILOSOPHY

Chair of Committee,	Mark E. Everett
Committee Members,	Peter S. Knappett
	David W. Sparks
	Niall Slowey
Head of Department,	Julie Newman

December 2020

Major Subject: Geophysics

ABSTRACT

Several studies documented in the geophysics literature have applied the time-domain electromagnetic (TDEM) method for coastal and marine aquifer characterization, and for environmental and hydrological investigations. By imaging the subsurface conductivity (or its reciprocal, resistivity), the electromagnetic (EM) methods provide information about spatial variations in geomaterial properties. The main objective of this dissertation is to enhance the capability of terrestrial TDEM geophysical methods employing a controlled-loop source for onshore-offshore groundwater connectivity investigations. I developed 2D and 3D forward modeling capabilities based on finite-element (FE) analysis to show that TDEM responses can provide constraints on the geometry of the onshore freshwater body and potential flow paths offshore. Two case studies, from Malta and New Zealand respectively, are presented herein. TDEM responses have been acquired with the Geonics G-TEM instrument and used to map the geometry of the mean sea-level aquifer (MSLA) in SE Malta. A similar method is used to interpret data acquired inland at the top of the sea cliffs and along the beach at Canterbury coast, South Island of New Zealand. Forward modeling of the TDEM data based on FE algorithm is utilized to generate geoelectrical models that can be used to better understand the coastal hydrology. The subsurface geometry of the onshore freshwater body within the MSLA along the SE Malta coast is identified from 2D and 3D EM forward modeling results. In a similar manner, the utility of the TDEM geophysical method along with forward modeling demonstrates the connections between groundwater conduits and the coastal gullies in terms of directing freshwater discharge offshore along the mid Canterbury coast. This EM imaging technique has the capability of solving this similar types of problems in the other places to provide valuable information for future water management of the groundwater reserves.

DEDICATION

To Naulprang, Pattarawadee

Thitima, and

Sutthiluck.

ACKNOWLEDGMENTS

I would first and foremost like to express my gratitude to my commitee chair, Dr. Mark Everett, for his support, encouragement, and patience since day one. Without him this success would not be possible. In addition, I would like to thank my committee members Dr. David Sparks, Dr. Peter Knappett and Dr. Niall Slowey for their valuable time and guidance throughout the course of this research. I must express my gratitude to entire Geology and Geophysics Department, whose shapes me who I am today.

I am very grateful to Dr. Aaron Micallef, Dr. Bradley Weymer, Dr. Amir Haroon, Dr. Marion Jegen, and Zahra Faghih from GEOMAR for their kind assistance on fieldworks and manuscripts.

I do appreciate Dr. Angel Glover and Dr. Ben Spears from TAMU Counseling & Psychological Services, Megan Cullers and Tiffany Skaggs from TAMU Student Health Services for helping me get through hard times.

CONTRIBUTORS AND FUNDING SOURCES

Contributors

This work was supported by a dissertation committee consisting of Professor Mark Everett [advisor] and Professors David Sparks and Associate Professor Peter Knappett of the Department of Geology and Geophysics and Professor Niall Slowey of the Department of Oceanography.

Funding Sources

Graduate study was supported by Development and Promotion of Science and Technology Talents Project (DPST), Royal Thai Government.

Travel supports were received from Howard Karren Professorship.

This research has partially received funding from the European Research Council (ERC) under the European Union's Horizon 2020 research and innovation programme (grant agreement No 677898 (MARCAN).

NOMENCLATURE

EM	Electromagnetic
TEM	Transient Electromagnetic
TDEM	Time-Domain Electromagnetic
EMI	Electromagnetic Induction
emf	electromotive force
TX	Transmitter
RX	Receiver
GPR	Ground-Penetrating Radar
ERT	Electrical Resistivity Tomography
DEM	Digital Elevation Model
MSLA	Mean Sea-Level Aquifer
LCL	Lower Coralline Limestone
OFG	Offshore Freshened Groundwater
OA	Offshore Aquifer
FE	Finite-Element
FV	Finite-Volume

TABLE OF CONTENTS

Page

LIST OF FIGURES

FIGURE Page

LIST OF TABLES

TABLE Page

1. INTRODUCTION

1.1 Offshore Freshwater Aquifers

Groundwater resources in many coastal regions worldwide are currently under stress because of increased population, tourism and economic growth. Offshore groundwater in such places is an alternative future resource that can help to mitigate the water stresses experienced by coastal communities [Post et al., 2013]. The population density in coastal zones is significantly higher than the global average and is rapidly increasing. Worldwide there are currently more than two billion people living within 100 km of a coastline [Stuart et al., 2010].

Lower sea levels during the last glacial maximum $\sim$19–22 ka, promoted the recharge of groundwater beneath the continental shelves. Moreover, surface water, precipitation and, in some areas, glacial meltwater discharged onto the shelf while it was subaerially exposed. The freshened groundwater drove saline groundwater further offshore (Figure 1.1a). When seawater is rising, the shelves are flooded during interglacials. As sea level rose during the latest subsequent interglacial periods, many of the formerly exposed shelves became submerged. Below sea level (Figure 1.1b), fine sediments (comprising an impermeable layer) deposited on the seafloor act as an aquitard to trap the freshened water underneath. Also during interglacials, intruding seawater migrates landward as well as downward as the supply of freshened groundwater diminishes. Sea level has been much lower than today for 80% of the Quaternary period (last 2.6 Ma). Since the landward migration of meteoric groundwater is generally outpaced by sea level rise, remnants of meteoric groundwater are found in many places offshore [Post et al., 2013, Michael et al., 2016].

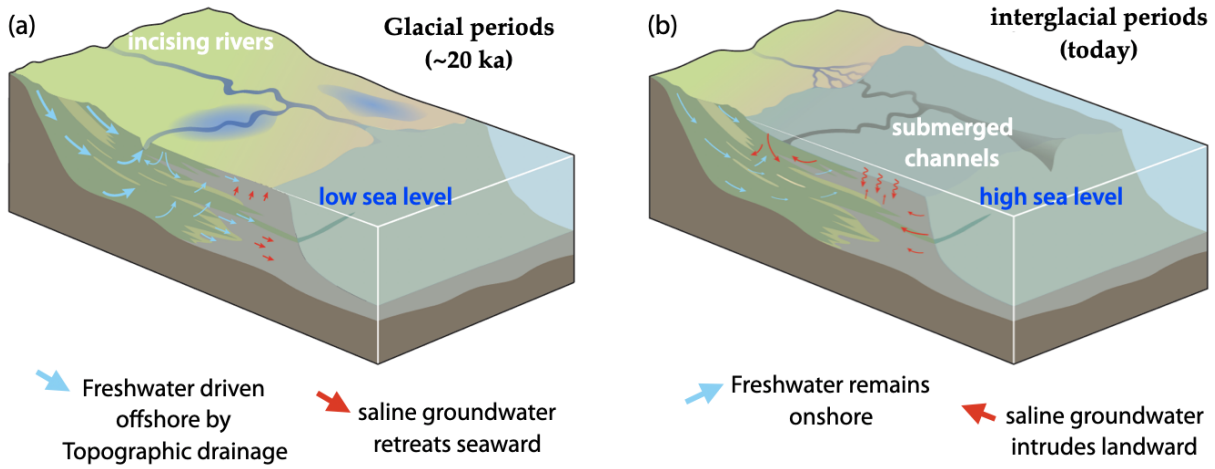

Figure 1.1: Conceptual model of geology, groundwater flow and dissolved salt transport processes below the continental shelf. (a) glacial and (b) interglacial periods. Modified after Post et al. [2013].

The definition of an offshore aquifer (OA) is given by Post et al. [2013] as a groundwater body with a minimum horizontal extent of 10 km, and maximum total dissolved solids $<$10 g/l ($\sim$1/3 of sea water salinity). There are two principal types of OAs (Figure 1.2). Active OAs contain a present-day, permeable connection of offshore to terrestrial aquifer recharged by precipitation [Taniguchi et al., 2002, Bratton, 2010]. Such aquifers tend to be wedge-shaped, becoming thinner and more saline with increasing distance from the coast. On the other hand, inactive OAs comprise offshore groundwater systems that are associated with paleo-groundwater (fossil groundwater) and are no longer recharged by meteoric water. Inactive OAs may result from an insufficiency of terrestrial hydraulic head to push water offshore [Kooi and Groen, 2001] or the absence of a hydraulic connection to an onshore aquifer [Person et al., 2003].

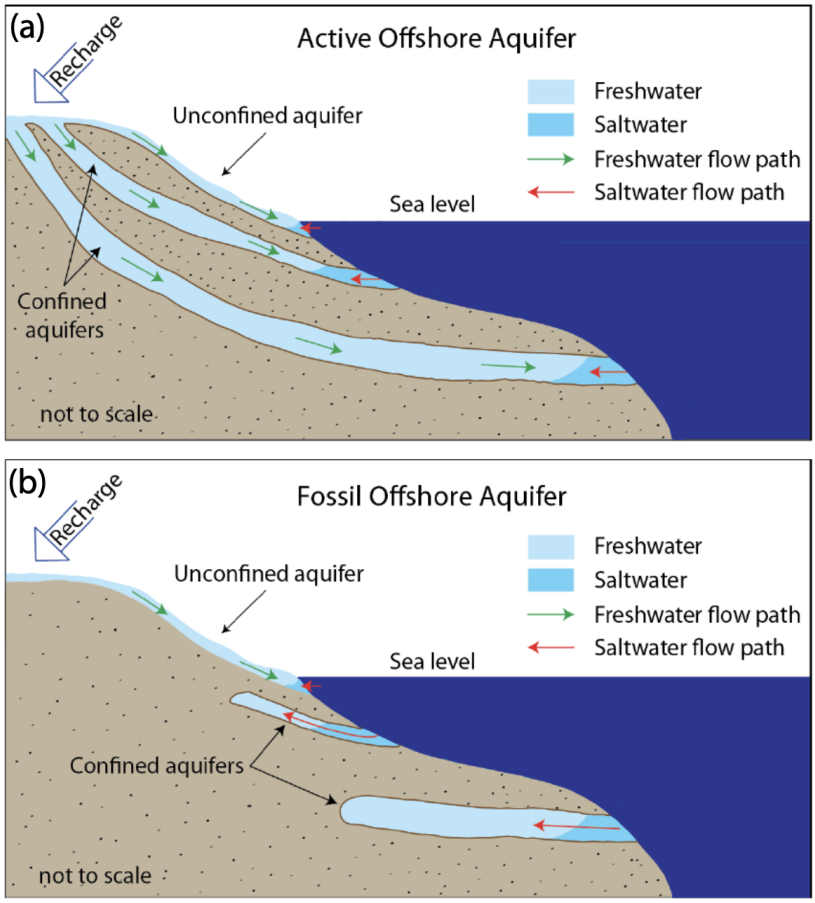

Figure 1.2: Conceptual model illustrating differences between (a) offshore freshened groundwater (connected, or active); and (b) paleo-groundwater (disconnected, or fossil) system. Active aquifers are recharged by meteoric water (green arrows). Fossil aquifers are no longer recharged by precipitation and are susceptible to saltwater intrusion (red arrows). Reprinted from Weymer et al. [2020] with permission.

Onshore-offshore aquifer connectivity in coastal areas, if it can be demonstrated, would have important implications for water scarcity mitigation and sustainable exploitation of offshore groundwater reserves. Connectivity remains poorly understood however due to: 1) barriers across disciplines that inhibit interdisciplinary research [Talley et al., 2003]; 2) difficulty with integrating geophysical and geochemical methods of characterizing groundwater systems across the coastal transition zone [Post, 2005]; and 3) the lack of appropriate technologies to map and quantify zones of freshwater flow offshore [Post, 2005, Evans, 2007], especially in the nearshore environment.

Currently, it is difficult to determine fluxes of groundwater discharge to the sea. Apart from the uncertainties about possible onshore-offshore connections, there is a general lack of information regarding location and geometry of coastal aquifer systems. However, a few recent attempts have been made by employing offshore geophysical methods, such as marine controlled-source electromagnetics (mCSEM) [Gustafson et al., 2019, Micallef et al., 2020]. The mCSEM technique, which maps bulk electrical resistivity beneath the seafloor, provides a means to guide geochemical sampling, and ultimately to inform hydrogeological modelling efforts that aim to quantify the evolution of coastal groundwater systems in response to changing sea level and for the purpose of possible extraction [Weymer et al., 2020].

Marine hydrogeologists have known about the existence of offshore freshwater aquifers since the mid 1970's [Hathaway et al., 1979]. However, ownership and sovereign control of this seabed resource remains ambiguous. Traditionally, the distribution of natural resources is a right that is closely linked with sovereign claims to the resource. There are no generally agreed-upon rules or guidelines for managing offshore freshwater reserves, but by the Law of the Sea (LOSC) and custom, each coastal state is granted exclusive sovereign rights over seabed natural resources that are located within its exclusive economic zone, which includes the continental shelf. Offshore aquifers may however transcend political boundaries but LOSC does not address transboundary resources (including offshore groundwater). The resulting "governance gap" for equitable distribution could be filled by legal claims but also it could be filled by the ethical argument that water should be shared since it is an exceptional resource due to its a life-sustaining properties [Martin-Nagle, 2020]. In the future, as offshore freshwater becomes appropriated for use, technologies developed for offshore hydrocarbon development can be adapted for extraction and transportation of freshwater.

1.2 Time-Domain Electromagnetic Method for Groundwater Exploration

Early attempts to use the transient electromagnetic or time-domain electromagnetic (TEM or TDEM) geophysical method for groundwater applications were made in the 1980's. Ground-based TDEM soundings were carried out to map the freshwater/saltwater interface in coastal aquifers in

Florida and Massachusetts [Stewart and Gay, 1983, Fitterman and Hoekstra, 1984]. Fitterman and Stewart [1986] and Fitterman [1987] provide good overviews of the TDEM method for groundwater explorations. In those papers, elementary numerical approaches were used for modeling the TDEM responses of several groundwater scenarios, e.g., mapping of alluvial fill over bedrock, estimating depths to the water table in an alluvium-filled basin, mapping of sand and gravel lenses in unsorted sediment, and detection of the salt-freshwater interface in a coastal aquifer. At that time, the TDEM technique was mainly used for locating deeper (>50 m) targets such as ore bodies because of its high sensitivity to good conductors [Kaufman et al., 1983].

There have been a number of more recent studies using the geophysical TDEM method for investigating groundwater and mapping freshwater aquifers. For example, Meju et al. [2000] carried out shallow-depth TEM soundings coincident with borehole locations to map the hydrogeological conditions under glacial drift deposits. They deployed 20, 40 and 50 m^2 square transmitter (TX) loops with the central-loop receiver (RX) configuration using Geonics PROTEM 47 equipment to reach a penetration depth 150 m. The resistivity depth-profiles obtained by their inversion of the TEM soundings helped to visualize the aquifer formation and overlying sedimentary rocks and moreover the information turned out to be well-correlated with the borehole data.

Auken et al. [2003] and Denielson et al. [2003] developed a new TDEM technique, namely the Pulled Array TEM (PATEM) system that can provide high data density and increased lateral resolution of the subsurface resistivity structure. A large-scale PATEM sounding survey covering more than 500 km in length was performed using a 40×40 m^2 transmitter loop. The survey was performed in order to map the spatial distribution of resistivity and estimate the depth to a water-bearing formation. To map deep-seated aquifers up to 300 m depth, the High Moment TEM (HiTEM) system was developed [Sørensen and Auken, 2004]. More than 2000 HiTEM soundings acquired in different geological settings in Denmark were used to study the electromagnetic coupling between natural hydrogeological formations and man-made conductors.

Porsani et al. [2012] deployed the TDEM technique to map sedimentary and crystalline aquifers within an urban setting in Brazil. The surveys help to delineate both these types of

aquifers. The study area was characterized by a fracture zone wherein conductive zones at the base of the sedimentary sequence were indicative of water-saturated basement rocks. The results are in good agreement with local geology obtained from lithological boreholes located in the study area. This study opened new perspectives for TDEM-method use in urban environments.

1.2.1 Recent TDEM Method for Coastal Seawater Intrusion Identification

Several studies documented in the geophysics literature have applied the TDEM method to investigate coastal aquifers. By imaging the subsurface conductivity (or its reciprocal, resistivity), electromagnetic (EM) methods provide information about spatial variations in geomaterial properties. Inversions of TDEM soundings for 1D and 2D earth structures have now been widely performed for the purpose of coastal and marine aquifer characterization. Some of the studies that have detected evidence of seawater intrusion in coastal aquifers using TDEM methods are described in the following paragraphs.

Herckenrath et al. [2013] performed a coupled hydrogeophysical inversion, in which a saltwater intrusion hydrological model was used to guide the geophysical data interpretation. The method was designed to mitigate errors caused by the inconsistent spatial scales of geophysical and hydrologic models. The coupled Hydrogeophysical Inversion-State (CHI-S) method enables an electrical resistivity model to be constructed based on converting simulated salt concentrations, after which a geophysical forward response is calculated and compared to the measured geophysical data. The approach was applied to a TDEM dataset collected from a field site in Santa Cruz County, California. A 2D cross-sectional saltwater intrusion model was developed based on the estimated hydrological, geophysical, petrophysical parameters.

El-Kaliouby and Abdalla [2015] carried out TDEM soundings using a Geonics PROTEM 47 system with a 20 m$\times$ 20 m single-turn TX loop. The study area was the coast of the Gulf of Oman and the aims of the survey were to determine the extent of seawater intrusion and to map a shallow alluvial aquifer. The TDEM method in the study area proved to be successful in mapping the fresh/saline water interface and locating the depth of a freshwater aquifer. The depth and inland extent of the saline zone were mapped along shore-perpendicular profiles. The TDEM-inferred

depths to the freshwater table and saline interface turned out to be compatible with available well data.

Martínez-Moreno et al. [2017] combined two geophysical techniques, electrical resistivity tomography (ERT) and TDEM soundings, to examine seawater intrusion within the Ferragudo Albufeira aquifer system of southern Portugal. The models they obtained by a 1D joint inversion improved upon preliminary results from separate inversions of the ERT and TDEM data. The sedimentary layers and seawater intrusion appear to be better resolved by the joint inversion. A quasi-2D joint inversion, creating an image of the subsurface resistivity distribution, provides a more realistic geometry of the seawater intrusion and it is able to distinguish some of the sedimentary layers that were recognized in nearby exploration drilling.

Kalisperi et al. [2018] investigated the Geropotamos aquifer that is located on the coast of Crete, an island belonging to Greece. The authors deployed a survey grid that included 1179 TEM soundings at 372 sites to delineate zones of salination of groundwater within the aquifer (see Figure 1.3). The 1D and 2D inversion results based on the TEM soundings are in agreement with geological mapping, hydro-lithological data and geochemical analysis. The authors suggest that the aquifer is degraded by saline intrusion, which likely occurs along fractures that are associated with a fault zone.

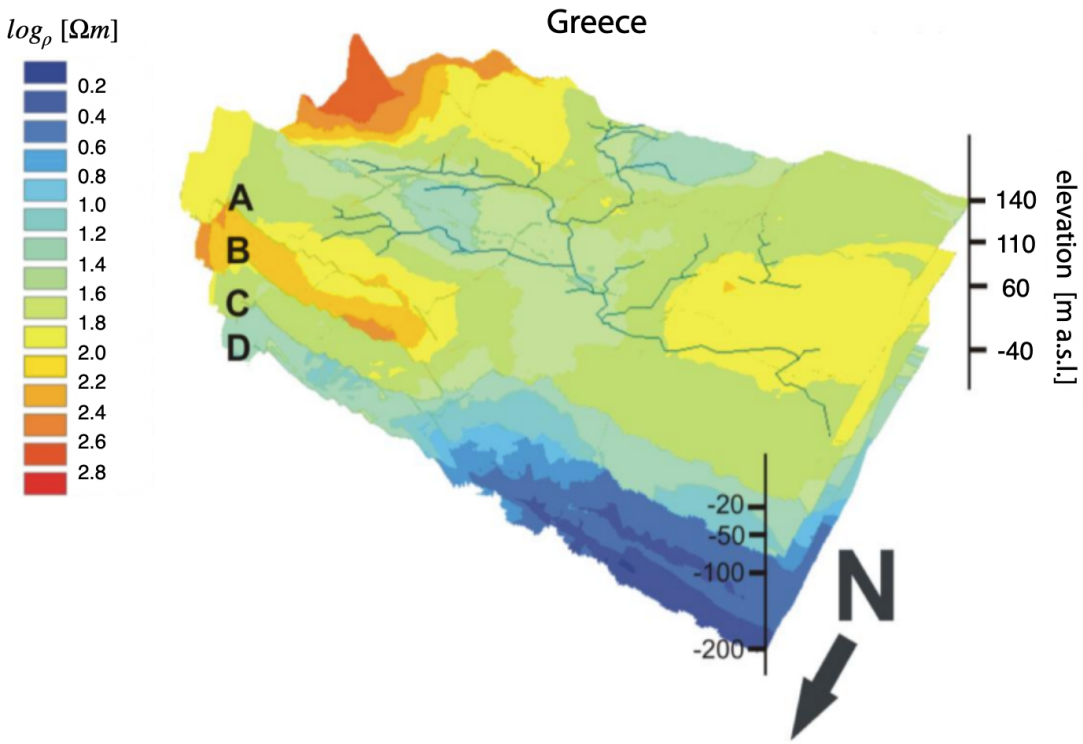

Figure 1.3: The extracted resistivity slices A, B, C and D from north-central Crete, Greece; zones of low resistivity associated with the location of the coastal area. Four resistivity layers, which obtained from interpolation of TEM resistivity values at different depth ranges, include Layer A (0–20 m) Layer, B (20–50 m), Layer C (50–100 m), and Layer D (100–200 m). Modified after Kalisperi et at. [2018].

Torres-Martinez et al. [2019] deployed TDEM surveys using Sirotem-S equipment, with a single-turn TX loop of 150×150 m^2 area, reaching a maximum investigation depth of 500 m. The inverted TEM soundings from a total of 50 locations (1D models) were interpolated to generate resistivity depth-slices at different depths. This procedure provided a good spatial coverage of the subsurface electrical distribution over the aquifer of La Paz in Baja California, Mexico. Subsequently, the resistivity maps were used to refine the original geological model and to construct a 3D density-dependent fluid flow model in order to better understand seawater intrusion into the aquifer. The results confirm that a large cone of depression has formed due to excessive pumping by the agricultural sector over the last few decades. The groundwater abstraction has led to a reversal of the hydraulic gradient and seawater intrusion advancement on the order of 6–8 km inland,

especially in the north-central portion of the aquifer.

1.2.2 Recent TDEM Studies of Coastal and Marine aquifer characterization

Nielsen et al. [2007] carried out 96 transient electromagnetic soundings covering an area of 1 km$\times$2.5 km over a portion of Keta Barrier in Ghana to map the freshwater lens and saltwater-freshwater interface. They deployed a central-loop configuration using the Geonics PROTEM 47 instrument with 40$\times$40 m square TX loop. Three dynamic ranges of the transient decay of secondary magnetic field were recorded by the RX coil in the standard 20 time-gate mode, namely ultra high (237.5 Hz), very high (62.5 Hz) and high range (25 Hz). Interpretation of the inversion results suggests that the fresh water lens reaches 24 m in maximum thickness. The inverted models show that the top of the saltwater-saturated sediments at 0–5 m depth attain low resistivity $\sim$1 Ωm. A mixing zone of brackish water is identified at various depths between the top layer of the saltwater-saturated sediments and the overlying freshwater lens.

Ezersky and Frumkin [2017] investigated groundwater salinity throughout the Dead Sea coastal area of Israel and Jordan in order to evaluate the aquifer salinity for future water management. A total of 28 TEM soundings along the Dead Sea coast were carried out close to observation boreholes. The latter enabled a calibration of the TEM-inferred bulk resistivity with borehole-measured salinity readings. Quantitative relationships between bulk resistivity, formation water resistivity and chloride concentration were derived based on Archie equations, all within the resistivity range of order 1 Ωm. This procedure enabled a determination of the bulk salinity of the aquifer. The results showed that the Dead Sea aquifer has bulk resistivity in the range of 0.55–1.0 Ωm containing brine with 50–110 $g_{chloride}$/liter and 22–50% saturation. Average values of the effective porosity of 0.32 and 0.44 were found for sandy and silty sediments, respectively.

Lippert and Tezkan [2019] carried out multicomponent long-offset transient EM measurements offshore Israel. They deployed a long grounded dipole as transmitter and established several electric and magnetic receivers on the sea floor up to $\sim$5 km from the coast. They present 1D Occam and Marquardt inversions of measurements of the offshore horizontal broadside and inline electric field components, in addition to the vertical broadside magnetic component. The results (see

Figure 1.4) demonstrate that an Israeli submarine coastal aquifer extends offshore to a distance of ∼3.25 km.

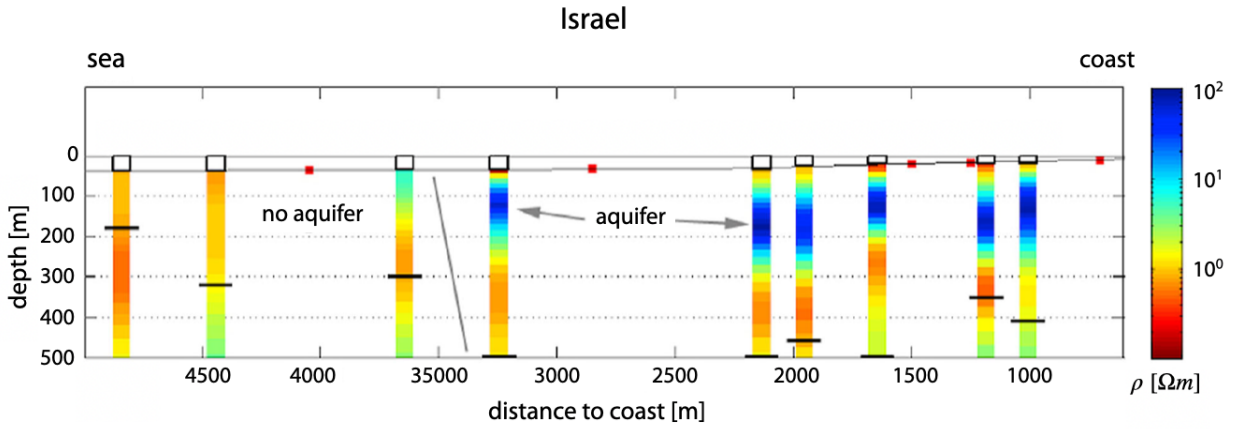

Figure 1.4: Merged 2D profile from Occam 1D inversions of the broadside horizontal electric fields at the Palmahin disturbance, Israel. The aquifer is clearly visible as a poor conductor of resistivity ∼80 Ωm and it extends from the coast to a distance of 3250 m. The data from receiver position at 3650 m clearly shows the absence of the aquifer at that location. Modified after Lippert and Tezkan [2019].

1.3 3D Modeling for other Geophysical Applications

Mathematical formulations for the numerical implementation of 3D EM forward-modeling in the frequency domain based on finite-element (FE) and finite-volume (FV) approaches have recently been developed in the geophysical literature [Ansari and Farquharson, 2014, Jahandari and Farquharson, 2014].

An adaptive edge-based FE algorithm has been applied to frequency-domain marine CSEM modeling to study the responses of an anisotropic medium [Li et al., 2020]. The edge-based FE method adopts vector basis functions defined on the centers of elements instead of using scalar basis functions defined on element nodes as per the conventional node-based algorithm. The advantage of the edge-based 3D algorithm is that it can model anisotropic seafloor sedimentary sequences and other complex model geometries. The algorithm included a capability for unstructured

tetrahedral grids. The algorithm is validated against the quasi-analytic solution for an anisotropic 1D layered model. The authors then calculate mCSEM responses over a suite of 3D anisotropic models, with the results suggesting that azimuthal anisotropy has a considerable influence on both the inline and broadside responses. Azimuthal anisotropy is generated by the variation in azimuth of a horizontal transverse isotropic medium. The inline direction refers to a survey traverse line that is aligned in the same direction with the line connecting the TX and RX, while the broadside direction is defined by the line joining the TX and RX being perpendicular to the survey traverse direction.

Much of the development of 3D forward modeling for TDEM data, specifically with the loop-source configuration, has occurred within the field of mineral exploration. Examples include applying 3D TDEM forward codes to investigate electromagnetic responses of models that can capture the complex geometry of ore bodies and fault systems. The 3D forward modeling in these studies is largely based on FE analysis [Li et al., 2017, Li et al., 2018]. The combined approach of a vector FE formulation with local mesh refinement techniques near TXs and Rxs provides the capacity to handle realistic models with complex TX loop geometry and irregular topography. This approach has been used to develop 3D forward modeling for moving-loop configurations, with application to the Ovoid Zone massive sulfide deposit, Canada. The authors found that a combination of local refinement of an unstructured tetrahedral mesh with an accurate time-stepping scheme reduces to less than 3% the relative error between the computed FE time-domain responses and analytic solutions.

A complicated geological setting, including the conductive features of graphitic fault systems, in the Athabasca Basin, Canada were modeled using a 3D finite-volume TDEM formulation [Lu, 2020]. In order to model the TDEM problem, two numerical methods were used, namely the electric-field and the potential approaches. The electric field method directly solves the electric field Helmholtz equation, while the potential method solves the Helmholtz equation formulated in terms of vector and scalar potentials. The developed methods with unstructured grids are then applied to the TDEM modeling of acquired electromagnetic data from Athabasca Basin. The mod-

eling results illuminate thin, steeply dipping fault systems associated with uranium deposits in the study area.

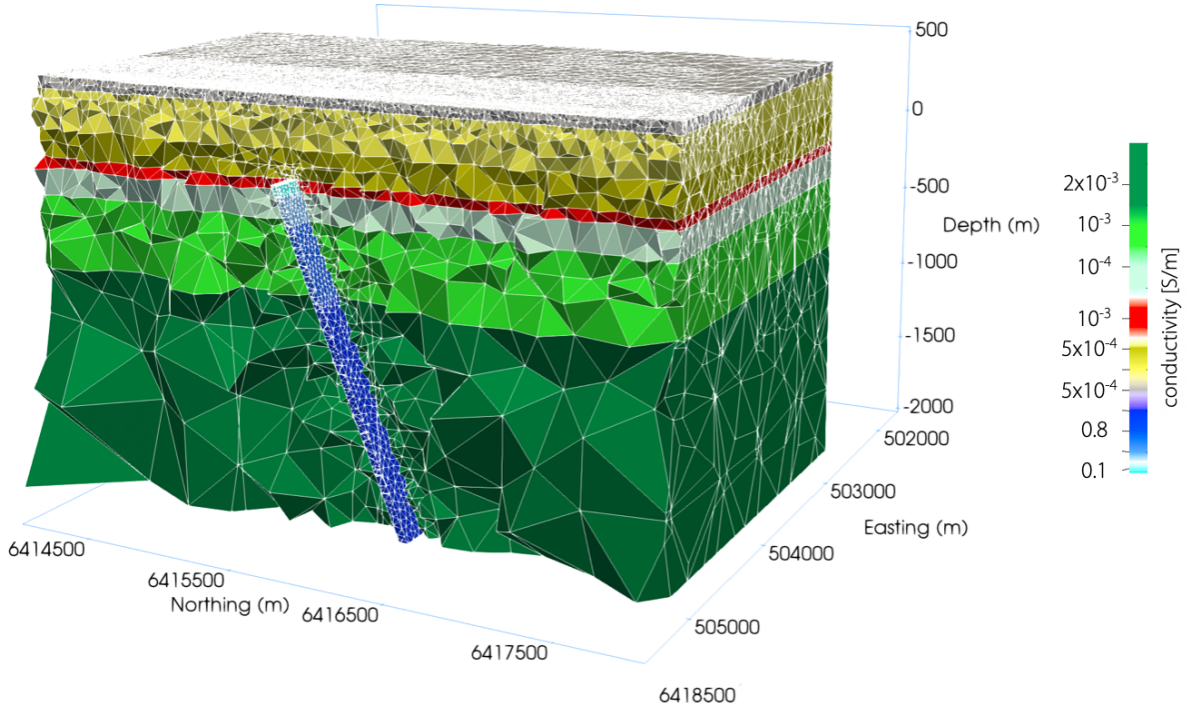

Figure 1.5: An unstructured mesh used for 3D TDEM modeling that includes a steep–dipping fault marked as the cyan/blue prism in the center of model. Modified after Lu [2020].

1.4 Purpose of the Study

The main objective of my dissertation is to enhance the capacity of terrestrial time-domain electromagnetic geophysical methods for investigation of onshore-offshore groundwater connectivity. I have developed 2D and 3D forward modeling capabilities based on finite-element (FE) analysis to show that TDEM responses can provide constraints on the geometry of the onshore freshwater body along with potential flow paths offshore. Two case studies, from Malta and New Zealand respectively, are presented. Time-domain electromagnetic (TDEM) responses have been acquired with the Geonics G-TEM instrument and used to map the geometry of the mean sea-level

aquifer in SE Malta. A similar method is used to interpret data acquired inland at the top of the sea cliffs and along the beach at Canterbury coast, South Island of New Zealand. Forward modeling of the TDEM data is performed to generate geoelectrical models that can be used to better understand the coastal hydrology. My work helps to characterize the valuable groundwater resources of the semi-arid, rapidly urbanizing island of Malta. Using a similar approach at New Zealand, my work has permitted a detailed evaluation of the connections between groundwater conduits and the coastal gullies in terms of directing large quantities of freshwater discharge offshore.

1.5 Outline of Dissertation

The structure of this dissertation is as follows. Chapter 2 focuses on the development of TDEM methods to map the hydrological structure of the mean sea-level aquifer along the southeastern coast of the island of Malta. In particular, 2D and 3D TDEM forward modeling are used to constrain and identify the subsurface geometry of the onshore freshwater body. Chapter 3 explores possible scenarios for groundwater discharge based on forward modeling of my field geophysical observations along the mid Canterbury coast, New Zealand. The 2D EM imaging technique visualizes the spatial geoelectrical heterogeneity, which are likely indicative of groundwater flow paths and/or associated with location of coastal gullies beneath the Canterbury plains. Chapter 4 contains work that I have contributed as a co-author to two submitted manuscripts on onshore-offshore aquifer connectivity. Chapter 5 discusses the overall findings from my research and provides suggestions for future work.

2. 3D CHARACTERIZATION OF A COASTAL FRESHWATER AQUIFER IN SE MALTA (MEDITERRANEAN SEA) BY TIME-DOMAIN ELECTROMAGNETICS

All contents in this chapter are from the article[1] published in open-access journal *Water*: Special Issue "Applied Geophysics in Hydrological Practice".

2.1 Abstract

Electromagnetic (EM) geophysical methods are well equipped to distinguish electrical resistivity contrasts between freshwater-saturated and seawater-saturated formations. Beneath the semi-arid, rapidly urbanizing island of Malta, offshore groundwater is an important potential resource but it is not known whether the regional mean sea-level aquifer (MSLA) extends offshore. To address this uncertainty, land-based alongshore and across-shore time-domain electromagnetic (TDEM) responses were acquired with the G-TEM instrument (Geonics Ltd., Mississauga, Ontario, Canada) and used to map the onshore structure of the aquifer. 1-D inversion results suggest that the onshore freshwater aquifer resides at 4–24 m depth, underlain by seawater-saturated formations. The freshwater aquifer thickens with distance from the coastline. We present 2D and 3D electromagnetic forward modeling based on finite-element (FE) analysis to further constrain the subsurface geometry of the onshore freshwater body. We interpret the high resistivity zones that as brackish water-saturated bodies are associated with the mean sea-level aquifer. Generally, TDEM results provide valuable onshore hydrogeological information, which can be augmented with marine and coastal transition-zone measurements to assess potential hydraulic continuity of terrestrial aquifers extending offshore.

Keywords: coastal hydro-geophysics; groundwater; mean sea-level aquifer; transient electromagnetics

[1]Reprinted with permission from Pondthai, P., Everett, M. E., Micallef, A., Weymer, B. A., Faghih, Z. Haroon, A. & Jegen, M. (2020). 3D Characterization of a Coastal Freshwater Aquifer in SE Malta (Mediterranean Sea) by Time-Domain Electromagnetics. *Water. 12(6)*, 1566. doi:10.3390/w12061566.

2.2 Introduction

Groundwater resources in many coastal regions worldwide are currently under stress because of increasing population, agricultural demands, tourism and economic growth. Fresh groundwater in coastal regions may be a resource that can help to mitigate the water scarcity experienced by coastal communities [Post et al., 2013]. However, several first-order questions need to be addressed before the fresh groundwater can be used sustainably. These include a lack of understanding regarding the location, nature, geometry of coastal aquifer systems and their offshore connectivity. Large-scale desalination of seawater is a technologically viable solution, but there are important energy and environmental impacts that must be considered [Jones et al., 2019]. Terrestrial time-domain electromagnetic (TDEM) methods of geophysical exploration employing a loop or grounded dipole source can be used to explore the onshore component of coastal aquifers that may extend offshore. TDEM methods are useful because they have good depth penetration in saline environments compared to other geophysical techniques, such as ground-penetrating radar (GPR) and electrical resistivity tomography (ERT). TDEM methods are sensitive to electrical resistivity which, in turn, is diagnostic of important aquifer parameters such as porosity, water saturation and salinity [Archie, 1942]. Transient EM methods respond to the interaction between an applied time-varying magnetic flux and the geoelectrical structure beneath the transmitter.

In order to interpret transient electromagnetic responses, the key physical mechanism is the induction process governed by Faraday's law, which is equivalent to diffusion into a conducting medium of an image of the transmitter (TX) loop current. A fundamental overview of the physical principles underlying the electromagnetic (EM) geophysical method is given elsewhere [Nabighian and Macnae, 1991, Everett and Chave, 2019b], and there are many reviews related to near-surface applications of EM techniques, e.g., [Everett, 2012, Fitterman, 2015]. The TDEM method has been widely used for groundwater studies [Fitterman and Stewart, 1986, Kafri et al., 1997, Danielsen et al., 2003, Siemon et al., 2009, Costabel et al., 2017, Yogeshwar and Tezkan, 2017, Kalisperi et al., 2018], including coastal aquifer characterization. The EM methods distinguish electrical conductivity contrasts between

freshwater-saturated or brackish-water saturated formations (resistivity $\sim$10–100 Ωm, or more) and seawater-saturated formations (resistivity $\sim$1–10 Ωm). A hydraulic connection implies a continuous hydraulic pathway beneath the coastal zone, such that an offshore aquifer could be recharged by its onshore counterpart, or depleted by pumping of its onshore counterpart. Terrestrial EM geophysical surveys can provide valuable information about the existence of such connections. This knowledge is important if we are to ensure the long-term sustainability of groundwater resources and it can serve as a valuable constraint for hydrogeological modeling studies. Onshore-offshore connectivity also has implications for possible onshore land subsidence due to offshore drilling and extraction [Morgan et al., 2018, Yu and Michael, 2019]. It should also be noted that the electromagnetic method remains largely undeveloped for data acquisition in the important coastal shallow-water transition zone.

This study is a part of a multi-disciplinary project that aims to investigate potential onshore-offshore groundwater aquifer connections based on terrestrial and offshore TDEM geophysical data from SE Malta (Mediterranean Sea). Here we utilize 2D and 3D electromagnetic forward modeling based on finite-element (FE) analysis to constrain the 3D geometry of the onshore freshwater body, in this case, the mean sea-level aquifer in SE Malta. To accomplish this objective, TDEM responses were acquired with the Geonics G-TEM instrument. The analysis of the TDEM data generated geoelectrical models that are used to better understand the variable coastal hydrogeology along a short segment of the Maltese coastline. This helps to characterize the potential groundwater resources of the semi-arid, rapidly urbanizing island of Malta. Future work, currently in the planning stages, will involve conducting additional EM measurements in both offshore and within the coastal transition zone.

2.3 Characterization of mean sea-level aquifer and study area

The Maltese Islands, comprising of Malta, Gozo and Comino, are composed of marine sedimentary rocks deposited between the Late Oligocene and Late Miocene epochs [Pedley et al., 1976]. The five sedimentary formations outcropping across the Maltese Islands include, from top to bottom: Upper Coralline Limestone (162 m), Greensand (11 m), Blue Clay

(75 m), Globigerina Limestone (207 m), and Lower Coralline Limestone (up to 1 km, of which the top $\sim$140 m is exposed) (numbers in brackets denote maximum thickness) see Figure 2.1a [Micallef et al., 2013, Directorate, 1993]. This succession contains a range of lithologies and facies, but overall it is dominated by marine carbonates of shallow water origin. The rock formations exhibit a gentle regional flexure and normal faulting is widespread [Illies, 1981]. The older (Early Miocene) and most widespread system of faults is oriented SW-NE and includes the Great Fault or Victoria Fault, which is $\sim$11 km long and traverses the entire width of the island. A younger system of faults (Late Miocene-Early Pliocene) is present along the southern coastline and often cross-cuts pre-existing faults. The longest of the younger faults is the NW–SE striking Maghlaq Fault. The climate of Malta is semi-arid Mediterranean characterized by a hot, dry summer and a mild, humid winter. The mean annual precipitation is 550 mm, which mainly falls between September to April [Galdies, 2011, FAO, 2006].

The Maltese Islands obtain $\sim$55% of their potable water supply from groundwater, while the rest comes from seawater desalination [FAO, 2006]. Aquifers are the primary source of portable water as there is no appreciable surface water streamflow. The mean sea-level groundwater body lies within the pores and fissures of Lower Coralline Limestone (LCL) in the interval where the formation subcrops at sea-level south of the Victoria fault [Stuart et al., 2010]. The LCL formation is predominantly composed of an algal fossiliferous limestone with sparse corals. The rocks exhibit moderate, irregular or channel-like permeability [MARSOL, 2016]. The primary porosity of LCL ranges between 7 and 20%, whereas its intrinsic permeability is low (10^{-7}-10^{-9} m/s). Effective porosity and secondary permeability, both of which are dependent on fissures and weathering, have values of 10–15% and 10^{-6} m/s [Stuart et al., 2010, Bakalowicz and Mangion, 2003]. The mean sea-level groundwater body is in lateral and vertical contact with seawater. A body of fresh water in the form of a 'lens' floats on saline water due to its lower density [Malta and Authority, 2011, Mangion and Sapiano, 2008]. The thicker part of the lens is situated in the central part of Malta, with its height decreasing towards the coastline. The mean-sea level groundwater is not at rest, but flows horizontally outward from the thickest part. The aquifer is

recharged by the infiltration of rainwater in every winter, and groundwater is either discharged offshore at the coastline or else removed by abstraction (pumpage) for agricultural purposes. The mean sea-level aquifer (MSLA) has a mean thickness of 67.5 m and covers an area of > 200 km^2 [BRGM, 1991]. This water is mainly abstracted for potable supply and agricultural use. A number of discontinuous perched aquifers with a limited saturated thickness occur north of the Great Fault in the Upper Coralline Limestone above the impermeable Blue Clay, and they are exclusively used for agricultural purposes.

The study site is situated on the SE coast of the island of Malta $\sim$6 km SE of Valletta, the capital city. The elevation of the study site is $\sim$10 m above the sea surface (see Figure 2.1a). The rocks exposed at the study site consist of the lower member of the Globigerina Limestone formation, which overlies the upper members of the LCL formation. There is a geological well at 3.5 km west of the study site that shows 35 m of Lower Globigerina above 34 m of Lower Coralline and the elevation of the well is 35 m [Malta and Authority, 2003]. There is another well drilled for hydrological purposes, located 2.5 km west of the study site, where the top of the water table is 1 m above sea level [Malta and Authority, 2011].

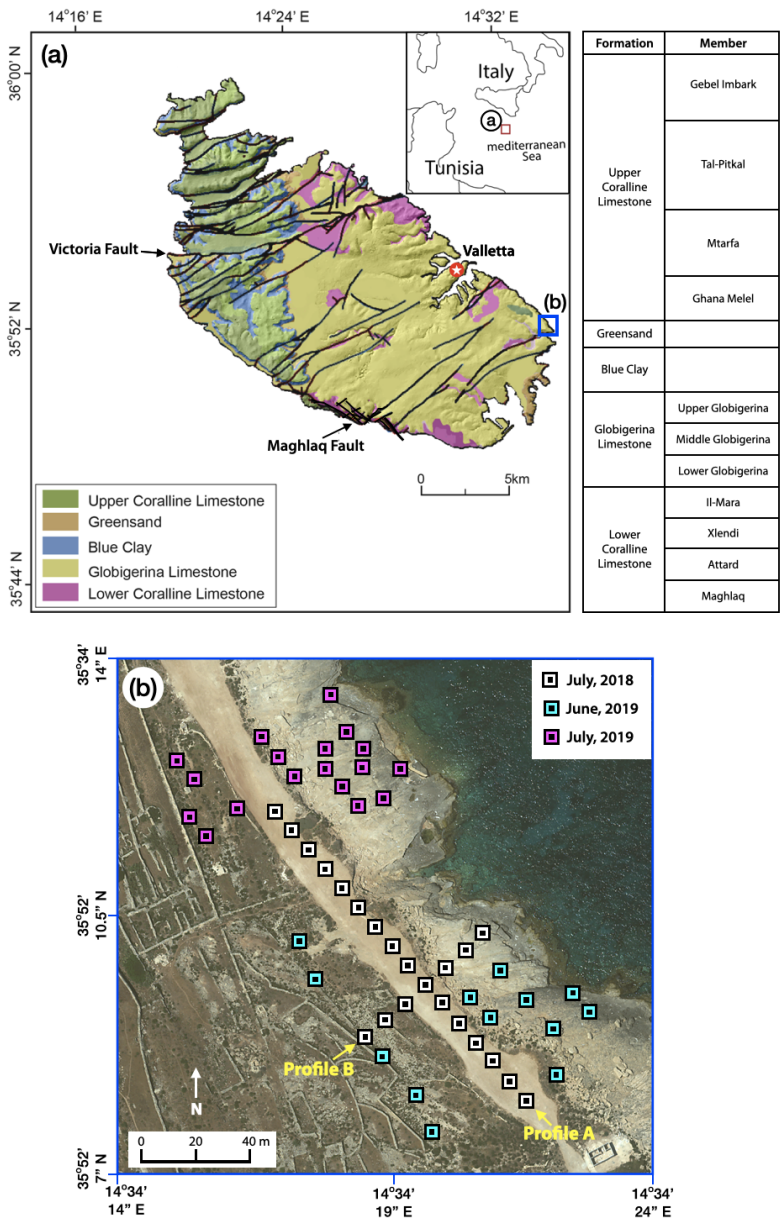

Figure 2.1: (a) Geological map of the island of Malta and an inset map shows location of Malta in the Mediterranean Sea as a red square. Modified from Geological Map of Maltese Islands [1993]. Black lines denote faults. The lithological profile is provided in the right panel. Study site is shown as blue square. (b) Detail of the study site in SE Malta; transect A is aligned NW–SE and B is aligned NE–SW. TDEM soundings are marked as squares with black squares inside; the difference in colors denotes different acquisition dates. White symbols show TDEM sounding locations from July 2018. Additional soundings investigated during June and July 2019 are indicated by cyan and purple symbols, respectively. Reprinted from Pondthai et al. [2020] with permission.

2.4 Methods

This study utilizes the near-surface TDEM geophysical method to determine the geometry and characteristics of the onshore MSLA along the coast at the survey site in SE Malta. The TDEM measurements were carried out using the Geonics (Canada) G-TEM system consisting of a portable battery-operated transmitter-receiver (TX-RX) console, a TX antenna deployed as 4 turns of a 10×10 m square loop of wire laid on the ground, a 0.6 m diameter RX rigid coil with pre-amplifier, and the supporting cables. In field operations, the equipment was deployed as shown in Figure 2.2. In this study, all soundings were acquired in the 20 time-gate mode, corresponding to investigation depths of 60–100 m. The 30-gate mode with longer acquisition time allowing for deeper exploration was not used. The depth of investigation also depends on the TX power, which is a product of the loop size, current, and its number of turns, in addition to the subsurface conductivity and the RX sensitivity [Spies, 1989].

The operating principle of TDEM is based on the EM induction process. An abrupt shut-off of a steady value of TX current in the wire loop, according to Faraday's law, generates an impulsive electromotive force (emf) that drives eddy current flow in the conductive earth. After the shut-off, the emf vanishes and the eddy currents start to decay. A weak secondary magnetic field is produced in proportion to the deceasing amplitude of the eddy currents. The multi-turn receiver coil located at the ground surface measures the time rate of change of the decaying secondary vertical magnetic field, the decay rate being diagnostic of the subsurface electrical resistivity.

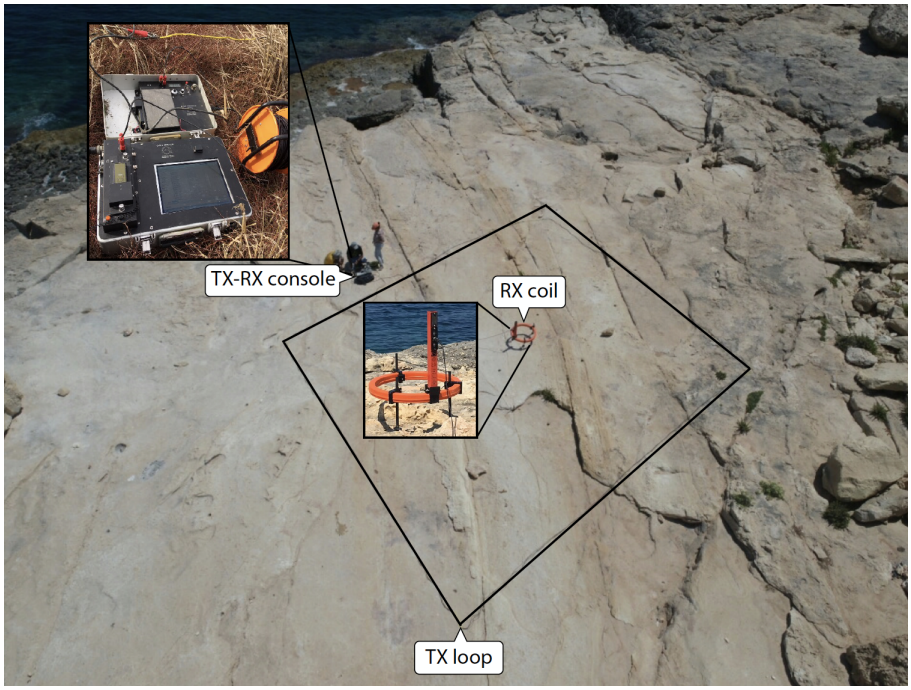

Figure 2.2: Field deployment of Geonics G-TEM geophysical equipment in SE Malta. Reprinted from Pondthai et al. [2020] with permission.

2.4.1 Data Acquisition

The geophysical survey procedure was as follows. At each sounding location, the wire loop was laid out on the ground. Then the RX coil with its pre-amplifier was set up in the center of the wire loop, to achieve a central-loop sounding. The portable TX-RX console was set up immediately outside the TX loop for convenience. A ramp-off current was passed through the wire loop using the signal generator in the TX console. The resultant signal received by the RX coil was recorded by the RX console, averaged over several thousand repetitions to improve signal-to-noise ratio. The overall time to acquire each sounding response was $\sim$5 min. Then the TX loop and RX coil were picked up, along with the TX-RX console, and moved forward to the next sounding location. The center of the RX coil represents the location of each sounding, that latter was recorded by handheld GPS. The operating frequency, i.e., the repetition rate of the TX on/off cycle, is in the kHz range (i.e., well outside the main power supply at 50 Hz and cell phones at $\sim$1 GHz.) The TDEM method is non-invasive, and no significant environmental disturbance is made to natural

flora, wildlife, or agriculture.

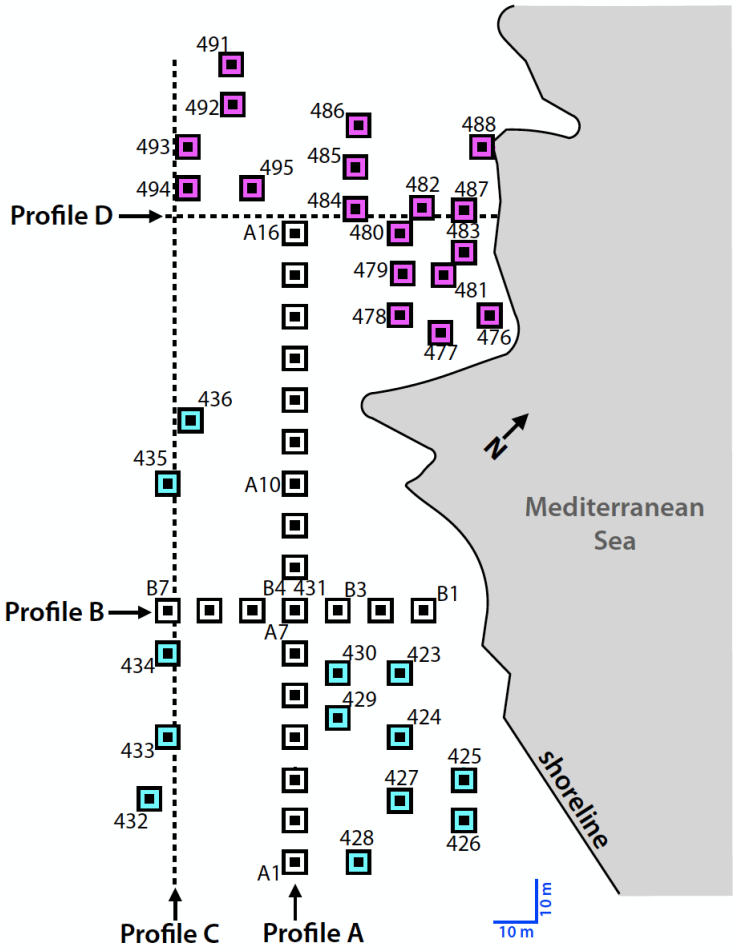

Figure 2.3: C are shown. A symbol denotes position of each sounding and differences in colors refer to different measurement dates. TDEM soundings deployed during July 2018, June 2019, and July 2019 are indicated by black-and-white, black-and-cyan and black-and-purple symbols, respectively. Reprinted from Pondthai et al. [2020] with permission.

The two orthogonal transects acquired in SE Malta comprising a total of 23 TDEM central-loop soundings in July 2018 are marked as black-and-white symbols in Figure 2.1b. Profile A is oriented from SE to NW along the shoreline with a total length of 150 m, while profile B is aligned from NE to SW with a length of 60 m (Figure 2.3). The two profiles cross each other at stations A7 and B4, respectively. An additional dataset of 31 soundings (cyan and purple symbols in Figure

2.1b; see also Figure 2.3) was added to this area from a second field survey conducted during June and July 2019. One of the 2019 soundings (station 431) was performed at the crossing point of the two previous transects (A, B) to check signal repeatability. The 2019 survey was performed in order to expand the coverage of the survey from the previous year. The rationale for adding more soundings is that the denser spatial distribution of data enables us to better construct a fully 3D geoelectrical model.

2.4.2 Data Analysis

2.4.2.1 1D Inversion

The 1D inversion of G-TEM transient EM sounding curves is performed using the IXG-TEM software from Interpex Ltd. After importing a data file containing a measured sounding curve, the software generates a consistent 1D smooth model of electrical resistivity vs. depth based on the iterative Occam regularization method [Constable et al., 1987]. The user is required to define the minimum, maximum depths and also the starting resistivity for initiating the model iterates. We seek the 1D inverted model that gives a satisfactory fit to the TDEM data with minimal variation in electrical resistivity between adjacent layers. Such a "smooth" model generally provides a preferable representation of subsurface geoelectrical structures compared to a "rough" model that may fit the data better but contains unrealistically large variations in resistivity between adjacent layers. An example of an inversion to 100 m depth of G-TEM sounding from station A7 is shown in Figure 2.4. The data points on the left indicate the Earth-response signal recorded by the RX coil as a function of time (in ms) after current is shut off in the TX loop. The red line on the right indicates an initial guess of Earth resistivity, which in this case is a uniform 10 half-space. The dark green line on the right indicates the calculated smooth depth profile of Earth resistivity, the predicted response of which (continuous dark green curve passing through the data points on the left) best fits the observed response, subject to the smoothness constraint. At this location, a high-resistivity zone of $\sim$80–100 Ωm appears at $\sim$4–22 m depth, underlain by a uniform low-resistivity zone of $\sim$2–3 Ωm.

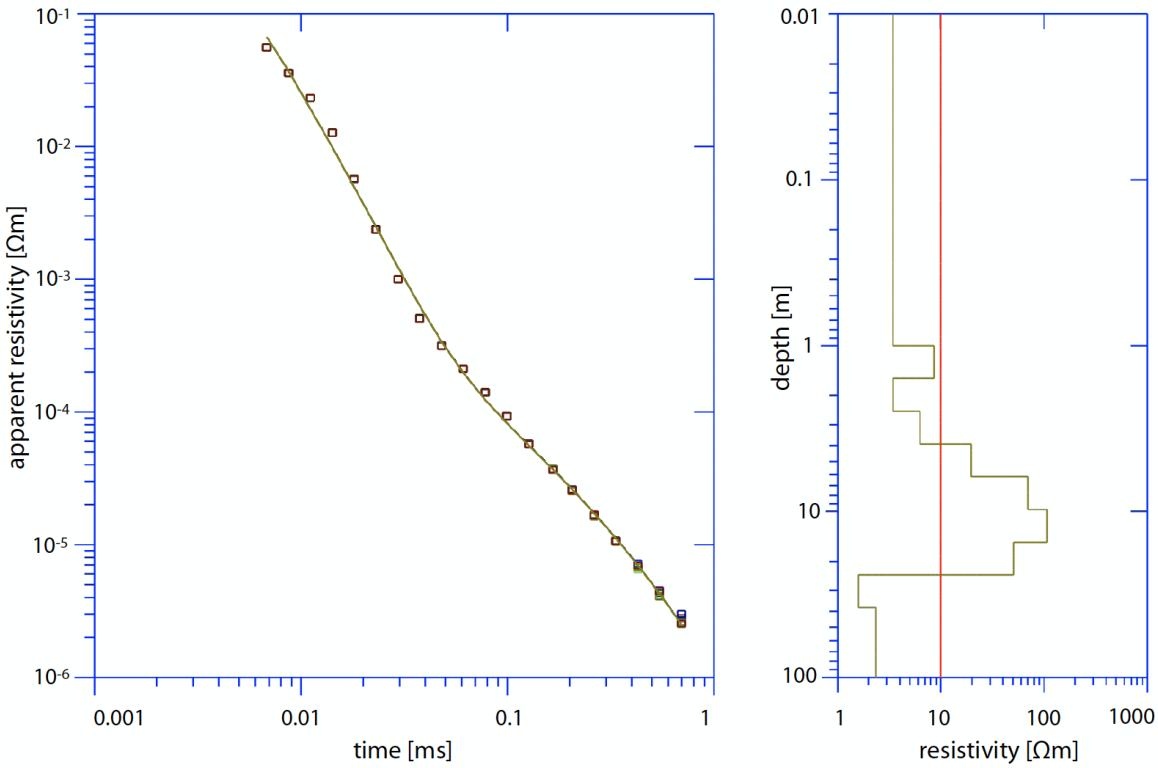

Figure 2.4: Example of G-TEM data shown as square symbols and the computed resistivity depth profile displayed as a curve passing through all data points with root mean square (RMS) misfit 6.8% (left); the fitted model is marked as the dark green line while the red line is the starting model (right). Reprinted from Pondthai et al. [2020] with permission.

2.4.2.2 1D Forward model context

In this study, we used a well-tested, in-house FORTRAN program to compute 1D transient responses based on a finite-radius, inductively-coupled loop source deployed over a layered earth. For such a 1D model, the resistivity changes only in a vertical direction. A series of 1D responses at different frequencies is computed using the well-known frequency-domain analytic solution [Ward and Hohmann, 1988, Everett, 2013]. The transient response is then obtained by taking an inverse Fourier transform of the frequency-domain responses using a Padé summation method [Chave, 1983].

2.4.2.3 2D and 3D Forward model context

This study also utilizes 2D and 3D forward modeling of transient EM responses to further constrain the geometry of the onshore geoelectrical structure of the SE Malta aquifer system. The computation of time-harmonic EM responses of aquifer geoelectrical models is performed using a finite-element (FE) analysis of the governing Maxwell equations in the magnetoquasistatic regime. The FE algorithm [Badea et al., 2001, Stalnaker et al., 2006] generates a rectangular mesh that is used to discretize buried 1D, 2D and 3D structures by defining rectangular prisms, or slabs, and assigning them certain dimensions, locations, and electrical conductivities (the inverse of resistivity).

In our simulations, the G-TEM transmitter (TX) in 'vertical dipole' mode is approximated by 4 turns of a circular current loop with 5.64 m effective radius (equivalent to the in-field-survey of a 10×10 m square loop) lying on the air-earth interface at the origin of the computational grid. A single receiver position is assigned to the center of the TX loop to simulate the central-loop configuration. The resistivity model is discretized using 100×100×100 nodes of a uniform rectilinear mesh with cell-size 0.8×0.8×0.8 m^3. The modeling-domain limits are –40 m, 40 m, –40 m, 40 m and –20 m, 60 m in the x, y and z directions, respectively. A typical mesh contributes roughly 4 million degrees of freedom to the finite-element system of equations since there are four complex degrees of freedom associated with each interior mesh node in the formulation, described below. The CPU time required to compute a single CSEM response for a model of this size at one frequency on the Aspen Systems Texas A&M cluster is ∼20 min.

The FE formulation is cast in terms of two Coulomb-gauged electromagnetic potentials, namely a magnetic vector potential $\mathbf{A}$ and a scalar electric potential Ψ. The Coulomb gauge condition is applied, $\nabla \cdot \mathbf{A} = \mathbf{0}$. A set of known primary potentials $(\mathbf{A}_p\ , \Psi_p)$ is specified, which consists of the analytic expression for electromagnetic induction in a homogeneous formation with σ_p constant (see [Badea et al., 2001, Stalnaker et al., 2006]). Secondary potentials $\mathbf{A}_s$ and Ψ_s are then defined according to $\mathbf{A} = \mathbf{A}_p + \mathbf{A}_s$ and $\Psi = \Psi_p + \Psi_s$, in which case the governing equations

become

$$\nabla^2 \mathbf{A}_s - i\omega\mu_0\sigma(\mathbf{A}_s + \nabla\Psi_s) = i\omega\mu_0\sigma_s(\mathbf{A}_p + \nabla\Psi_p) \tag{2.1}$$

$$\nabla \cdot [-i\omega\mu_0\sigma(\mathbf{A}_s + \nabla\Psi_s)] = \nabla \cdot [i\omega\mu_0\sigma_s(\mathbf{A}_p + \nabla\Psi_p)], \tag{2.2}$$

where $\sigma_s = \sigma - \sigma_p$ is the difference between the conductivity distribution whose response is required and the background value whose response is known. The value of electric field E and the induction field B are derived, after calculation of the Coulomb-gauged electromagnetic potentials, according to

$$\mathbf{E} = -i\omega(\mathbf{A} + \nabla\Psi), \tag{2.3}$$

$$\mathbf{B} = \nabla \times \mathbf{A}. \tag{2.4}$$

The spatial derivatives in the above equations are performed numerically in the post-processing stage of the algorithm.

To summarize, Maxwell's equations are formulated in terms of frequency-domain magnetic vector and electric scalar secondary potentials. The primary potentials are set by the aforementioned analytic solution and added to the calculated secondary potentials in order to obtain the total response at the prescribed frequency. At a given receiver location, such as the center of the TX loop, the total vertical magnetic field component is computed by numerical differentiation of the computed potentials. This procedure is repeated for a number of frequencies spanning several decades, building up the frequency-domain response. For this study, responses are evaluated at 43 logarithmically-spaced frequencies, at 6 frequencies per decade over the range 10^1–10^8 Hz. After its inverse Fourier transform into the time-domain, the resulting computed transient responses may be directly compared to the G-TEM sounding curves measured in the field.

2.5 Results

2.5.1 1D Scenario

First we analyze the transient EM soundings from the two orthogonal G-TEM transects of July 2018 comprising 23 locations along and across-shore SE Malta. The field dataset is divided into

two transects, labeled A and B. All soundings are plotted in terms of Earth-response voltage as a function of time on a single log-log display for each transect (Figures 2.5a, 2.5b). This format illustrates the variability, or scatter, in the temporal decay of the signals following shut-off in the TX current. A definition of time gate is provided in Appendix 2A. At station A3, a distinctive and unusual decay curve is observed, which is thought to be caused by effects of localized 3D subsurface structures of unknown origin. This curve, plotted as blue dots in Figure 2.5a, is clearly distinguished from the other curves and it cannot be fit by the response of a 1-D model. At A3, the unusual response - perhaps from inductive or IP coupling to steel infrastructure - exhibits a sign reversal (from solid to open circles) after gate 13 of the transient and it is not considered for further analysis. The central-loop response of a 1-D layered model cannot generate such a sign change.

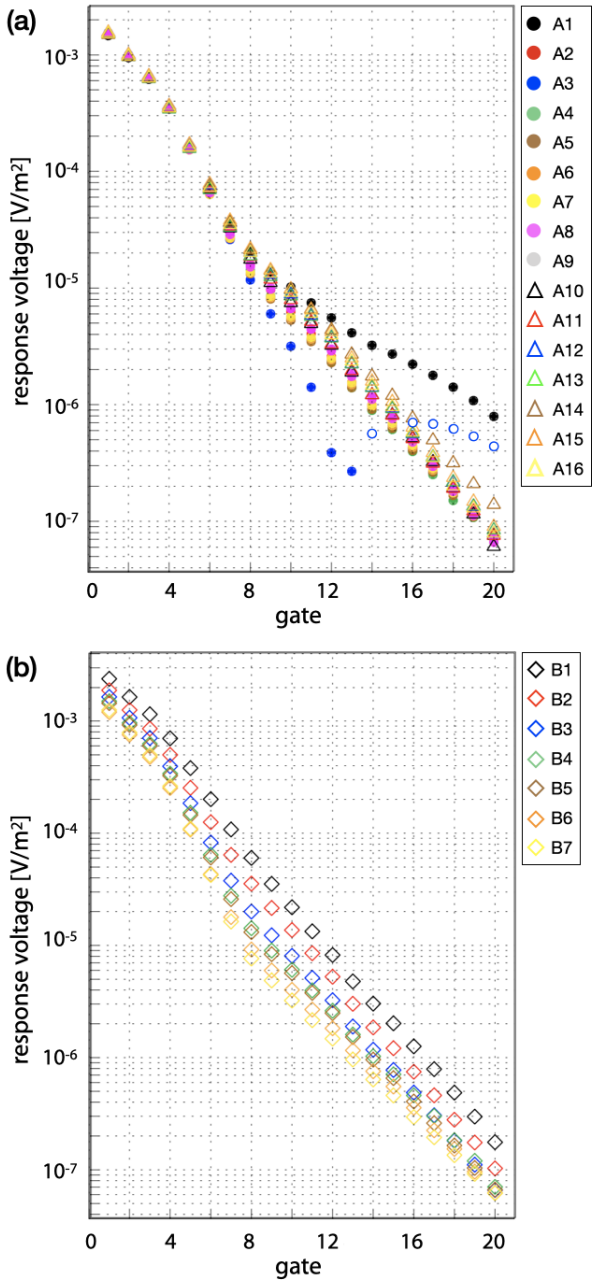

Figure 2.5: G-TEM data from 23 soundings in SE Malta. (a) All 16 soundings in profile A; (b) soundings from the 7 stations belonging to Profile B. Reprinted from Pondthai et al. [2020] with permission.

After examining the remaining 21 sounding curves comprising the alongshore profile, the responses from the southernmost stations A2, and A4–A9 may be classified as one group since they

exhibit very similar decay patterns. A separate 1D inversion was performed for each of these soundings. The resulting 1D resistivity models from each station were used as initial resistivity distributions in an attempt to find a single 1D model that could fit these southernmost soundings. After many iterations of computation and model adjustment using the 1-D analytic forward code, a simple 3-layer 1D model was found to be the most consistent with the field responses (Figure 2.6, right). This resistivity model for the southern section of profile A consists of a three layered-earth of 5.5 Ωm and 25 Ωm resistivity with 4 and 15 m thicknesses, respectively, and including a basal resistivity of 1.8 Ωm. The fit of this model to the sounding curves A2, A4–A9 is shown in Figure 2.6, left.

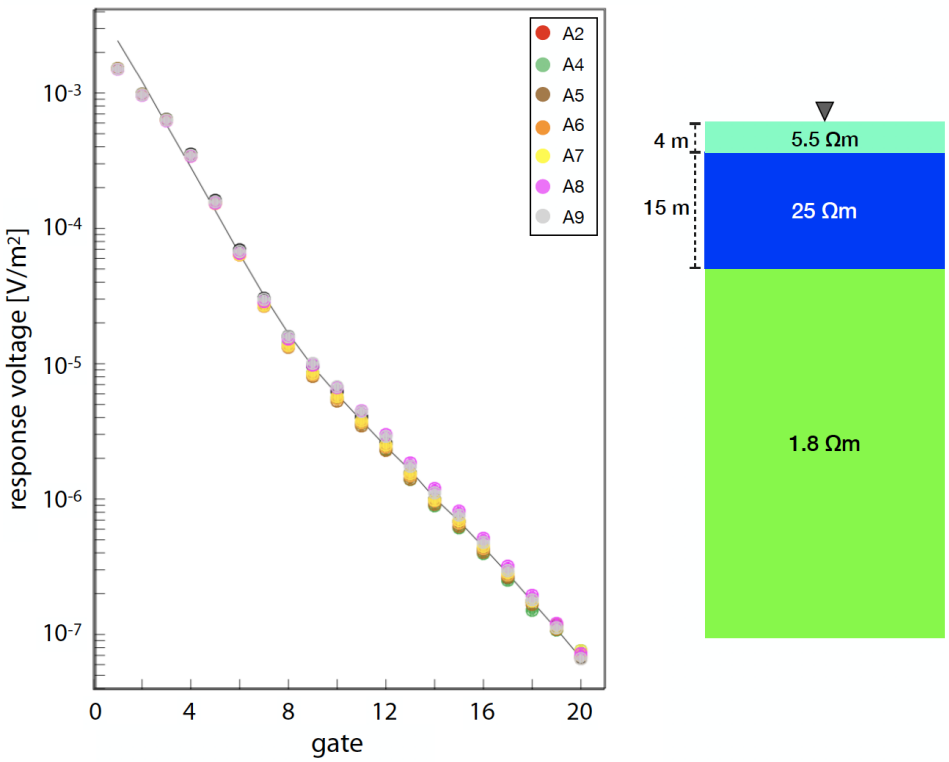

Figure 2.6: (left) 1D analytic forward result for station A2, A4 to A9 shown as the black solid line; (right) The resistivity model corresponds to the response (sold line) displayed in the left panel. Reprinted from Pondthai et al. [2020] with permission.

We used the same procedure to analyze the sounding curves from all 21 stations comprising the

reduced SE Malta 2018 dataset and the additional 31 soundings from the field survey conducted during June and July 2019. Another unusual decay curve is found at station 432 (black squares, Figure 2.7). At the late-time of this sounding, the observed signal decays significantly slower compared to neighboring stations, i.e., station 433, which is located only 15 m to the north. The anomalous response may be due to the effects of a localized highly-conductive body; this will be discussed later.

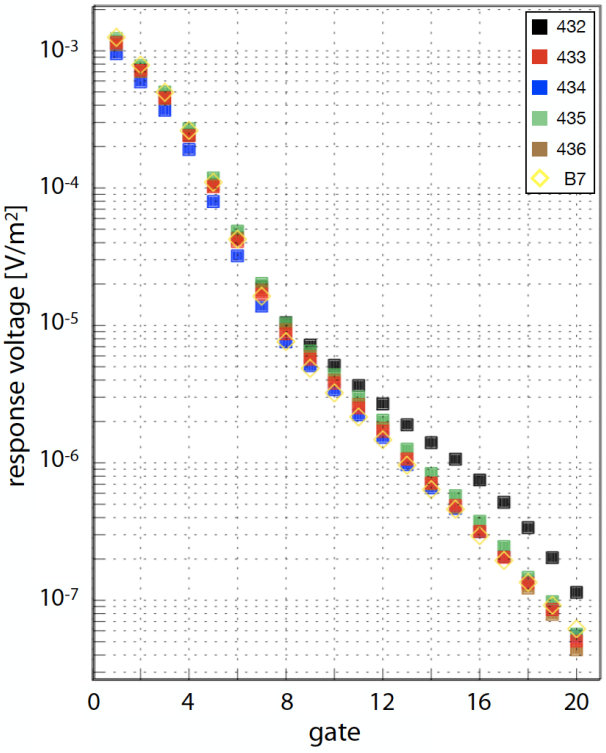

Figure 2.7: Decay curves of some measured G-TEM soundings at the western section of study area. An unusual decay at station 432 denoted as black squares may be due to a localized highly-conductive body. Reprinted from Pondthai et al. [2020] with permission.

After investigating all of the decay curves, we observe certain systematics in the spatial variability in the measured responses. Over distances of a few tens of meters, for example, it is shown below that the lateral changes in subsurface resistivities in the across-shore direction are much stronger than those in the alongshore direction. As regards the locations of soundings and simi-

larity of decay patterns, many of the more-recently acquired soundings are similar to those of the earlier-acquired transects A and B. For example, consider soundings 430 and 429, which are situated 15 and 25 m south of station B3, respectively (see Figure 2.3). The responses from these three stations, along with that of station 428, can be sorted as one group due to their similar decay pattern. The best-fitting 1D model of these 4 stations, whose response is illustrated as the thin black line in Figure 2.8, consists of a three layered-earth of 5.5 Ωm and 18.2 Ωm resistivity with 4 and 12 m thicknesses, respectively; with the basal resistivity of 1.8 Ωm. This model is displayed as the column beneath station B3 in Figure 2.9b.

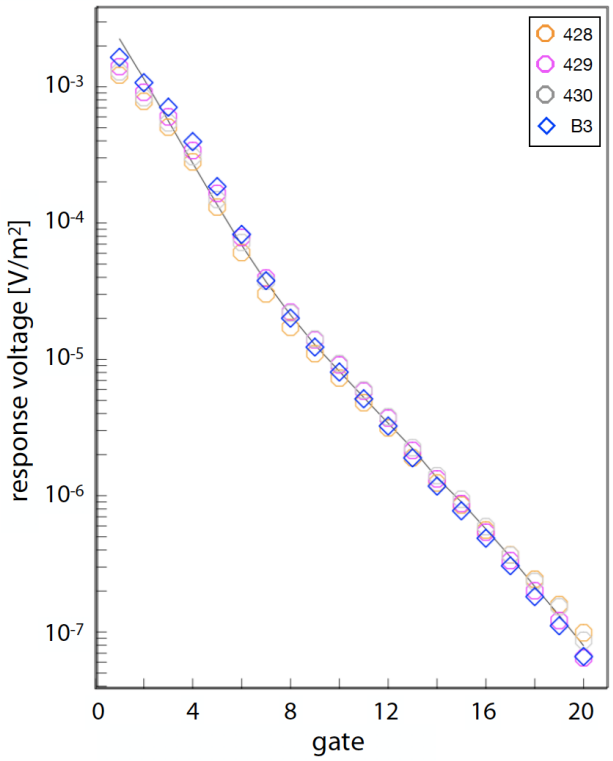

Figure 2.8: 1D forward modeling result for station 428, 429, 430 and B3 shown as a black line (see column beneath B3 in Figure 9b for the model). Reprinted from Pondthai et al. [2020] with permission.

From the 1-D forward modeling results, two pseudo-2D resistivity models have been constructed and they are depicted in Figure 2.9. These models are obtained by merging, or "stitching",

the 1D forward model results from groups of adjacent stations. With regards to the alongshore profile shown at the top, the upper-layer resistivity value is constant and it exhibits no variation in thickness observed along the 150 m transect. In the very near surface, from the surface to 3–4 m depth, the uppermost layer represents a spatial average over a heterogeneous region and we do not attempt to interpret this layer. The second layer spans the depth range 4–19 m in the SE part of the profile, but the layer becomes thinner and slightly more conductive in the NW part. A huge contrast in vertical resistivity variations of maximum 0.1 m beneath the sounding A1 compared with a neighboring sounding A2 is suggestive of structure with very low resistivity at depth, such as steel infrastructure. The lateral variations in resistivity of geological origin are much stronger in the across-shore transect, shown at the bottom. The top layer of this profile becomes slightly less resistive and thicker towards the coast. In contrast, the underlying resistive zone becomes thinner as the sounding location is located closer to the sea.

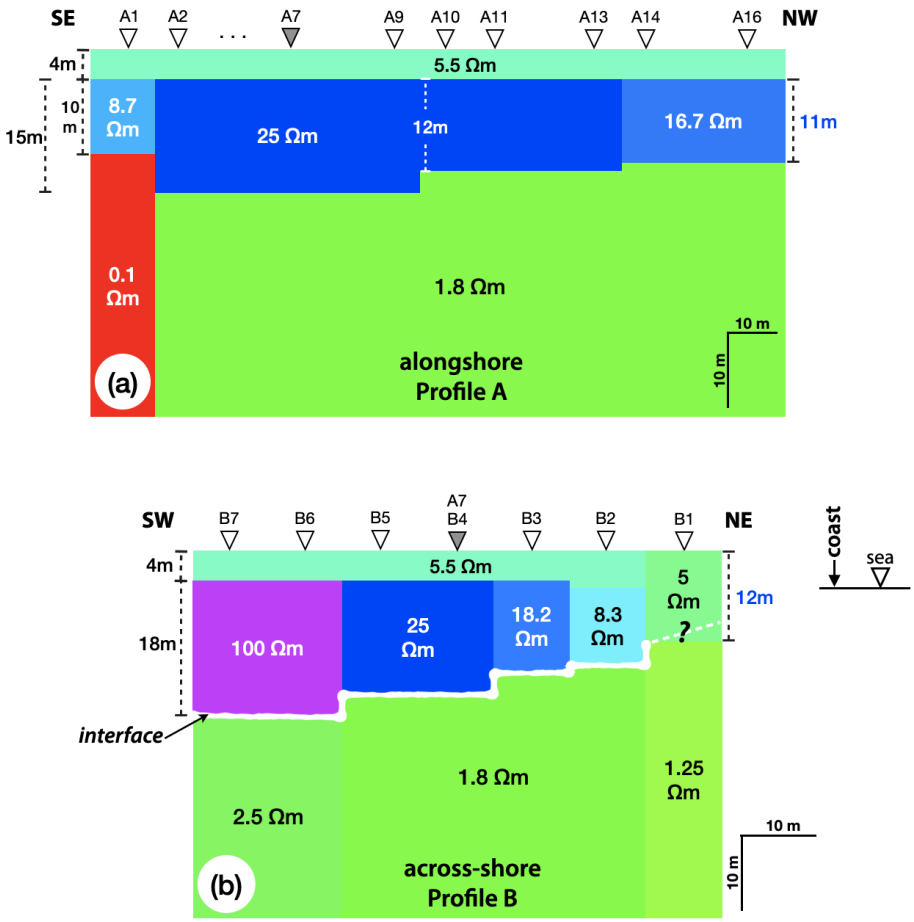

Figure 2.9: Stitched version of resistivity profiles obtained from 1D forward modeling results of the 2018 (a) alongshore Profile A and (b) across-shore Profile B surveys. The white line provides a rough guide to the geometry of the thinning of the freshwater lens towards the coast, where it becomes brackish to mildly saltwater. Reprinted from Pondthai et al. [2020] with permission.

In Figure 2.10, another set of pseudo-2D resistivity models, corresponding to TDEM profiles C and D (see Figure 2.3), are obtained by combining 1D forward model results from the 2018 and 2019 datasets. These models enable visualization of the resistivity structure in the western and northern parts of the study area. The model from profile C shown at the top (Figure 2.10a) is located ∼30 m west of Profile A. Profile C runs NW–SE alongshore and intersects profile B at station B7 (Figure 2.3). The resistivity model of this transect appears to be similar to that of Profile A. However, the resistivity values of the second and basal layers are higher in Profile C due to its

greater distance inland, i.e., away from the seawater. The second layer of Profile C is also thicker compared to that of Profile A. Lateral heterogeneity of resistivity at depth of ∼17.5 m to 60 m can be observed in the SE part of this transect similar to that of Profile A beneath soundings 432 and 433. The across-shore resistivity distribution in the northern part of the study area, labeled Profile D, is shown in Figure 2.10b. Profile D is located 90 m northward from the intersection of transects A and B. There is no significant change in either the thickness or resistivity of the uppermost structure of this profile as compared to Profile B. With respect to the middle, resistive layer along Profile D, the shape is comparable to the resistive zones found in Profile B, except they are less resistive and somewhat thinner.

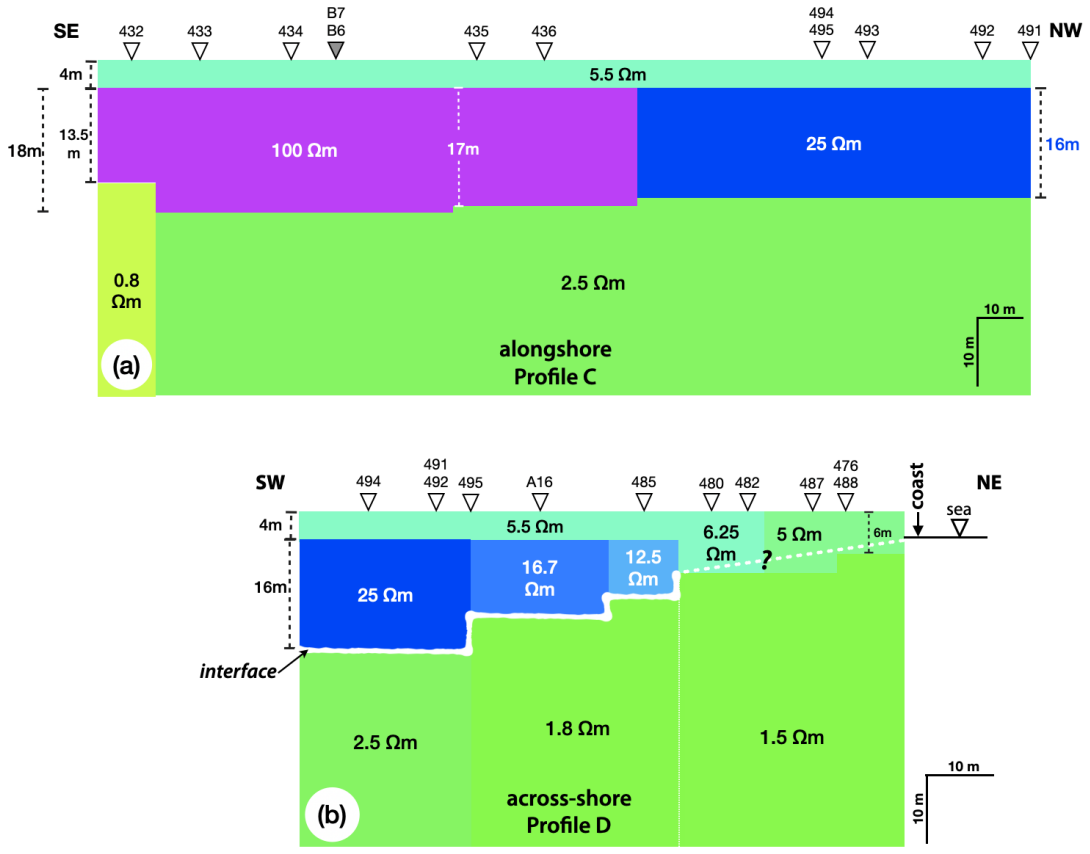

Figure 2.10: Stitched version of resistivity models from (a) Profile C along the western boundary and (b) Profile D in the northern part of the study site. The white line provides a rough guide to the geometry of the thinning of the freshwater lens towards the coast, where it becomes brackish to mildly saltwater. Reprinted from Pondthai et al. [2020] with permission.

2.5.2 2D and 3D Scenarios

In the previous section, we used the analytic solution of the TDEM forward problem to determine stitched 1D resistivity depth-profiles across the SE Malta study area. In this section, we use the FE analysis to compute frequency-domain responses of 2D and 3D models. The time-domain response is obtained by splining the frequency-domain response evaluated at each of the designated discrete frequencies. Subsequently, the set of time-domain responses are used as the input from which we develop a series of 2D and 3D forward model iterative adjustments. The best 2D and 3D models that result from this analysis are then further evaluated and interpreted. The adjustments are made by trial and error since insufficient computational resources are available to achieve an automated inversion process. Since a single forward run takes $\sim$14 hr of CPU time on our computational platform, and an automated inversion would require many thousands of forward runs, even with a highly efficient algorithm, it is envisioned that both coarse-grained and fine-grained massive parallelization are a prerequisite for a fully 3D inversion. Such algorithmic development is beyond the scope of this study, but is definitely recommended for future work.

Figure 2.11 shows FE-calculated responses at two stations based on the fully 2-D model constructed from the stitched 1-D resistivity models shown in Figure 2.9. The calculated response at station A7 obtains from the alongshore 2D resistivity model in Figure 2.9a. This model allows spatial variations in resistivity only in the SE-NW direction. That criterion is kept for all soundings along Profile A. Similarly, the 2D lateral resistivity distribution used to compare with the observed soundings at each station along Profile B is based on the across-shore transect shown in Figure 2.9b. The yellow dots in Figure 2.11, left, represent the field response actually measured at station A7. The modeling result of the alongshore 2D structure, computed using the 3D FE code, is marked as the solid line. Another sounding at the intersection of the two transects, namely station B4, is displayed in green diamonds in Figure 2.11, right, with the corresponding across-shore 2-D model response shown by the solid line.

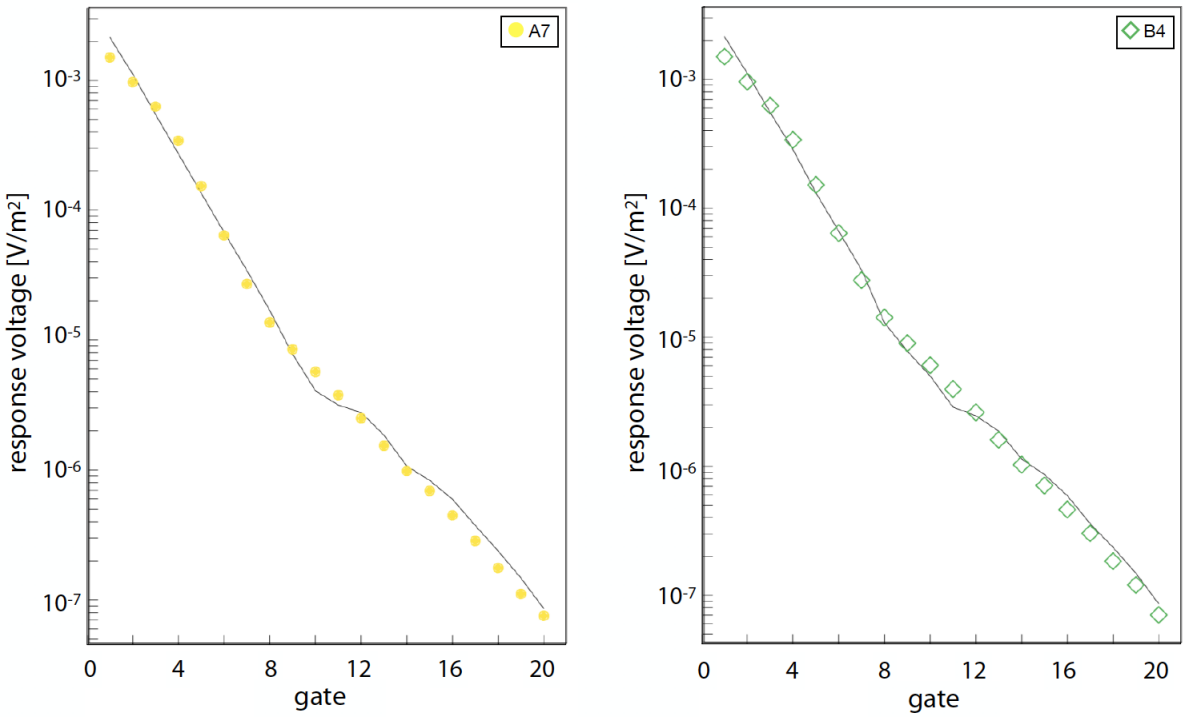

Figure 2.11: 2D modeling results of station A7 and B4 from left to right. A computed step-off voltage from 3D forward modeling code at cross-section point of two transects is shown as a black line. Reprinted from Pondthai et al. [2020] with permission.

At the bottom of Figure 2.12, the step-off voltage response as a result of 3D forward modeling was computed at station locations A7 and B4. The 3D model shown at the top of Figure 2.12 is constructed by combining the 2D models from the three transects, namely Profiles A, B (in Figure 2.9) and C (Figure 2.10a). For the sake of better visualization, only a local portion of the complete 3D model that is indicative of the structure beneath station A7 is illustrated within the modeling-domain limits of –40 m, 40 m, –40 m, 40 m and 0 m, 60 m in the x, y and z directions, respectively. Some part of the model that is above ground surface up to 20 m high is also excluded for better visualization; the size of 10×10 m square TX loop is shown for scaling. The complete 3D model representing the subsurface structure beneath SE Malta, covering a surface area of 16,500 m^2, is depicted in Figure 2.13. Some of the sounding points are included to better indicate the location and orientation of the 3D model with respect to the G-TEM survey layout. A brief sensitivity

analysis is provided in Appendix 2B.

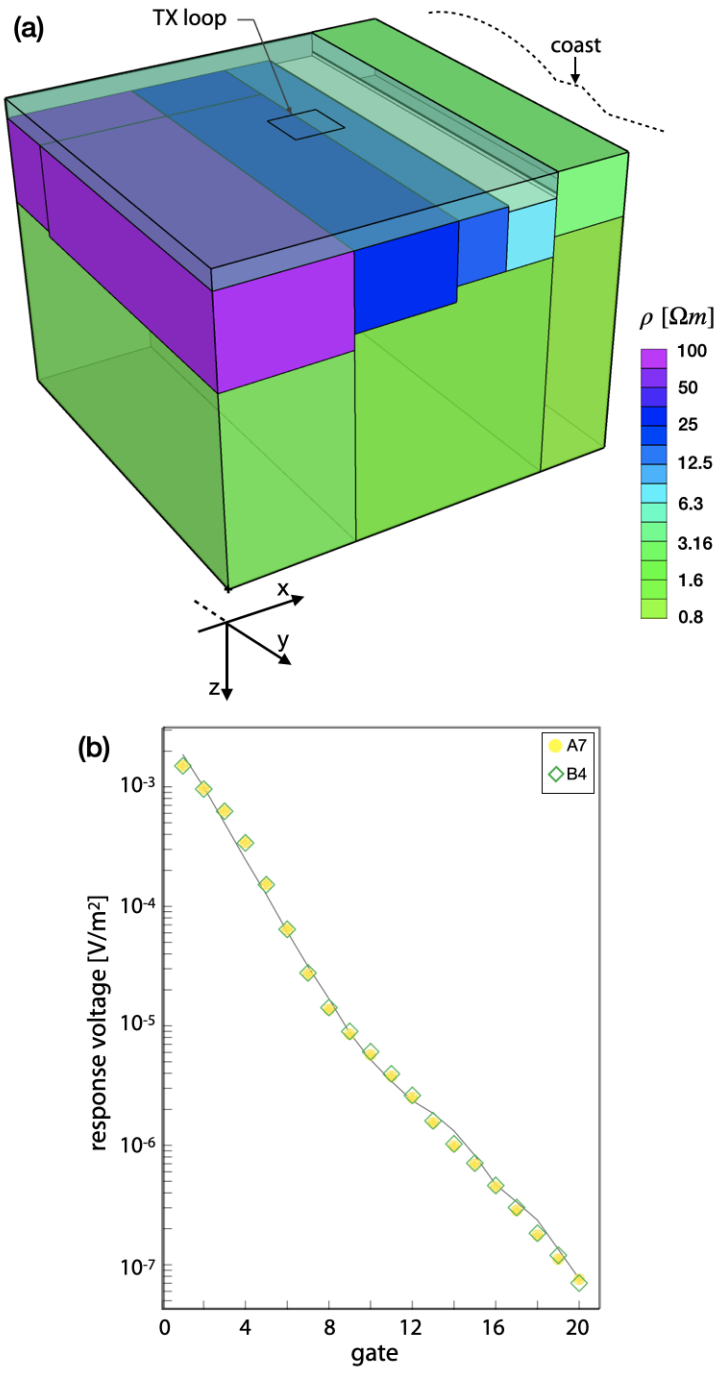

Figure 2.12: (a) 3D resistivity model showing the subsurface geoelectrical distribution beneath A7 and B4; (b) The computed step-off voltage according to the resistivity model in (a) is displayed as a black line. Reprinted from Pondthai et al. [2020] with permission.

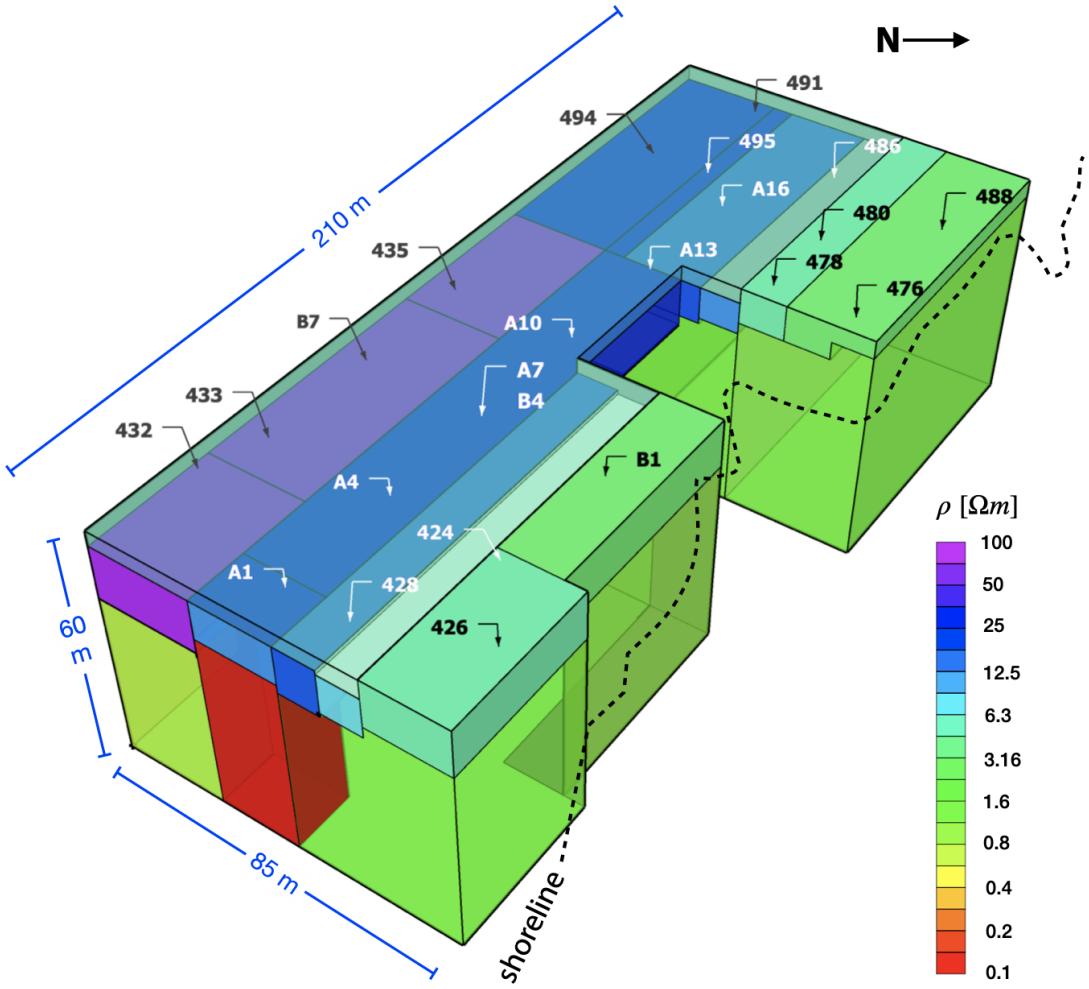

Figure 2.13: The preferred 3D model representing the subsurface geoelectrical structure beneath study site in SE Malta. Reprinted from Pondthai et al. [2020] with permission.

The computed misfit at each sounding location is plotted in terms of relative error, visualized using various circle sizes, for the 1D, 2D and 3D models. These misfit circles are shown in black, blue, and red, respectively (Figure 2.14). The misfits of the responses at gate 1 and 2 for all soundings are excluded from the display since the amplitude of the early-time responses is very large. The relative errors of the 2D model are shown only at the 21 stations of the reduced SE Malta 2018 dataset located along transects A and B. The reader should note that the misfit of the preferred 3D model at a given station may exceed the misfit of the 1D model at that station. The

important point is that a single 3D model has been found that fits all the observations reasonably well, sometimes at the cost of locally increasing the misfit compared to a 1D model that strictly applies only to an individual station. The actual geoelectrical structure of the Earth is 3D rather than locally 1D beneath the G-TEM measurement stations.

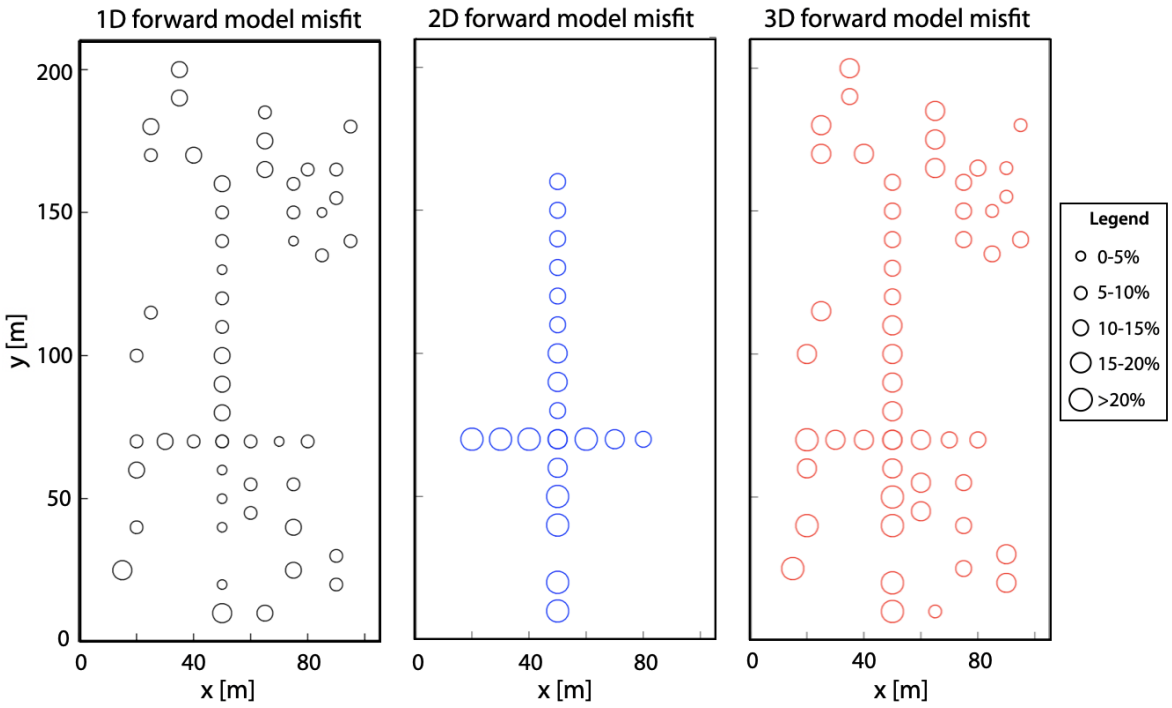

Figure 2.14: Misfit of 1D, 2D and 3D models, from left to right. Size of circle represents a relative error for each sounding. Only 21 points of misfits are shown for 2D model along 2018 dataset. Reprinted from Pondthai et al. [2020] with permission.

2.6 Discussion

The results presented in this study suggest that the structure of the mean sea-level groundwater aquifer near the shore in SE Malta exhibits a lenticular shape, with decreasing thickness towards the coast. The combination of TDEM models derived from the summer 2018 and 2019 datasets shows distinct high-resistivity zones. These are interpreted as the signature of a brackish water-saturated geological medium, in this case corresponding to the LCL formation hosting the mean

sea-level groundwater body.

Based on the preferred 3D TDEM model in Figure 2.13, the top layer up to 5 m deep is interpreted as the overlaying Globigerina Limestone and there is no geophysical indication of freshwater in this low-resistivity formation. We also find that the depth to the top of LCL and water table in the study area is 4–5 m. Our study is in good agreement with a regional groundwater modeling study of the South Malta region which points out that the elevation of the top of the formation holding fresh groundwater is in the range +20 to –20 m with reference to mean sea level [MARSOL, 2015]. The zones of high resistivity below the depth of 4–5 m in the 2D and 3D models are indicative of a (moderately brackish) freshwater-bearing formation with resistivity in the range ρ $\sim$10–100 Ωm (i.e., the purple-blue-cyan colors in Figure 2.13). The steeper base compared to the gentler top of the groundwater body is consistent with the geometry of a Ghyben-Herzberg-type lens. Below the freshwater region, from depths $\sim$13–22 m down to the TDEM depth of investigation at 60 m, the underlying rocks situated beneath sea level are much less resistive, attaining values ρ $\sim$1.25–2.5 Ωm (i.e., the green-yellowish green colors in Figure 2.13). These low resistivity (conductive) zones are indicative of a seawater-saturated formation. The shallow resistive freshwater lens sits on top of a more conductive formation, the latter being indicative of lateral landward movement of saltwater, i.e., intrusion. The boundary between the zones of high and low resistivity indicates the presence of the interface or transition zone along the two across-shore transects. Within the areas closest to the shoreline a mixing zone of freshwater and seawater appears to be present. Zones of moderate resistivity ρ $\sim$5 Ωm are observed along the northeastern parts of the across-shore transects by the coast and this could be indicative of brackish groundwater.

In order to assess the groundwater quality implications of our model, we calculate the bulk resistivity of the fluid-saturated rock using Archie's law for various porosities of limestone assuming that all pore spaces are filled with freshwater with resistivity of 2 Ωm. This latter value is equal to the water resistivity found in a well located 2.5 km inland. For porosities of 10% and 15% we find 126.2 and 60.8 m, respectively, as the formation bulk resistivity. These values of estimated

resistivity are slightly higher than the range of those in the 3-D TDEM model (ρ $\sim$10–100 Ωm). In addition, we have estimated bulk resistivity for saturated limestone filled with seawater of 0.2 m with 10$\%$, and 15$\%$ porosities. These are 12.6 and 6.1 Ωm, respectively, which is also slightly higher than our model's prediction of low resistivity seawater-saturated formations of 1.25–2.5 Ωm. As we move inland, our values are consistent with the borehole's fluid resistivity saturating a formation of 10 to 15$\%$ porosity. Closer to the shoreline, the TDEM bulk resistivity is lower, reflecting more brackish water. Thus, the groundwater freshens as we move inland. Of course, Archie's law is not a perfect petrophysical model for the fractured limestone lithology, since the law was founded on lab measurements made on clean sandstone cores, but an Archie-type calculation should be approximately correct.

To assess confidence in the spatial structure of our model, we also consider which of the model slabs indicative of the freshwater-bearing formation are best resolved based on the sensitivity analysis (see Appendix 2B for details). At the lower frequency of 100 Hz, the best-resolved slab is slab 3; whereas the responses from slabs 5, 6 and 7 are more sensitive to perturbations in their resistivity than the responses of slabs 1 and 2. At the high frequency 1 MHz, the misfit-change distribution indicates that changing a slab's resistivity affects only the sounding that is situated directly over that slab. Slab 6 seems to be the most well-resolved slab at the intermediate frequency 31.6 kHz. Slabs located further inland appear to be not as well resolved as those closer to the sea. The latter are thin and more conductive relative to the thicker, more resistive inland slabs and it is well known that terrestrial TDEM better resolves thin conductive layers. We do not have sufficient data coverage to infer a possible offshore extension of the freshwater aquifer at the SE Malta study site. The landward encroachment of seawater decreases the resistivities of the near-coastline region and possibly interacts with the fresh groundwater of the MSLA. There are unpublished ground-penetrating radar (GPR) data that appear to show infiltrated meteoric water trapped in fractures above water table in some areas of the study site [Rizzo, 2020]. More across-shore measurements throughout Malta are recommended in order to investigate the lateral subsurface geoelectrical variation in the direction perpendicular to the coast.

2.7 Conclusions

This study demonstrates the utility of the TDEM geophysical method along with 1D, 2D and 3D forward modeling as a means to study coastal freshwater aquifers in water-scarce regions. Here we image the geometry of the onshore aquifer within the permeable Lower Coralline Limestone formation along the SE Malta coast. Our results show 2D and 3D resistivity models found by iterative adjustments of FE forward modeling. The final preferred 3D model provides information to depth of 60 m, covering an area of $\sim$16,500 m^2 and shows diagnostic spatial variations in subsurface electrical resistivity. The geophysical modeling provides a basis for determining important characteristics of the MSLA that fit our observations, namely the decreasing thickness of fresh groundwater bodies towards the coastline. Zones of fresh groundwater have been identified, but these are located preferentially inland from the coast. Thus, there is no indication from the electromagnetic data of a robust offshore extension of the MSLA at this location. However, it is argued that method that we used can be applied across the entire Maltese archipelago to better constrain the geometry, dimensions and distribution of terrestrial and coastal aquifers providing valuable information for future water management of the stressed groundwater reserves of Malta.

2.8 Appendix 2A: Receiver Gates and Times

The G-TEM receiver records the characteristics of transient response by sampling it at 20 or 30 sequential time intervals or gates. The gates are logarithmically-spaced times that fill the measurement period and their widths (separation) exponentially increase with time [Geonics, 2016]. Table 2.1 lists the center time of each gate that occurs after TX shut-off for repetition rate of 237.5 Hz at 20-gates acquisition mode.

Gate	Time (μs)	Gate	Time (μs)
1	6.813	11	77.94
2	8.688	12	99.38.
3	11.13	13	126.7
4	14.19	14	166.4
5	18.07	15	206
6	23.06	16	262.8
7	29.44	17	355.2
8	37.56	18	427.7
9	47.94	19	545.6
10	61.13	20	695.9

Table 2.1: Gate center times. Reprinted from Pondthai et al. [2020] with permission.

2.9 Appendix 2B: Sensitivity Analysis

It is of interest to examine which of the slabs indicative of the freshwater-bearing formation responds most sensitively to the time-domain electromagnetic excitation. Conducting a sensitivity analysis provides information about how small perturbations to an independent variable, in this case a slab resistivity, affect the 3D model's overall misfit. Herein, the resistivity of each slab is subjected to a 5% decrease and the 3D response re-computed, with only one slab changed at a time. We compute the vertical magnetic fields at three different frequencies to determine the changes in subsequent responses after each slab's resistivity is changed compared with the responses of the unperturbed preferred model shown in Figure 2.13. The choices of 100 Hz, 31.6 kHz, and 10 MHz generate low, medium, and high frequency responses, respectively. Seven slabs with various resistivities ranging from 8.3 to 100 Ωm are chosen and the corresponding seven sounding locations on the surface nearest the center of each slab are selected for monitoring the change of computed responses (see Figure 2.15). For example, station B7 is underlain by slab 1, station B4 overlies

slab 2, station B3 is above slab 3, and so on. The computed misfit resulting from a model that includes a perturbation in a slab's resistivity is displayed in terms of relative change, illustrating using a color plot for the three different frequencies in Figure 2.16.

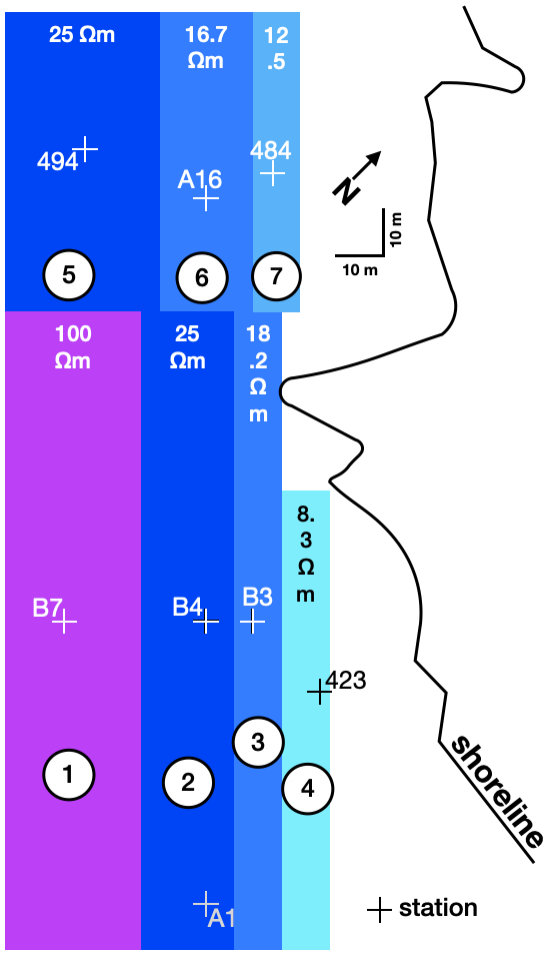

Figure 2.15: Illustration of the location of selected slabs (numbered 1–7) that are suggestive of a water-bearing formation, and the TDEM sounding locations where the sensitivity analysis is performed. Value of unperturbed resistivity is shown for each slab. Reprinted from Pondthai et al. [2020] with permission.

At low frequency (100 Hz), Figure 2.16 top left, the changes in frequency-domain responses at each station are mainly due to the directly underneath slab and to the neighboring slabs. This is indicated by the larger values of percentage misfit mainly along the diagonal of the plot. An

exception is the change caused by decreasing in resistivity of slab 1 that did not appreciably affect the misfit at any of the 7 stations. Surprisingly, the sounding 494, beneath slab 5, is most sensitive to the decrease of resistivity of slab 3 at frequency of 100 Hz. At moderate frequency (31.6 kHz), Figure 2.16 top right, slab 1 has a minor impact on the data if its resistivity decreases. The misfit plot shows how the change in one slab's resistivity affects almost all the surrounding stations by different amounts. Moreover, the change in resistivity of slab 6 has a large effect on observed responses at the soundings A16 and 484, located above slabs 6 and 7, respectively. At high frequency 10 MHz, bottom left of Figure 2.16, the misfit-change distribution indicates that decreasing a slab's resistivity is likely to affect only the sounding that situated over that slab. This result is not surprising since the footprint of a TDEM sounding is smallest at high frequencies.

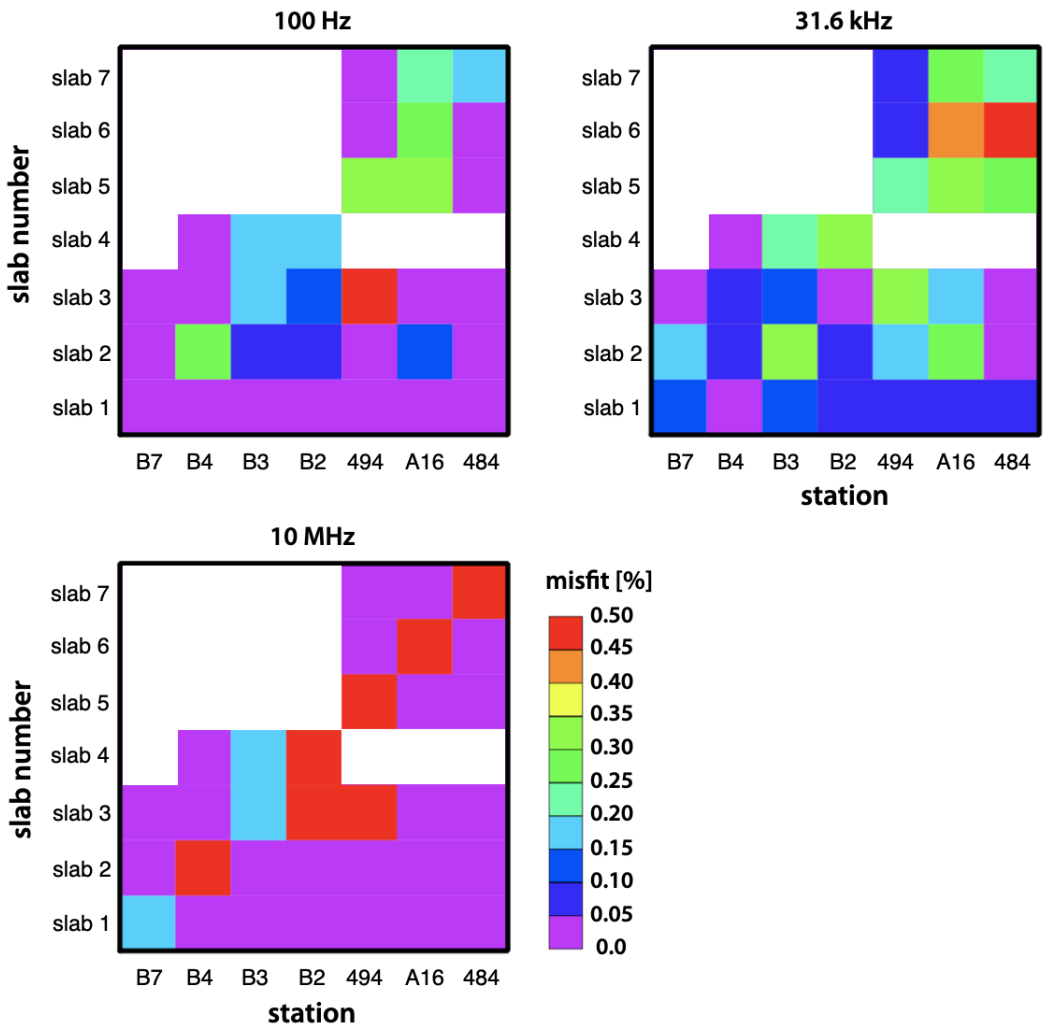

Figure 2.16: Response misfits for 100 Hz, 31.6 kHz and 10 MHz. Color plot denotes a relative change in percentage misfit for examples of seven soundings after each slab's resistivity decreases by 5%. The white region in each plot signifies that there is no effect from perturbation to a particular slab detected by that sounding location. The misfits over 0.25% at each frequency are considered significant by rough estimation, and this will affect the 1D, 2D and 3D modelling misfits of transient EM responses in Figure 2.14. Reprinted from Pondthai et al. [2020] with permission.

3. ELECTROMAGNETIC IMAGING OF DISCRETE GROUNDWATER DISCHARGE CONDUITS TO THE SEA ALONG THE CANTERBURY COAST (NEW ZEALAND)

This manuscript planned to submit to *Remote Sensing*: Special Issue "Recent Advances in Geophysical Exploration and Monitoring on Coastal Areas".

3.1 Abstract

This study utilizes 2D forward modeling based on 3D finite element (FE) analysis of time-domain electromagnetic (TDEM) responses acquired on the southeast New Zealand coast near Ashburton in order to: 1) constrain the 2D geometry of potential discharge conduits, beneath the braided outwash of the Canterbury plains, that focus groundwater flow into and beneath the beach; 2) investigate the spatial association of the groundwater discharge conduits with coastal gullies. To accomplish the objectives, terrestrial geophysical TDEM surveys were made using the G-TEM instrument (Geonics Ltd., Mississauga, ON, Canada). Four slingram transects were conducted on the plains inland across the heads of gullies along with across-shore central-loop survey between two coastal indentations. Possible scenarios for a groundwater discharge model including 2D geometry of potential conduits that matches the G-TEM measurements along May15-1 transect are explored. A spatial relationship between the locations of eroded coastal gullies and the G-TEM-inferred locations of groundwater discharge conduits beneath the braidplain alluvial sediments is also determined. The final preferred 2D model provides information to depth of 60 m, covering a length of $\sim$100 m and shows diagnostic spatial variations in subsurface electrical resistivity that could be characterized by distinct zones of elevated conductivity under the plains.

Keywords: coastal hydrogeophysics; groundwater discharge; coastal gullies; transient electromagnetics; finite-element

3.2 Introduction

The existence of continental groundwater discharge directly into the ocean from coastal areas has long been recognized by hydrologists; unlike surface water runoff, subsurface flows are

not directly visible or easily quantified [Burnett et al., 2001, Taniguchi et al., 2002]. Studies of interactions between groundwater and coastal seawater recently have gained attention from the hydrogeologic community. In coastal aquifers connected to the ocean, fresh groundwater flow may be driven offshore by a hydraulic gradient that is similar to the flow of rivers into the sea. Moreover, both shallow and deeper aquifers beneath the continental shelf can extend for considerable distances from the shoreline before discharging into the sea at outcrops and/or through fractures [Burnett et al., 2003]. Groundwater discharge from coastal aquifers is important because it contributes to the chemical mass input into the ocean [Jiao and Post, 2019]. Elements such as carbon, nitrogen and phosphorus in groundwater can have concentrations several orders of magnitude higher than in surface water, and the transport of these nutrients and anthropogenic contaminants influence the chemical and biological characteristics of shallow marine ecosystems [Johannes, 1980, Moore, 1996, Santos et al., 2008].

The time-domain electromagnetic (TDEM) method of geophysical exploration employing a controlled-loop source, long used to investigate onshore groundwater bodies, is also used in the study of terrestrial-marine groundwater interactions. The TDEM method is sensitive to electrical resistivity which, in turn, is diagnostic of important hydrological parameters such as porosity and water saturation [Archie, 1942]. The method responds to the electromotive force provided by the interaction of an applied time-varying magnetic flux with the geoelectrical structure beneath the transmitter loop. The key physical mechanism is the induction process governed by Faraday's law, which is equivalent to diffusion into a conducting medium of an image of the transmitter (TX) loop current. A fundamental overview of the physical principles underlying electromagnetic (EM) geophysical methods is given elsewhere [Nabighian and Macnae, 1991, Everett and Chave, 2019a, Everett and Chave, 2019b], and there are many reviews related to near-surface applications of EM techniques, (e.g. [Everett, 2012, Fitterman, 2015, Streich, 2016]).

Coastal gullies are specific geomorphic features associated with disturbed land that are often found adjacent to sea cliffs within the coastal zone. Outpacing of the ground resistance by the erosive force of surface runoff can incise a gully into a cliff or bluff. An important process that po-

tentially causes a retreat of a coastal cliff and incision of a gully is groundwater discharge through or under the cliff into the sea [Kline et al., 2014, Collins and Sitar, 2009, Collins and Sitar, 2011]. Where the sea cliff face is affronted by a beach, with no outward sign of overland flow and in the absence of basal wave quarrying, groundwater seepage could play an important role as a driving mechanism for coastal gully formation and evolution [Micallef et al., view]. However, there have been very few geophysical studies on the subsurface distribution of groundwater pathways in places where coastal gullies have formed.

Forward and inverse modeling of time-domain electromagnetic (TDEM) responses for 1D and 2D earth structures have been widely used for environmental, hydrological investigations [Fitterman and Stewart, 1986, Fitterman, 1987, Kafri et al., 1997, Meju et al., 2000, Auken et al., 2003, Danielsen et al., 2003, Porsani et al., 2012] including coastal and marine aquifer characterization [Nielsen et al., 2007, Costabel et al., 2017, Ezersky and Frumkin, 2017, Lippert and Tezkan, 2019]. Studies that have identified seawater intrusion in coastal aquifers using 1D or 2D TDEM methods can be found in [Goldman et al., 1991, Herckenrath et al., 2013, El-Kaliouby and Abdalla, 2015, Martínez-Moreno et al., 2017, Kalisperi et al., 2018, Torres-Martinez et al., 2019]. There have been several sedimentological studies focusing on mapping the subsurface architecture of fluvial and braided river deposits using related geophysical techniques, such as ground-penetrating radar (GPR) [Beres et al., 1995, Bridge and Lunt, 2006, Okazaki et al., 2013, Huber and Huggenberger, 2016] and a combination of GPR with electrical resistivity tomography (ERT) [Bowling et al., 2005, Rey et al., 2013]. There have been a few hydrological studies focusing on different aspects of subsurface fluid flow, such as flow in a heterogeneous fractured reservoir. These studies generally employ the frequency-domain EM method, e.g. [Sasaki and Meju, 2006, Ge et al., 2012, Ge et al., 2015]. The use of forward modeling for TDEM data, specifically with the loop-source configuration, has been applied to mineral exploration [Maher, 1992, Batayneh, 2008, Flores and Peralta-Ortega, 2009, Smith, 2014]. Examples include applying 3D TDEM forward codes to investigate the complex geometry of ore bodies and fault

systems. The 3D forward modeling in these studies is based on finite-element (FE) [Li et al., 2017] and finite-volume (FV) approaches [Lu, 2020]. A TDEM forward-modeling study based on a FE solution technique for a complex-shaped TX loop that also accounts for topography is provided in [Li et al., 2018].

The research described herein is part of the multi–disciplinary MARCAN project that aims to: define the characteristics and dynamics of topographically–driven meteoric groundwater systems in passive continental margins, and demonstrate that topographically-driven meteoric groundwater is an important geomorphic agent in passive continental margins [MARCAN, 2020]. An important aspect of the MARCAN project is to explore potential onshore-offshore groundwater aquifer connections based on terrestrial TDEM and marine controlled-source electromagnetic (mCSEM) geophysical data from the Canterbury Plains, New Zealand. In this paper we utilize 3D finite element analysis and carry out 2D forward modeling of TDEM responses acquired on the southeast New Zealand coast near Ashburton in order to: i) constrain the 2D geometry of potential discharge conduits, beneath the braided outwash plains, that focus groundwater flow into and beneath the beach; ii) investigate the spatial association of the groundwater discharge conduits with coastal gullies. To accomplish these objectives, TDEM responses were acquired with the Geonics G-TEM instrument (Geonics Ltd., Mississauga, ON, Canada) [Geonics, 2016]. The analysis of the TDEM data generates geoelectrical models that facilitate a better understanding of the development of coastal gullies associated with groundwater seepage through preferential hydraulic flow paths beneath the plains.

3.3 Regional Setting and Study Site

This study focuses on the eastern coast of the South Island of New Zealand adjacent to the Canterbury Plains $\sim$16 km SE from the town of Ashburton. The plains consist of broad fluvial megafan and glaciofluvial sheet deposits that formed as a result of braided-river drainage from the Southern Alps during the late Pleistocene (particularly since the Last Glacial Maximum) and Holocene Epochs. The plains are situated along the eastern margin of the South Island, covering an area of $\sim$7500 km^2 (Figure 3.1). The plains are transected by large, high-energy, gravel-bed rivers

that have mean annual discharges of 20–200 m^3/s [Browne and Naish, 2003]. Rangitata, Rakaia, Waimakariri and Ashburton are the major rivers that flow and incise the plains to the shoreline. The Quaternary sedimentary fluvial–deltaic sequence comprises ∼300–600 m thickness of gravel, sand and mud with associated aeolian deposits and palaeosols [Bal, 1996, Browne and Naish, 2003]. The gravels are comprised of greywacke and appear as a variety of channel-fill beds and bar forms, whereas the isolated bodies of sand appear as relict bars and abandoned channels. The interglacial deposits near the coast are better sorted and have higher porosity and permeability than the glacial outwash, resulting in a wide range of hydraulic conductivities [Scott, 1980]. The largest groundwater supply in New Zealand is contained in Quaternary gravels that are found to at least 150 m depths [Davey, 2006].

The sea cliffs along the Canterbury coast are comprised of Pleistocene sediments and their formation owes to coastal processes acting in response to the rise in sea level associated with the post-Pleistocene deglaciation (∼16 ka). The elevation to the top of the coastal cliffs in the study site is ∼20 m above present-day mean sea level. High-energy waves from heavy storms offshore and the movement of coastal sediment resulted in the landward retreat and erosion of the fans of the Canterbury Plains, producing the cliffs that are now observed along the mid Canterbury coast [Flatman, 1997]. The cliffs are retreating at ∼1 m/year [Schumm and Phillips, 1986]. The beach along the Ashburton coastline is classified as a mixed sand and gravel beach, composed of a relatively uniform sand-gravel mix throughout the entire cross-shore profile, with average grain size of ∼19 mm [Jennings and Shulmeister, 2002]. The beach morphology is reflective [Wright and Short, 1984] and the average beach width along the survey site is not more than ∼30 m.

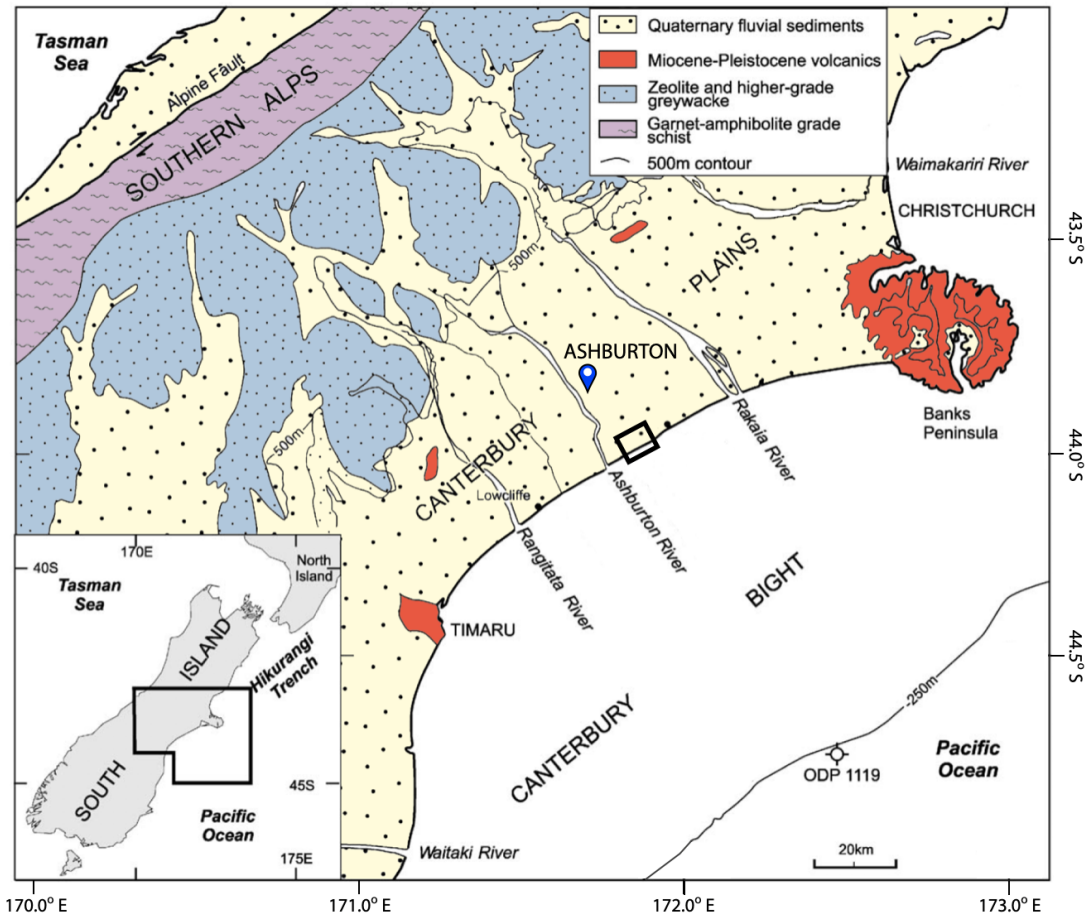

Figure 3.1: Geological map of the Canterbury Plains, South Island of New Zealand. The study site is identified by the dark rectangle and Ashburton town is shown as the blue-white symbol NW of the study site. Ocean Drilling Program site 1119 is also shown. Modified after Browne and Naish [2003].

3.4 Methods

This study utilizes the near-surface TDEM geophysical method to identify spatial relationships between groundwater discharge conduits and locations of coastal gullies along the Canterbury coast. The TDEM measurements were carried out using the Geonics G-TEM system consisting of a portable battery-operated transmitter-receiver (TX-RX) console, a TX antenna deployed as a loop of wire laid on the ground, with the RX coil set up in the center of the TX loop, for a central-loop sounding, or else set up at a designated distance from center of wire loop. The latter configuration is used for fixed-offset sounding or profiling, which is termed "slingram" in the EM

geophysics literature [Tabbagh, 1986, Kamm et al., 2013]. In this work, we used 4 turns of wire loop, covering a 10×10 m^2 area, carrying out 1 A of current. A TX-current step-off waveform was used to excite eddy currents in the subsurface The resulting signal measured at the RX coil is proportional to the time rate of change of the decaying secondary vertical magnetic field, the decay rate being diagnostic of the subsurface resisitivity. All measurements were acquired in the standard 20 time-gate mode, corresponding to investigation depths of 60–100 m. The depth of investigation also depends on the TX dipole moment [Spies, 1989], which is a product of the loop size, current and its number of turns, in addition to the subsurface conductivity, the RX sensitivity and background noise level [Geonics, 2016]. In field operations, the equipment was deployed as shown in Figure 3.2. Further information about the operating principles of TDEM may be found in [Everett, 2013, Pondthai et al., 2020].

In order to measure morphological changes over time of the coastal cliffs and gullies at the study site, unoccupied aerial vehicle (UAV) surveys were carried out using DJI Mavic Pro and DJI Phantom 4 Pro drones. These devices are able to determine both horizontal locations and elevations to cm accuracy. The method used for detecting gully erosion rates include analysis of othophotos, digital elevation models (DEMs), and slope gradient maps from the UAV data, along with aerial photographs dating back to 2004 from Google Earth databases [Micallef et al., view].

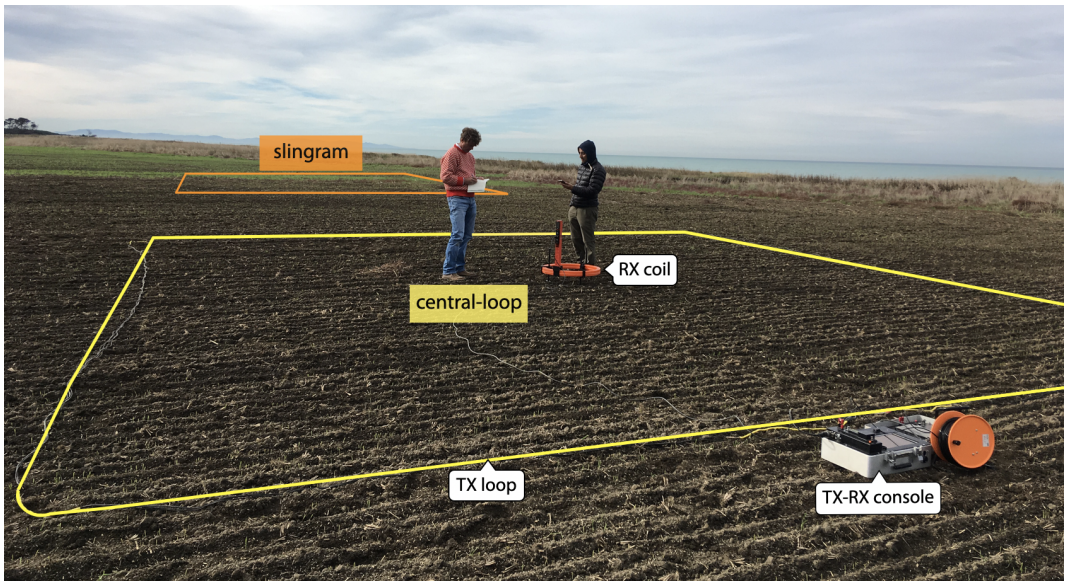

Figure 3.2: Field deployment of Geonics G-TEM geophysical equipment at the Canterbury Plains, South Island of New Zealand. The yellow rectangular indicates the location of the square TX loop wire with the RX coil placed at the center, as shown in the foreground, illustrates the central-loop configuration. The orange TX loop in the background, with RX coil set up outside ∼30 m away from the center of TX loop, illustrates a slingram-mode survey configuration.

3.4.1 Data Acquisition

The geophysical survey conducted using the TDEM method was performed in May 2019. At each sounding location, the wire TX loop was laid out on the ground. Then the RX coil with its pre-amplifier was set up at a fixed 30 m offset from the center of TX loop. The portable TX console was placed just outside the TX loop, while the RX console was placed ∼5 m away from the RX coil, as recommended by Geonics to avoid signal interference. The TX and RX consoles were then connected using a reference cable to enable synchronization of the TX and RX signals. An abrupt ramp-off current waveform was passed through the wire loop using the signal generator in the TX console. The resultant signal due to induction of eddy currents in the ground was received by the RX coil and recorded at the RX console. To improve signal-to-noise ratio, this signal was averaged over several thousand waveform repetitions with 8 s of integration time. The overall time to acquire each sounding response at a given station was less than 5 min. Then the TX loop and RX

coil were picked up, along with the consoles, and moved forward to the next sounding location. The midpoint between the center of the TX loop and RX coil is designated as the location of each sounding, and its coordinates were recorded by a handheld GPS. The operating frequency is in the kHz range, whereas the main power supply in New Zealand is 50 Hz and mobile phones operate at $\sim$10 GHz. No other ambient environmental electromagnetic disturbances were detected in this very quiet rural setting. TDEM is a non-invasive technique and does not cause any significant disturbance to the flora and fauna in the environment.

Four slingram transects were conducted inland across the heads of gullies and one transect was carried out along the beach using the 10 m $\times$10 m TX loop. The TX-RX pair was moved keeping a fixed 30-m TX-RX offset along the designated traverse line, with 2 m station spacing for the inland surveys and 5 m station spacing for the profile on the beach. All profiles are oriented approximately NE-SW, parallel to coastline. The lengths of each survey are respectively 168, 196, 260, 120, and 44 m for profiles May15-1, May15-2, May16, May17-1, and May17-2 (see Figure 3.3). In addition, a total of 43 central-loop soundings were made around the southern section of slingram profile May15-2. An additional across-shore survey was carried out on the plains inland from two coastal indentations using a single-turn 40$\times$40 m square TX loop with central-loop figuration, as shown by the SE-NW directed white line in Figure 3.3.

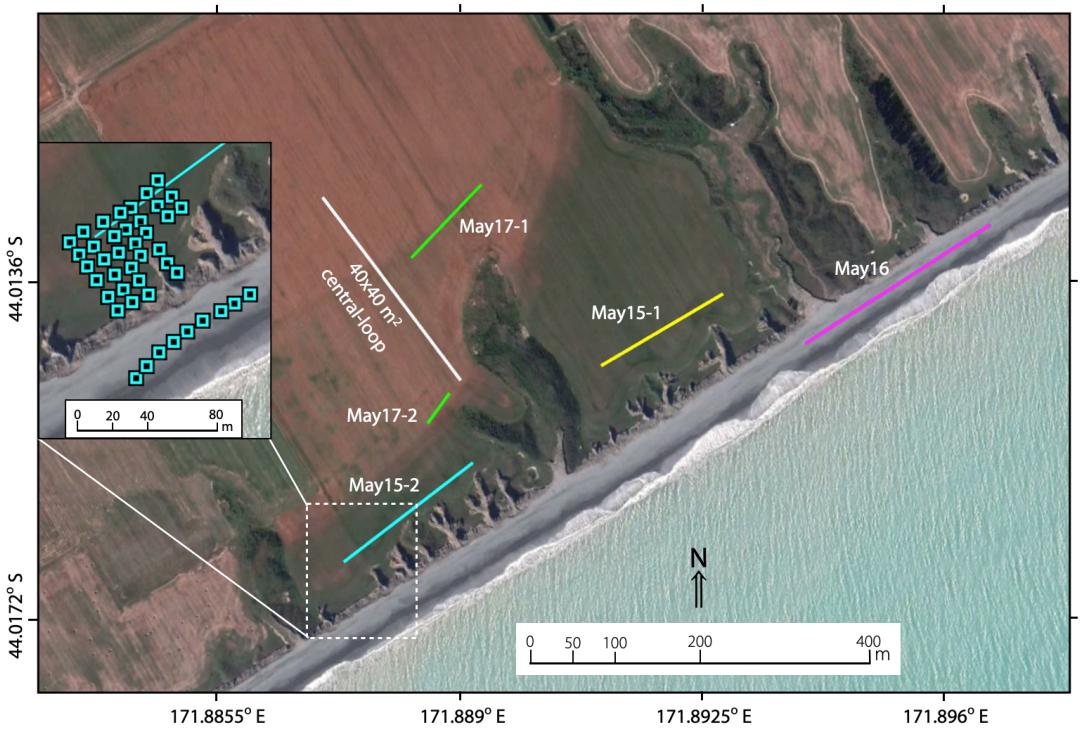

Figure 3.3: Location of the TDEM surveys showing the transects from 2019 (image source: Google Earth). Solid lines marked in yellow, cyan, magenta, and light green denote the position and orientation of each slingram-mode profile. These transects are named by the date of survey. An across-shore central-loop survey with 40 m×40 m TX loop is shown as the solid white line. In addition, the location of some additional central-loop soundings are marked as the cyan-and-black symbols.

3.4.2 Data Analysis

An inversion of G-TEM transient responses was performed using the IXG-TEM software from Interpex Limited (Golden, CO, USA). Inversion is the process of converting a G-TEM sounding curve into a smoothly-varying profile of electrical resistivity with depth. An attempt was made to invert the transient G-TEM sounding curves, from both the slingram-mode and central-loop surveys, into a smooth model of electrical resistivity vs. depth, based on a well-known iterative 1D Occam regularization algorithm [Constable et al., 1987]. A representative 1D inversion result along slingram profile May15-1 is shown in Figure 3.4. The resistivity model is presented in the right panel, while the computed response along with the actual data points, plotted as blue

plus/minus symbols, are displayed on the left. The best calculated smooth depth profile clearly does not fit with the measurements. In the resistivity model at right, there is a layer at depths below $\sim$11 m showing extremely low resistivity $\sim 10^{-4}$ to 10^{-3} Ωm. Such low values of resistivity, much lower than that of pure seawater, are clearly not reasonable. The inability to fit the slingram responses with a 1D model suggests that the geoelectrical subsurface structure is strongly heterogeneous within the footprint of the G-TEM transmitter. Strong 3D subsurface heterogeneity is also supported by sign reversals that are present in almost all the central-loop sounding curves. Sign reversals cannot be generated using a central-loop configuration by electromagnetic induction in a simple 1D layered Earth model. Subsequently, we cannot rely on 1D inversions of either the slingram-mode or central-loop data in this 3D geological environment.

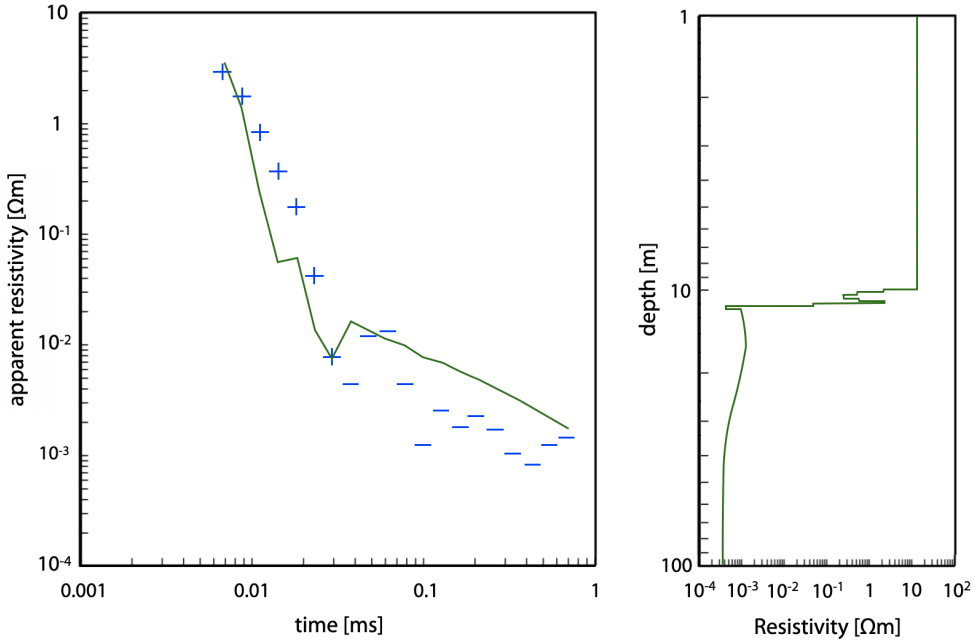

Figure 3.4: Example of 1D inversion result for the G-TEM sounding curve recorded at 60 m along profile May15-1. (left) The computed response displayed as the curve passing through the data points. The latter shown as blue plus/minus symbols for positive and negative received responses, respectively. (right) The corresponding resistivity-depth profile, obtained by regularized inversion, is shown as the dark green line.

3.4.2.1 2D Forward Model

In this study, we use a well-tested, in-house FORTRAN 3D forward modeling program to compute 2D forward responses based on an inductively-coupled loop source laid on the ground. The computation of time-harmonic (i.e. frequency-domain) EM responses of 2D geoelectrical models is performed using a finite-element (FE) approach of the governing Maxwell equations in the magnetoquasistatic regime [Badea et al., 2001, Stalnaker et al., 2006]. A 2D geoelectrical model is one in which the electrical resistivity of the subsurface is allowed to vary in the vertical and one horizontal (across-strike) direction, but remains invariant in the other horizontal direction (along-strike). The FE algorithm generates a rectangular mesh that is used to discretize 1D, 2D and 3D structures, buried within in a uniform background medium, by defining rectangular prisms or slabs, and assigning them certain dimensions, locations, and electrical conductivities (the inverse of resistivities). A series of 2D frequency-domain responses is then computed for a wide range of TX operating frequencies. The resulting responses, as a function of frequency, are then inverse-Fourier transformed to obtain the step-off time-domain response. A Padé summation method is used to execute the discrete inverse Fourier transform [Chave, 1983, Guptasarma and Singh, 2003]. Implementation details about setting up the simulations, assigning all model parameters including survey configuration, designating TX and RX positions, and mesh generation including specification of the number of nodes, mesh size, and modeling-domain limits, are explained elsewhere [Pondthai et al., 2020].

Our finite-element analysis of the governing magnetoquasistatic Maxwell equations in the frequency domain is formulated in terms of secondary magnetic vector and electric scalar potentials. Primary potentials are specified by the analytic solution for EM induction due to a loop source deployed over a homogeneous half-space with a constant conductivity. The primary potentials are added to the calculated secondary potentials in order to obtain the total response at the prescribed frequency. At a given receiver location, such as the center of the RX coil, the total vertical magnetic field component is calculated by numerical differentiation of the computed total potentials. This procedure is repeated for a number of frequencies spanning several decades, thus building up the

frequency-domain response. For this study, responses are evaluated at 43 logarithmically-spaced frequencies, at 6 frequencies per decade over the range 10^1–10^8 Hz. After the inverse Fourier transform into the time-domain, the resulting computed transient response may be directly compared with the corresponding G-TEM sounding curve measured in the field.

3.5 Results

As previously mentioned in the Methods section, attempts were made to fit a 1D Earth resistivity depth profile to slingram responses acquired at the study site. However, these attempts were unsuccessful which indicated that the subsurface geoelectrical structure could not be a simple horizontal-layered medium.

Even though the individual slingram-mode response cannot by fit using 1D inversion software, we can present time-gate plots in terms of the amplitude of response, for all transects to explore the subsurface lateral variability of acquired TDEM data. The time-gate profile is a plot as a function of distance along the transect of the G-TEM ramp-off voltage at the time after a current in TX has been shut off as a gate number. The interesting features are observed at transect May15-1, marked as a yellow line in Figure 3.3, where is located upslope of small-recently eroded gullies in the NE part of the study site (see Figure 3.5). Near the middle of this transect there is a distinctive peak that is much higher than the background. The peak is $\sim$24 m wide and it appears in a similar fashion on each of the gates 1 through 7, although it cannot be clearly seen after gate 7.

Herein, this paper focuses on analysis of the first half section of the slingram May15-1 transect, progressing in the NE to SW direction. Only this small part of the entire dataset is analyzed due to the heavy computational requirements to conduct 2D TDEM forward modeling of field datasets; the remainder of the dataset will be analyzed in a later publication.

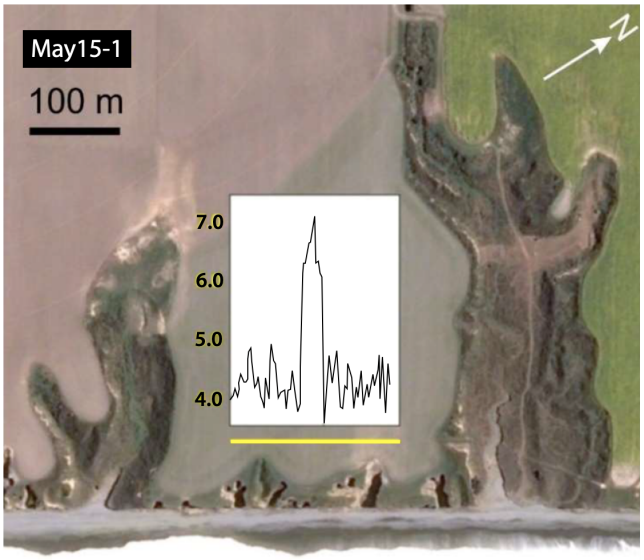

Figure 3.5: First-time-gate profile of G-TEM slingram transect May15-1 (units in black are 10^{-10} V m^{-2}). Source of background imagery: Google Earth. A yellow line marks a slingram transect, the length of which can be determined from the scale bar. Modified after Micallef et al. [in review].

3.5.1 2D Model Scenario

The pseudo-2D inversion result is obtained by stitching together smooth 1D depth profiles from the deep-probing 40 m$\times$40 m central-loop soundings employed on the top of the cliff (see the long, across-shore white line in Figure 3.3). It is used as an initial resistivity distribution in an attempt to find a 2D geoelectrical model that could fit the May15-1 slingram data. The 1D stitched section (see Figure 3.6) is of length 280 m and reveals a conductive region appearing at $\sim$10 m deep with $\sim$8–10 m thickness along the entire transect. The conductive zone is characterized by resistivity values of $\leq$100 Ωm. The zone is interpreted in [Weymer et al., 2020] as a continuous groundwater conduit, i.e. groundwater flow path toward the coast. Above and below the low-resisitivity zone, the host formation is much more resistive, attaining values of $\sim$1000 Ωm.

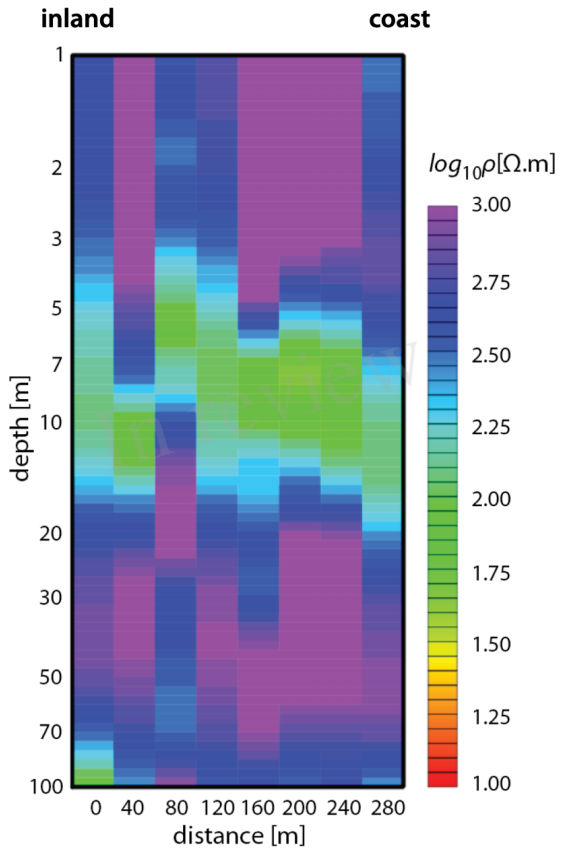

Figure 3.6: Plot of the 40 x 40 m G-TEM 1D stitched inversion profile from inland (0 m) moving seaward to the head of gully (280 m). Reprinted from Weymer et al. [2020] with permission. Refer to Figure 3.3 for the survey location.

At Figure 3.7, left is a 2D geoelectrical model containing a subsurface slab of resistivity ρ_1 = 10 Ωm, height 8 m, width 12 m, and top-of-slab depth 6 m. The resistivity of the host material is ρ_0 = 1000 Ωm. The center of the slab is located 26 m from the center of the TX loop. The strike length of the buried slab, in and out of the plane of the paper (along-strike, y-direction), is theoretically infinite, but practically it extends along-strike for ±40 m long according with the limits of the computational domain. At the right of this figure, for the model shown at the left, is the FE-computed response in the solid and dashed lines. The green filled and unfilled symbols indicate the measured G-TEM slingram response from the station located at 6 m from the start of transect May 15-1. The solid line/filled symbols represent a positive G-TEM response, while the dashed

line/unfilled symbols represent a negative G-TEM response. Note that the FE-computed response of this slab model provides a good match at early times to the measured response, especially reproducing the transition from the positive to negative response at time-gate 7 ($\sim 3 \times 10^{-5}$ s after TX ramps off). The fit to the late-time response is not as good; this is further discussed below.

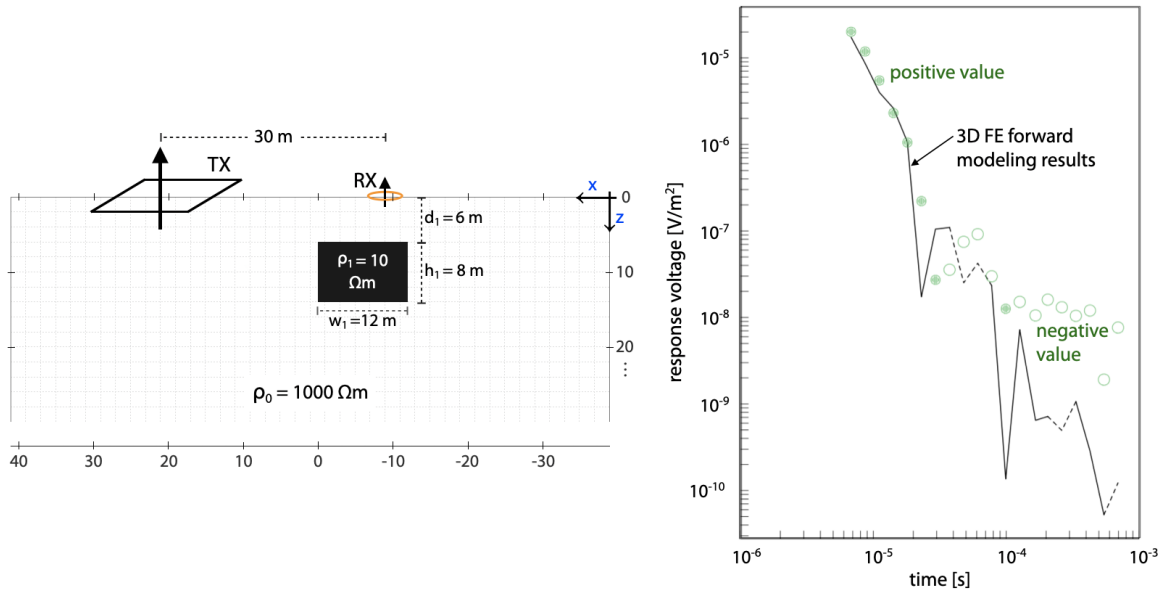

Figure 3.7: 2D electrical conductivity model containing a single buried slab (left) generating a good-fit slingram response (right), as illustrated by the black solid line (positive value) and dashed line (negative value). Data are from station 4 on transect May15-1, 6 m from the start of the transect. Overall misfit is 115%, decreasing to 29% for the first six time-gates

At some distance from the starting point of the May15-1 transect, the modeling results show that the single-slab model is unable to provide a good fit to the G-TEM responses. The fit of the one-slab model degrades at stations located further from the start of the transect. After much trial and error, it was found that a two-slab model produces a better fit to the data. All model adjustments in this study are made by trial and error because the available computational resources are insufficient to implement an automated inversion process. Such 2D or 3D algorithmic inversion is beyond the scope of this study, but is definitely recommended for future work. The CPU time required to compute a single controlled-source electromagnetic (CSEM) response for a model at

one frequency ∼2–3 min on 2.0 GHz dual-core Intel core i5 workstation with 8 GB of RAM.

An example of the measured G-TEM and FE-computed responses at the station located 22 m from the start of the May 15-1 transect is shown in Figure 3.8. At this station, the single slab (of resistivity ρ_1) of the initial model is now located to the right of the RX coil. Modeling trials show a good fit if this slab is supplemented by a second slab (of resistvity ρ_2) with slightly different model parameters. The parameters for the newly-added slab, which is located directly beneath TX loop, are given by following: resistivity 11.1 Ωm, height 8 m, width 12 m, and top-of-slab buried depth 6.6 m. The FE-computed EM response of the two-slab model is shown as the solid/dashed lines in the right panel of Figure 3.8. The introduction of the second slab greatly improves the fit to the observations. Again, a change in sign of the ramp-off voltage from positive to negative starts at time-gate 7. Note that the FE-calculated response of a model containing only the second slab (the one at the left) does not produce such a good fit; both slabs are needed to fit the data.

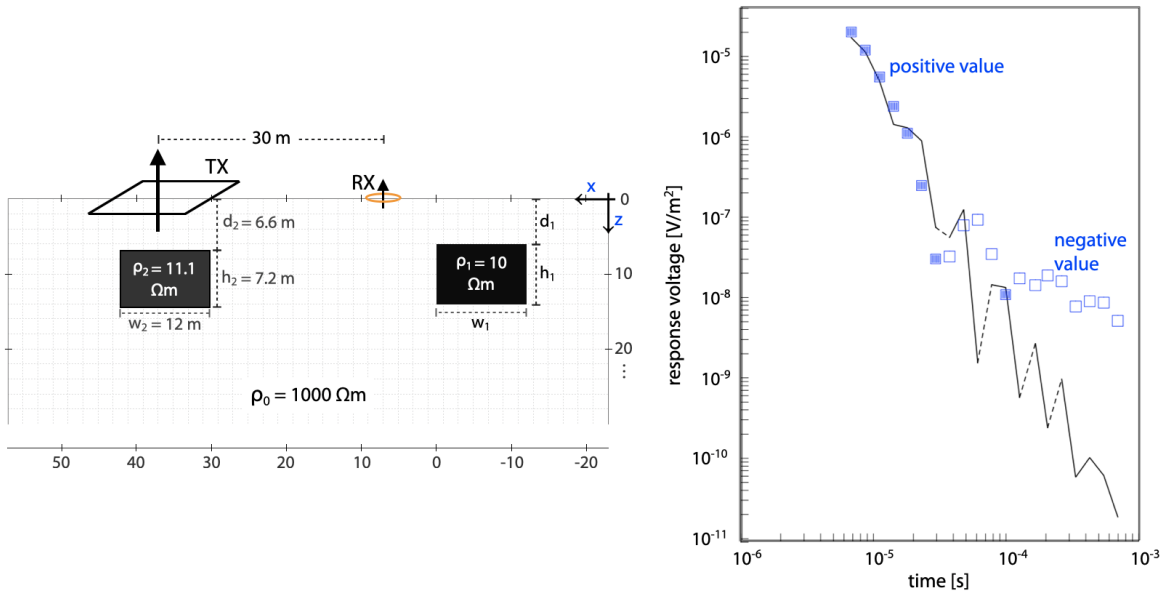

Figure 3.8: 2D resistivity model with two slabs (left) generates the FE-computed voltage that fits the response at station 22 m on transect May15-1 with a overall misfit 150%, reducing to 41% over the interval time-gates 1-6 (right). In the right panel, the solid lines and filled square symbols correspond to positive responses; the dashed lines and unfilled symbols correspond to negative responses

3.5.2 2D Multi-layered Model Scenario

Multilayered groundwater conduits discharging to the sea along the Canterbury coastline were proposed in [Weymer et al., 2020]. In that study, the combined results from EM measurements using three different geophysical instruments reveal a geoelectrical image interpreted in terms of subsurface hydrological variations from the surface down to $\sim$80 m depths along the mixed sand/gravel beach adjacent to the Ashburton River mouth. The interpretation suggests that a series of highly conductive zones at various depths and sizes are indicative of buried high-permeability groundwater conduits such as lenses of well-sorted gravels within the braided river deposits. Moreover, the forward modeling results presented in the previous sections of this paper from one or two buried slabs located at a single depth shows the difficulty in fitting late-time responses (see Figure 3.7 and 3.8). Late-time responses are associated with deeper structures since the G-TEM-activated electromagnetic field diffuses further into the subsurface with increasing time after ramp-off.

An example of fitting late-time G-TEM responses with a multi-layered slab model is now given. At station 90 m along transect May15-1, (Figure 3.9), the center of initial slab (resistivity, ρ_3) is located slightly to the left of the RX coil, at burial depth 10 m. The model is supplemented by a deeper slab (resistivity, ρ_4) of the same lateral dimensions but slightly higher resistivity. The additional slab is located 5 m to the right of slab 3 and buried 16 m deeper. The FE-computed TDEM responses of the single-slab (the shallower one) and two-slab models are displayed as the black and red solid/dashed lines, respectively. It is evident that adding the deeper slab improves the fit to the in-field measured response; in particular, the misfit is reduced by 38%.

The computed misfit (relative error) at each measurement location along transect May15-1 is plotted in Figure 3.10 for the single-slab and two-slab models. These misfits are shown in the black and blue lines, respectively. The misfits of the first 6 time-gates and the misfits of all 20 time-gates of the G-TEM response, for all stations, are displayed as dashed and solid lines, respectively. The relative errors of the 2D models have been calculated (due to computational limitations) for only the first 22 stations of the May15-1 transect (see yellow survey line in Figure 3.3). The reader should note that the misfit over the first 6 time-gates at any given station is much smaller than the

misfit over all 20 time-gates, even taking into account the normalization of the misfit function by the number of stations. The important point is that the 2D models still present difficulties to fit the late-time observations signals after the sign-reversal appears in the recorded responses (typically after time-gate 7). This result is consistent with the actual geoelectrical structure of the Earth beneath the G-TEM measurement stations being fully 3D rather than a simple 2D structure, like as the ones whose responses we have been able to evaluate in this paper.

It is interesting to relate our G-TEM-inferred multilayer groundwater conduits to the dynamic geomorphology of the coastal gullies as they have evolved through time. This paper represents a tentative first step in that direction. To observe long-term landscape changes, satellite imagery from 2004–2019 was used to map three newly formed gullies adjacent to the May15-1 survey line. Much of the recent erosion is evident in the Google Earth image taken on August 26 2013 and marked by the orange lines in Figure 3.11a. It is assumed that the formation of new gullies followed a heavy rainfall event with a total of $\sim$170 mm in the third week of June 2013 [Canterbury, 2019]. Detection of short-term morphological changes was achieved by comparing orthophotos and DEMs generated from UAV data acquired between May and October 2017 [Micallef et al., view]. There are found to be 6 newly-enlarged gullies along the sea cliffs $\sim$25–40 m SE of transect May15-1 (Figure 3.11a; show in red). The enlargements are typically elongated and occasionally widened or branched. The proposed 2D geolectrical model, with the multi-layer slabs, and representing our inference about the subsurface architecture beneath the first half of transect May15-1, covering survey length of $\sim$90 m, is illustrated in (Figure 3.11a). This model is obtained by combining the 2D forward model results from the tested scenarios of the single-slab, two-slab and multi-layer slab models, as shown in Figure 3.8 and 3.9, respectively.

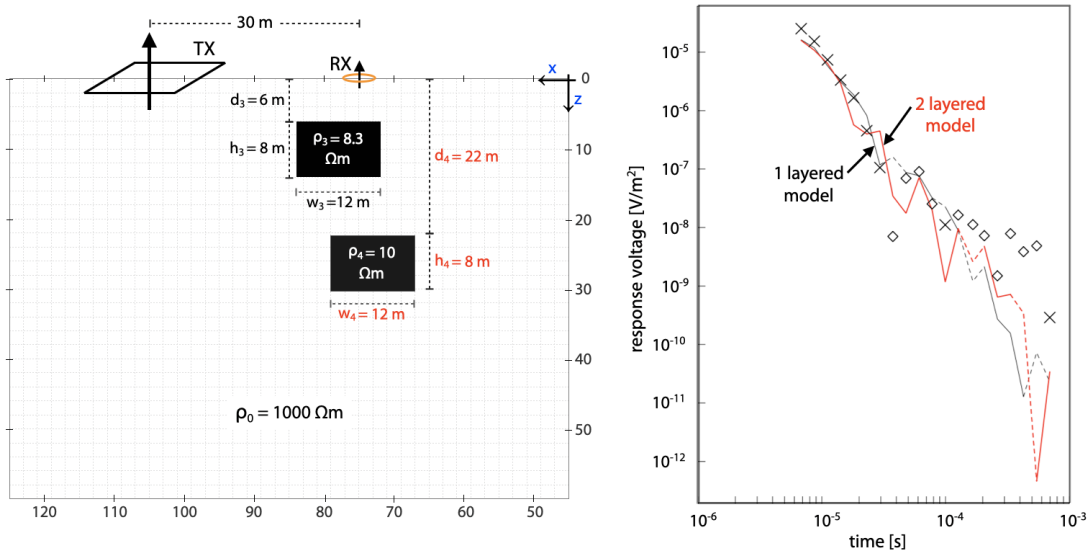

Figure 3.9: Multi-layered resistivity model with two slabs buried at different depths (left). The FE-computed G-TEM voltages at station 90 m on transect May15-1 generated from the resistivity model at left (right). The calculated EM response from the single-slab model is marked in black, while the computed voltage resulted from two-slab model is shown in red. The solid portion and cross symbols correspond to positive responses; the dashed portion and unfilled diamond symbols correspond to negative responses.

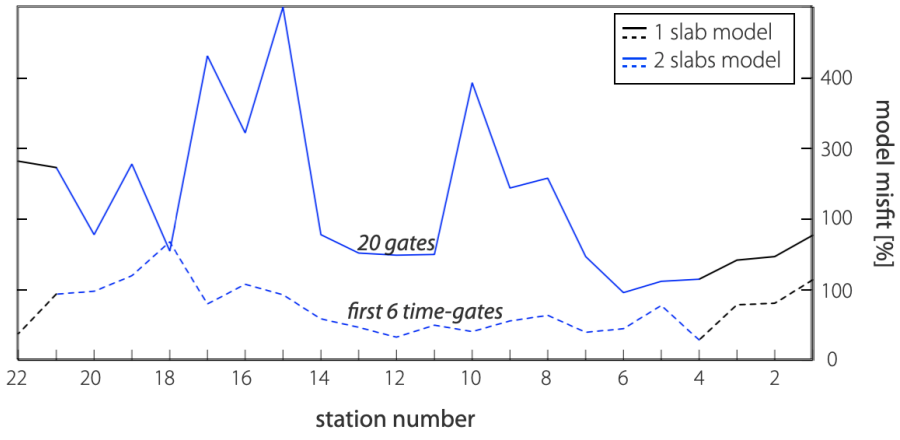

Figure 3.10: Misfit of single-slab (solid and dashed black lines) and two-slab model (blue lines) responses along May15-1 transect; the data acquisition proceeded from right to left (also see Figure 3.11). Dashed and solid lines represent, respectively, the relative errors of FE-computed vs. G-TEM measured responses at each station over time-gates 1-6, and time-gates 1-20. The misfits at only the first 22 stations covering 42 m of the transect are shown.

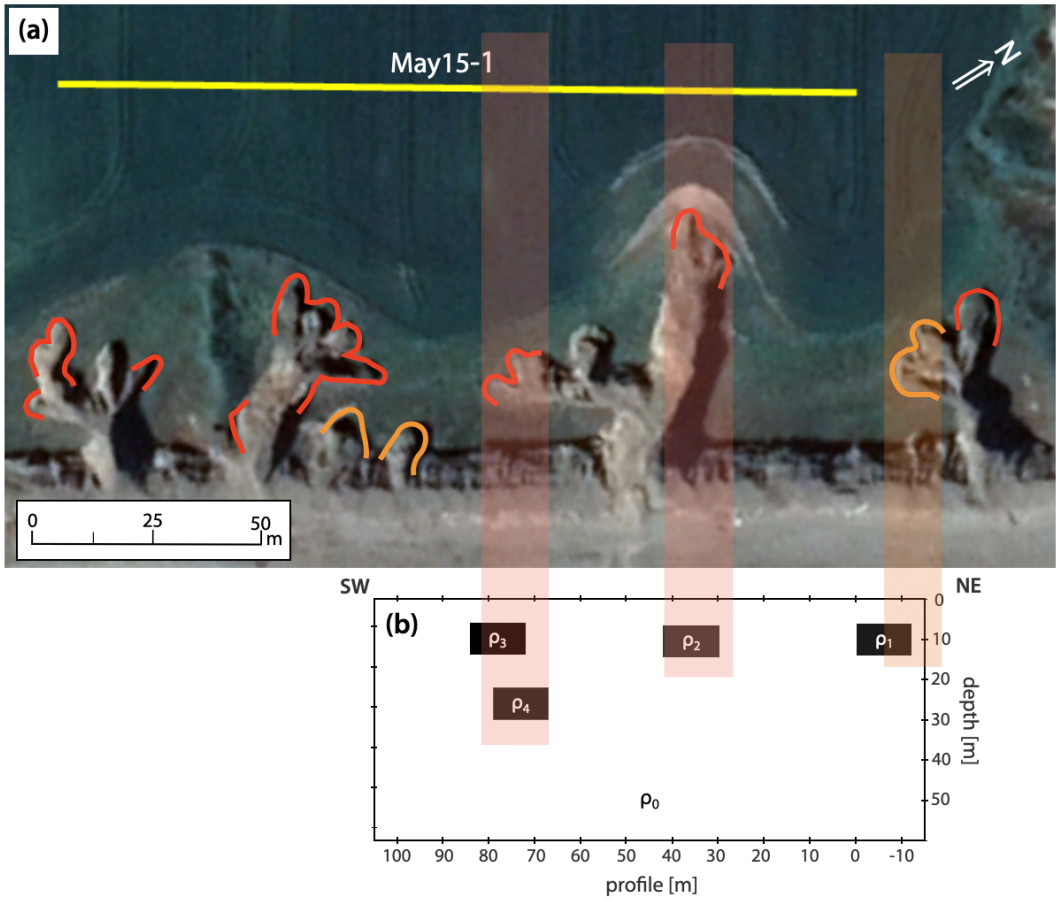

Figure 3.11: a) Satellite imagery of transect May15-1 and adjacent coastal gullies, modified after Micallef et al. [in review]. Recently eroded areas are highlighted by red and orange lines. (b) The preferred 2D subsurface resistivity distribution model with four possible slabs beneath the first half of May15-1 transect and reaching to depth 60 m. Shaded areas in red and orange are the locations of observed gullies projected onto the survey profile and the preferred model.

3.6 Discussion

A previous geophysical study along the Canterbury coast mapped groundwater pathways beneath braided alluvial deposits along the coast [Weymer et al., 2020]. Their results show that co-located measurements using three different EM instruments were effective in characterizing hydrological variations and detecting multiple stacked electrically conductive zones. These were suggested to be indicative of high permeability conduits below the beach. A comparison between their results and a recent marine controlled-source electromagnetic survey [Micallef et al., 2020], which

indicated the presence of a large offshore freshened groundwater system in the Canterbury Bight, points to the existence of an onshore-offshore groundwater connection. Additionally, a recent study using the integration of geochronological analyses, remote sensing surveys, near-surface geophysical measurements, and geotechnical modeling reveals that the gully initiation is an episodic process related to groundwater flow, but triggered by intensive rainfall periods [Micallef et al., view]. This process is a key mechanism shaping the sea cliff geomorphology at the study site.

In this study, we can explore possible scenarios for a groundwater discharge model that matches the G-TEM observations along profile May15-1. The failure to fit a 1D resistivity depth profile and the locations of the slabs in our 2D geoelectrical models point to evidence of a seepage system focusing groundwater flow through preferential pathways. There is a spatial relationship between the locations of recently-eroded coastal gullies and the G-TEM-inferred locations of groundwater discharge conduits beneath the braidplain alluvial sediments. Based on the geophysical EM investigation, the preferred 2D TDEM model in Figure 11b demonstrates that subsurface spatial geoelectrical heterogeneity is found at this study site. The model derived from the May 15-1 dataset shows that the subsurface resistivity distribution may be characterized by distinct zones under the plains with elevated conductivity in the range $\sigma \sim$0.09–0.12 S/m. These conductive bodies are interpreted herein as groundwater discharge conduits, corresponding to the hydrological pathways through the sea cliffs and out to the sea. Our results are in agreement with hydrological field observations [Wilson, 1973] of the Canterbury Plains which point out the presence of ancient buried river channels of high permeability in the plains. These ancient channels focus preferred flow paths in the braided alluvial architecture [Wilson, 1973]. Paleochannel conduits likely form a complex network at all depths in the alluvial deposits, acting as pipelines to the seepage features. Moreover, our 2D geoelectrical model comprising slabs of 12 m width agrees with the characteristics of the high permeability conduits defined as secondary channel fills, which can occur with the sizes ranging from $\sim$10 m wide to tens of meters, suggested by [Moreton et al., 2002].

The first potential discharge conduit (resistivity $\rho_1 = 10\,\Omega$m) located at the NE part of the profile May15-1 may correlate with the newly formed gully of August 2013, which is marked with the

orange line, and situated ∼10 m from the start of transect. At a distance of 30–42 m, the location of an active, recently-formed (< 3 years ago) gully coincides with the position of the second G-TEM-interpreted conduit of resistivity ρ_2 = 11.1 Ωm. The third and most conductive conduit (ρ_3 = 8.3 Ω m) located near the middle of the transect corresponds to the location of the distinctive peak in the early-time gates plot reported in [Micallef et al., view] (see Figure 3.5). The deeper conduit, (resistivity ρ_4 = 10 Ωm), appears at 20–30 m depths, and is of slightly higher resistivity than that observed in the conduit at shallow depth (ρ_3 = 8.3 Ωm). This conductive zone in the lower plains is likely caused by relatively fresh water-saturated secondary channel fills that focuses groundwater flow offshore under the coastal bluffs. The erosion observed along this transect is evidenced by the elongation of the two gullies marked in the red lines. The shaded areas in Figure 3.11 are potentially associated with the presence of all four inferred conduits. It should be noted that our imaging result shown here covers a relatively short distance (<100 m) and at the present time, due to computational limitations, are not able to describe the architecture of the conduit network at larger scales.

3.7 Conclusions

This study demonstrates the utility of the TDEM geophysical method along with forward modeling as a means to evaluate the connections between groundwater conduits and the coastal gullies in terms of directing freshwater discharge offshore. In this paper, we image possible scenarios for a groundwater discharge beneath braided alluvial deposits along the mid Canterbury coast. The final preferred 2D model provides information to depth of 60 m, covering a length of ∼100 m and shows diagnostic spatial variations in subsurface electrical resistivity at this study site. The geophysical modeling provides a basis for determining important characteristics of the high permeability groundwater conduits that fit our observations, namely a series of high electrical conductive zones at various depths such as lenses of well-sorted sediments. Each of these conductive bodies has been identified, and its position might possibly correlate with either newly formed or elongated coastal gullies observed in the site. In summary, we do not have the capability to characterize all the groundwater discharge conduits at the eastern Canterbury coast study site. However, we still

have additional G-TEM datasets available for further analysis. Herein, our main accomplishment is to demonstrate the capacity of the geophysical EM imaging method and to make an interpretation that it is reasonable from the hydrogeological perspective.

The EM imaging method that we used can be applied across the entire the Canterbury plains to better constrain the geometry, dimensions and spatial distribution of terrestrial subsurface water discharge pathways providing valuable information for future water management of the groundwater reserves of South Island, New Zealand. Moreover, this imaging technique has the capability of solving this similar type of problem in the other places, e.g., Alaska (USA), Florida Panhandle (USA), Kalahari (South Africa), and Obara area (Japan).

4. WORK CONTRIBUTED AS A CO-AUTHOR

I have collaborated with international research institutions (MARCAN project[1] and GEOMAR) doing multidisciplinary research and participating in field projects (Malta, New Zealand). In addition to my research, I have contributed to another two manuscripts (as a co-author), which are included in this chapter by providing my expertise on TDEM survey, analysis and interpretation.

4.1 Multi-layered high permeability conduits connecting onshore and offshore coastal aquifers

All contents in the section 4.1 are from the article[2] published in open-access journal *Frontiers in Marine Science*.

4.1.1 Authors

Bradley A. Weymer[a,*], Phillipe A. Wernette[b,c], Mark E. Everett[d], **Potpreecha Pondthai**[d], Marion Jegen[a], Aaron Micallef[a,e]

[a] GEOMAR–Helmholtz Centre for Ocean Research, Kiel, Germany

[b] School of the Environment, University of Windsor, Ontario, Canada

[c] Pacific Coastal and Marine Science Center, United States Geological Survey

[d] Department of Geology and Geophysics, Texas A&M University, Texas, United States

[e] Marine Geology and Seafloor Surveying, Department of Geosciences, University of Malta, Malta.

4.1.2 Abstract

Groundwater resources in coastal regions are facing enormous pressure caused by population growth and climate change. Few studies have investigated whether offshore freshened groundwater systems are connected with terrestrial aquifers recharged by meteoric water, or paleo-groundwater

[1] www.marcan.eu.

[2] Reprinted with permission from Weymer, B. A., Wernette, P. A., Everett, M. E., Pondthai, P., Jegen, M. & Micallef, A. (2020). Multi-layered high permeability conduits connecting onshore and offshore coastal aquifers. *Frontiers in Marine Science. 7*, 903.

systems that are no longer associated with terrestrial aquifers. Distinguishing between the two has important implications for potential extraction to alleviate water stress for many coastal communities, yet very little is known about these connections, mainly because it is difficult to acquire continuous subsurface information across the coastal zone. This study presents a first attempt to bridge this gap by combining three complementary near-surface electromagnetic methods to image groundwater pathways within braided alluvial gravels along the Canterbury coast, South Island, New Zealand. We show that co-located electromagnetic induction, ground penetrating radar, and transient electromagnetic measurements, which are sensitive to electrical contrasts between fresh (low conductivity) and saline (high conductivity) groundwater, adequately characterize hydrogeologic variations beneath a mixed sand gravel beach in close proximity to the Ashburton River mouth. The combined measurements - providing information at three different depths of investigation and resolution - show several conductive zones that are correlated with spatial variations in subsurface hydrogeology. We interpret the conductive zones as high permeability conduits corresponding to lenses of well-sorted gravels and secondary channel fill deposits within the braided river deposit architecture. The geophysical surveys provide the basis for a discharge model that fits our observations, namely that there is evidence of a multilayered system focusing groundwater flow through stacked high permeability gravel layers analogous to a subterranean river network. Coincident geophysical surveys in a region further offshore indicate the presence of a large, newly discovered offshore freshened groundwater system, suggesting that the offshore system in the Canterbury Bight is connected with the terrestrial aquifer system.

Keywords: coastal hydrogeophysics; Groundwater; ground penetrating radar; electromagnetic induction; transient electromagnetics

4.1.3 Contributions as Co-Author

I provided 1D stitched TDEM section of the shallow conduits structure potentially discharging offshore and helped in building the conceptual discharge model along the Canterbury beach.

4.1.3.1 TDEM surveys

On May 16, 2019 from 9:12 to 12:10 (local time) during a rising tide, we conducted a 185 m G-TEM survey along a shorter segment of the same survey EMI/GPR line previously collected in May, 2017 (Figure 4.1). The TEM measurements were carried out using the Geonics (Canada) G-TEM system. The survey parameters were 4 turns, 10 m$\times$10 m TX loop and the TX current output of 1 A. The G-TEM was operated in an fixed-offset sounding or slingram configuration in which the RX coil was placed 30 m from the center of the TX loop and the TX-RX pair moved along the transect at 5 m station spacings for 38 stations, maintaining the 30 m offset. All soundings data were collected in the 20-gate mode with acquisition interval of 6×10^{-6} s to 8×10^{-4} s (after ramp-off), corresponding to investigation depths of $\sim$80 m. This configuration is comparable to EMI profiling that was performed with the GSSI Profiler EMP-400 system. At each station, a consistent 1D smooth inversion model of electrical resistivity vs. depth based on the iterative Occam regularization method [Constable et al., 1987] was performed using the IXG-TEM software from Interpex Limited.

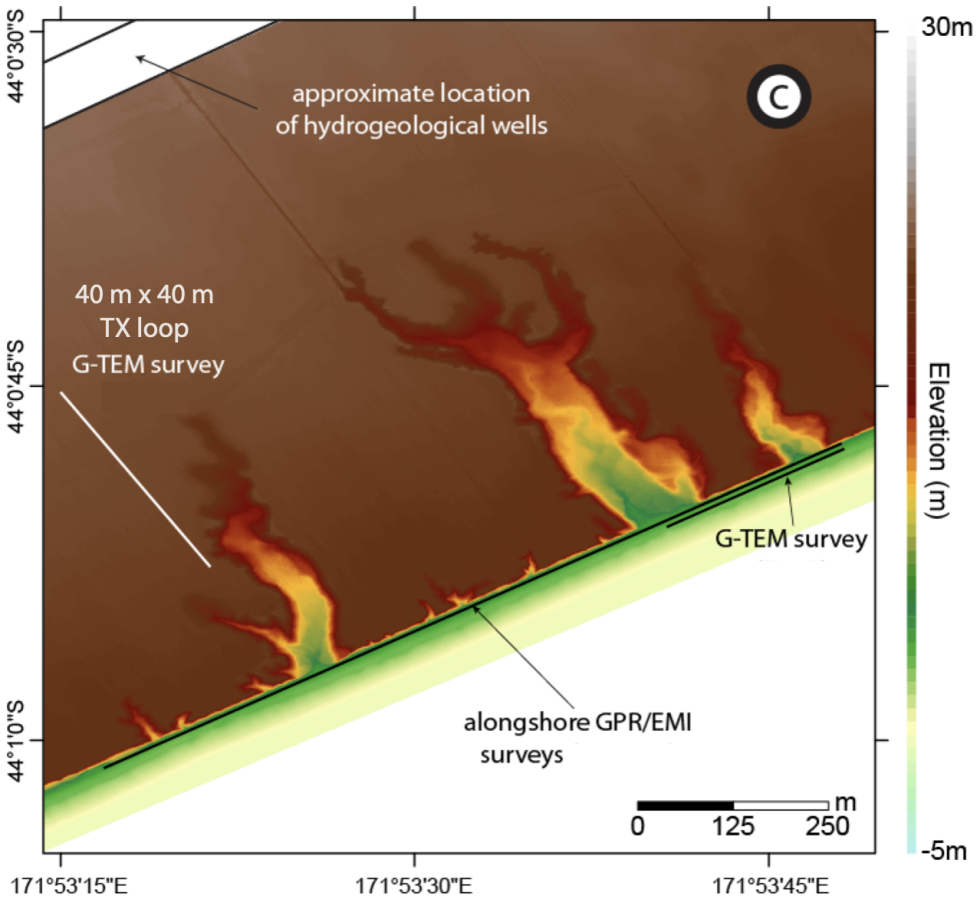

Figure 4.1: DEM of the study area showing the georeferenced locations of the GPR, EMI, and G-TEM surveys. Approximate locations of the closest hydrogeological wells ($\sim$1 km inland from the coastline are indicated in the upper left corner. Reprinted from Weymer et al. [2020] with permission.

The slingram configuration was used for the beach profile since no central-loop soundings using the 10$\times$10 m square loop measured on the beach could be fit by a 1-D model. An example of a typical 10 m$\times$10 m central-loop sounding and the best 1-D model response showing $\sim$200$\%$ RMS misfit is shown in (Figure 4.2a). The four different symbols in Figure 4.2 represent the four repetitions of a sounding. We repeated each measurement four times in order to estimate the scatter in the response. In low-noise environments, all four sets of data should sit on top of each other, but if there is noise (e.g., random, ambient EM noise from the atmosphere or from anthropogenic activity) there will be some scatter. The scatter is especially prominent at the later

time gates where the signal from the deep eddy currents in the ground has become small. The poor fit of the central-loop soundings is likely due to the strong heterogeneity generated by highly contrasting electrical conductivity zones at shallow depths beneath the beach. These contrasts could be related to freshwater discharging into seawater-saturated sediments. The deeper-probing slingram soundings, on the other hand, could be fit quite well by a 1-D model. A representative example with RMS $\sim$22% is shown in (Figure 4.2b). While we acquired many 10 m$\times$10 m central loop soundings on the plains above the coastal bluffs, also none of them could be fit by a 1-D model, again indicating strong electrical heterogeneity at shallow depths. Interestingly, all soundings made along the plains transect comprised of 40 m$\times$40 m central loop soundings (described further below) could be fit by a 1-D model, a representative example with RMS $\sim$18% is shown in (Figure 4.2c). To summarize, none of the 10 m$\times$10 m central-loop soundings made either at the beach or on the adjacent plains could be fit by a 1-D model. In contrast, all of the slingram soundings on the beach and all of the 40 m$\times$40 m central-loop soundings on the plains could be fit by a 1-D model.

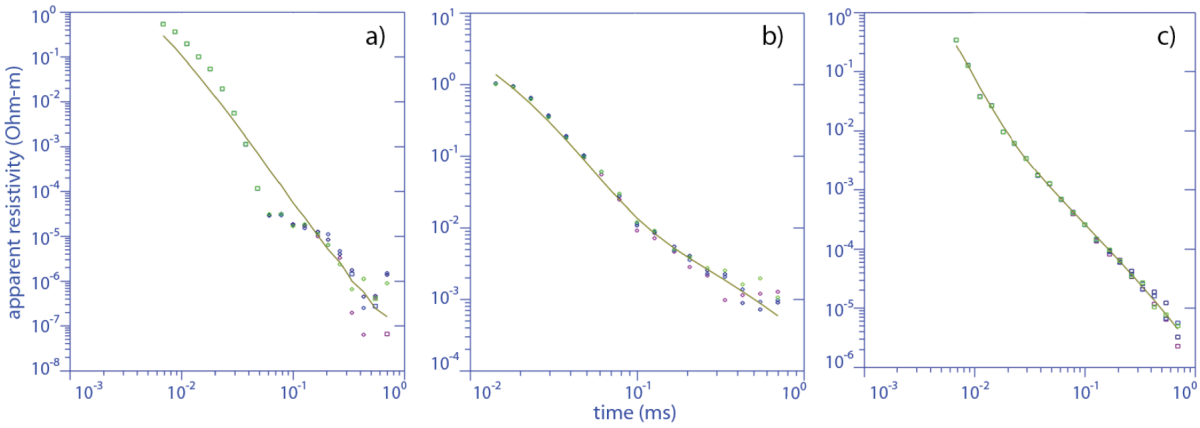

Figure 4.2: Representative data fits to the G-TEM sounding curves for (a) 10 m$\times$10 m central-loop sounding on the beach, (b) 10 m$\times$10 m slingram-mode on the beach, and (c) 40 m$\times$40 m central-loop soundings inland from the bluffs. Square symbols represent positive responses, whereas negative responses are displayed as diamond symbols. Reprinted from Weymer et al. [2020] with permission.

4.1.3.2 Integrated results

A primary research question in this study is to determine whether gravel lenses within the braided alluvial deposits beneath the Canterbury plain are groundwater conduits, potentially discharging offshore. To address this question, we compare results from collocated EMI, GPR, and G-TEM surveys conducted on the beachfront, along with a DEM of the study area [LINZ, 2019]. Complicating our exploration efforts, especially at shallow depths (e.g., < 10 m), is the effect of changing tides on the EM signals that we attempted to mitigate by conducting the surveys as far away as possible from the swash zone and by performing a series of calibration tests following the same procedure, as described in [Weymer et al., 2016], to gain better insight on interpreting the geophysical results.

A comparison of GPR profile D with a G-TEM transect along the final ∼185 m of the same path is shown in Figure 4.3. The resulting geoelectrical models are stitched together in a quasi-2D format in the figure. It can be seen that the G-TEM probes to depths ∼80 m, at which low resistivities indicative of clays and/or seawater-saturated sediments ρ ∼1–10 Ωm (green-orange-red colors) are found. Above these depths, the ground is more resistive, attaining values up to ρ = 100 Ωm (blue-purple colors). In the middle part of the section, at depths ∼20–30 m, there are a couple of zones that are somewhat less resistive (light blue color) than the surroundings. These zones are indicative of deep alongshore heterogeneity and are discussed below. Note the depth-ranges examined by the GPR (0–9 m) and G-TEM (∼10–80 m) in Figure 4.3 are largely non-overlapping and the near-surface (<10 m depth) structure is not well-resolved by the G-TEM.

To further illustrate the conductive zones onshore are most likely water-filled gravel conduits, we show an additional coast-normal G-TEM survey (Figure 3.6). The 40×40 m^2 G-TEM 1-D stitched section acquired on top of the cliffs (refer to Figure 4.1) reveals a consistent conductive zone at roughly 7–10 m depths. The resistivity of the conductive layer is about 150 Ωm (green region). This is slightly higher than the well water conductivity, but is to be expected in a gravel matrix. Because the conductive layer occurs at each station, at roughly the same depth, this suggests the conduit is continuous supporting the notion of a stream of freshwater discharge toward the

coast like a subterranean river. The fact that the 40×40 m^2 soundings could be fit by a 1-D model, unlike the 10×10 m^2 central-loop soundings, suggests that the deep conductive layer – unlike any shallower conduits – is quite broad, with a width that could be on the order of the instrument footprint. Thus, it is likely there is a considerable volume of deep flowing discharge towards the coast and offshore.

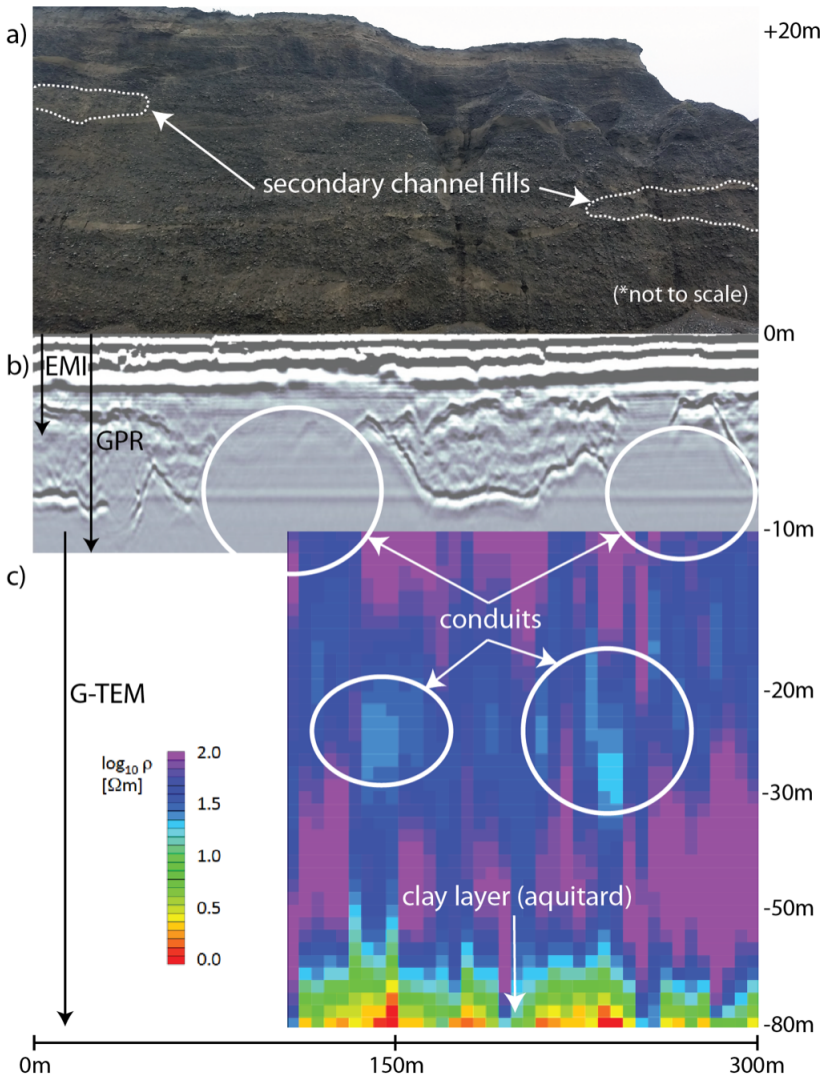

Figure 4.3: Composite depth slice from the top of the coastal bluff to the maximum depth of investigation probed by the G-TEM system. Secondary channel fills outlined in (a), extending into the subsurface, correspond to conductive zones that are outlined in the GPR section (b) and the inverted G-TEM section (c). Conductive zones illuminate the probable location of groundwater conduits and show evidence for a multilayered system. Reprinted from Weymer et al. [2020] with permission.

4.1.3.3 Deeper conduits connecting the onshore/offshore coastal groundwater system

The G-TEM results from the slingram survey along the coast (Figure 4.3) reveal two zones at ∼20–30 m depth of similar conductivities that were observed in nearby hydrogeological wells

(see Figure 4.1) averaging around 30 mS/m ($\sim$33 Ωm). These values are comparable to resistivities measured offshore [Micallef et al., 2020] that were interpreted to indicate the location of the offshore freshened groundwater (OFG) system. The overall agreement in conductivities measured both on land and at sea give the illusion that the conduits onshore are conductive, relative to the resistive geologic (dry gravels) background ($\sim$10 mS/m) and appear as resistors in the marine environment compared to the overall conductive background ($>$1000 mS/m).

Assuming the aquifer extends horizontally from the closest boreholes ($\sim$1 km inland) to the coast and that the elevation at the top of the coastal bluffs is $\sim$20 m, we expect a 20 m vertical offset between our G-TEM survey (at sea level) along the coast. By comparison, this would make the depth of the first confining layer (50 m) in [Davey, 2004] to 30 m in our data. Our data do not appear to show the first confining layer (at least in this particular area) because the conductivities are much lower than what would be expected for a clay layer/aquitard (Figure 4.3). Thus, we interpret these zones as groundwater conduits that are focusing flow offshore and are likely connected to the OFG system (Figure 4.4). The depth of the OFG system interpreted in Micallef et al. [2020] is slightly deeper, occurring at depths of 50 m or more. Marine seismic data show that the gravels extend further offshore in the region directly offshore the Ashburton coast i.e., the location of the surveys presented in this study. It is probable these gravel channels imaged in the offshore seismic data are connected to the coast, providing evidence for an onshore connection to the conduits/aquifers in the region. The high conductivity zone at 60–70 m is probably the second aquitard described by Davey [2004], but our interpretation is limited in resolution because the maximum depth of investigation of the G-TEM system is 80 m from the TX-RX configuration used in this study.

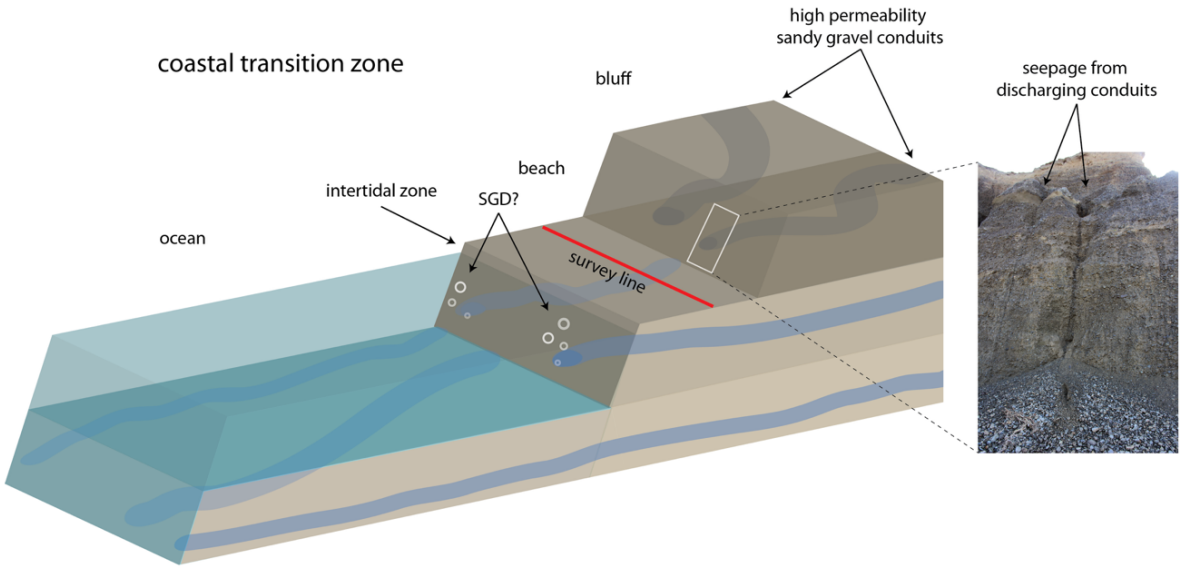

Figure 4.4: Conceptual discharge model illustrating the configuration of (from top to bottom): (1) high permeability sandy gravel conduits within the coastal bluffs and photograph from the field showing evidence for seepage on the bluff face, (2) shallow conduits in the unconfined aquifer potentially discharging in the nearshore at SGD sites, and (3) deeper conduits connecting the on-shore/offshore coastal groundwater system. Reprinted from Weymer et al. [2020] with permission.

4.2 Groundwater erosion of coastal gullies along the Canterbury coast (New Zealand): A rapid and episodic process controlled by rainfall intensity and substrate variability

All contents in the section 4.2 are from the article[3] submitted to open-access journal *Earth Surface Dynamics.*

4.2.1 Authors

Aaron Micallef[a,b,*], Remus Marchis[c], Nader Saadatkhah[1], **Potpreecha Pondthai**[d], Mark E. Everett[d], Anca Avram[e,f], Alida Timar-Gabor[e,f], Denis Cohen[b], Rachel Preca Trapani[b], Bradley A. Weymer[a], Phillipe Wernette[g]

[a] GEOMAR–Helmholtz Centre for Ocean Research, Kiel, Germany

[3]Reprinted with permission from Micallef, A., Marchis, R., Saadatkhah, N., Pondthai, P., Everett, M. E., Avram, A., Timar-Gabor, A., Cohen, D., Trapani, R. P., Weymer, B. A. & Wernette, P. (in review). Groundwater erosion of coastal gullies along the Canterbury coast (New Zealand): A rapid and episodic process controlled by rainfall intensity and substrate variability. *Earth Surface Dynamics.*

[b] Marine Geology and Seafloor Surveying, Department of Geosciences, University of Malta, Malta

[c] Department of Geological Sciences, University of Canterbury, Christchurch, New Zealand

[d] Department of Geology and Geophysics, Texas A&M University, Texas, United States

[e] Faculty of Environmental Science and Engineering, Babes-Bolyai University, Cluj-Napoca, Romania

[f] Interdisciplinary Research Institute on Bio-Nano-Sciences, Babeş-Bolyai University, Cluj-Napoca, Romania

[g] School of the Environment, University of Windsor, Ontario, Canada.

4.2.2 Abstract

Gully formation has been associated to groundwater seepage in unconsolidated sand to gravel sized sediments. Our understanding of gully evolution by groundwater seepage mostly relies on experiments and numerical simulations, and these rarely take into consideration contrasts in lithology and permeability. In addition, process-based observations and detailed instrumental analyses are rare. As a result, we have a poor understanding of the temporal scale of gully formation by groundwater seepage and the influence of geological heterogeneity on their formation. This is particularly the case for coastal gullies, where the role of groundwater in their formation and evolution has rarely been assessed. We address these knowledge gaps along the Canterbury coast of the South Island (New Zealand) by integrating field observations, optically stimulated luminescence dating, multi-temporal Unoccupied Aerial Vehicle and satellite data, time-domain electromagnetic data, and slope stability modelling. We show that gully formation is a key process shaping the sandy gravel cliffs of the Canterbury coastline. It is an episodic process associated to groundwater flow that occurs once every 227 days on average, when rainfall intensities exceed 40 mm per day. The majority of the gullies in a study area SE of Ashburton has undergone erosion, predominantly by elongation, during the last 11 years, with the most recent episode occurring 3 years ago. Gullies longer than 200 m are relict features formed by higher groundwater flow and surface erosion >2 ka ago. Gullies can form at rates of up to 30 m per day via two processes: the formation of alcoves

and tunnels by groundwater seepage, followed by retrogressive slope failure due to undermining and a decrease in shear strength driven by excess pore pressure development. The location of gullies is determined by the occurrence of hydraulically-conductive zones, such as relict braided river channels and possibly tunnels, and of sand lenses exposed across sandy gravel cliff. We also show that gully planform shape is generally geometrically similar at consecutive stages of evolution. These outcomes will facilitate reconstruction and prediction of a prevalent erosive process and overlooked geohazard along the Canterbury coastline.

4.2.3 Contributions as Co-Author

I collected the geophysical data and provided time-gate plots to explore the spatial connection between the lateral fluctuation of the EM responses with temporal geomorphic changes.

4.2.3.1 Near-surface geophysics surveys

Time-domain electromagnetic (TDEM) measurements were carried out in May 2019 using the Geonics G-TEM system (Figure 4.5b). The operating principles of the inductive TEM technique are described in Nabighian and Macnae [1991] and Fitterman [2015]. The survey parameters included 4 turns, a 10×10 m square TX loop, and a TX current output of 1 A. The G-TEM was operated in slingram mode, in which the RX coil was placed 30 m from the centre of the TX loop and the TX-RX pair moved together along a linear transect at 2 m station spacing, maintaining the 30 m offset. The maximum depth of investigation of the G-TEM system is given approximately by the formula:

$$d = 8.94 L^{0.4} \rho^{0.25} \tag{4.1}$$

where L (m) is the TX loop size and ρ (Ωm) is the upper layer resistivity [Geonics, 2016]. Setting ρ = 100 Ωm yields a depth of investigation of d = 71 m, whereas ρ = 1000 Ωm yields d = 126 m. Our investigation depth in New Zealand may be slightly greater than these values since the Geonics formula assumes a 1-turn TX loop carrying current 3 A, whereas we used a more powerful combination of 4 turns at 1.5 A. At each station, a consistent 1-D smooth model of electrical resistivity vs. depth was performed based on the iterative Occam-regularised inversion

method [Constable et al., 1987] and using IXG-TEM commercial software [Interpex, 2012]. This is a standard 1-D TDEM inversion code that has been successfully used for coastal hydrogeophysical studies (e.g. [Pondthai et al., 2020]).

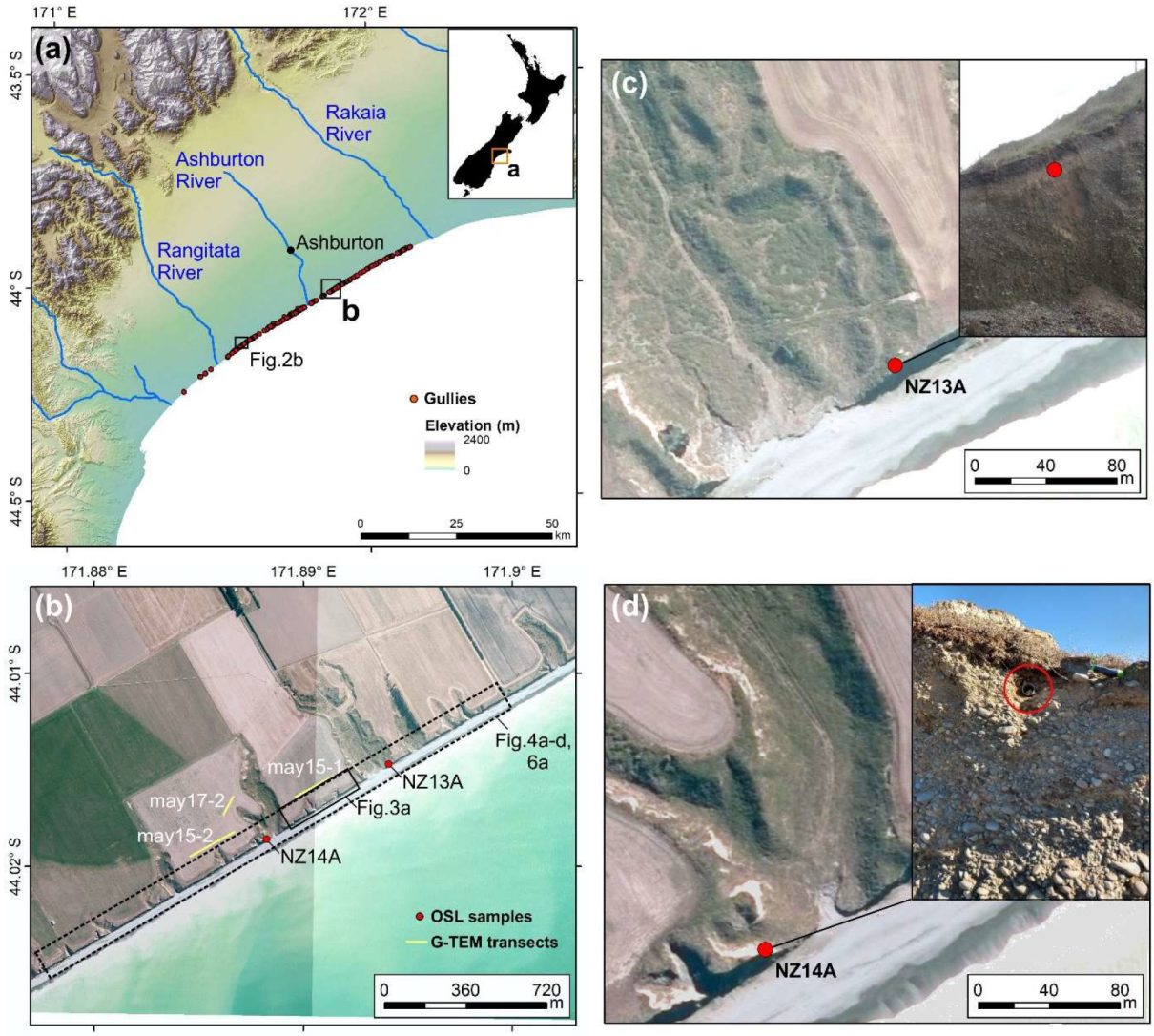

Figure 4.5: (a) Digital elevation model of the Canterbury Plains (source: Environment Canterbury), located along the eastern coast of the South Island of New Zealand, showing the location of mapped gullies. Location of figure is shown in inset. (b) Mosaic of aerial photographs of the study area (source: Environment Canterbury). Location of Optically Stimulated Luminescence (OSL) samples, G-TEM transects, and other figures is shown. (c-d) Zoomed sections of the aerial photograph and site photographs of the OSL sampling sites NZ13A and NZ14A. Reprinted from Micallef et al. [in review] with permission.

4.2.3.2 Geophysical data and results

The location of the G-TEM transects is shown in Figure 4.5b. An attempt was made to invert the G-TEM slingram mode responses with 30-m TX-RX offset using 1-D Occam inversion. A representative inversion result is shown in Figure 4.6a. The resistivity model is presented in the right panel, whereas the corresponding model-response with the actual data points is shown on the left. The best calculated smooth depth profile clearly does not fit well with the measured signal and there is excessive structure in the $\sim$10–20 m depth range, including the very low resistivity layer ($\sim 10^{-4}$ Ωm) at depths in excess of $\sim$12–15 m. The resistivity values between 40 and 100 m depth are lower than sea water resistivity (0.3 Ωm), which is not reasonable. The inability to fit a 1-D model to the slingram responses suggests that the geoelectrical sub-surface structure is strongly heterogeneous within the footprint of the G-TEM transmitter. As a result, we cannot trust 1-D inversions of the slingram-mode data in such a 3-D geological environment. We did not try to use the 1-D inversion software to further analyse and interpret the G-TEM data. However, even though the individual slingram-mode responses cannot be fit reliably by a 1-D model, we can still analyse lateral changes in the observed response curves along the slingram profiles to reveal information about subsurface heterogeneity; this is elaborated below.

Instead of performing 1-D inversions, we present time-gate plots for all three transects. A time-gate plot is defined as a graph of the observed G-TEM voltage response, evaluated at a particular time-gate, as a function of position along a profile. Time-gate plots are a useful alternative to explore the lateral variability of the G-TEM response along a profile in the event that the sounding curves at individual stations cannot be fit with 1-D models. It is presumed that variability in a time-gate plot is correlated with lateral heterogeneity in the subsurface geoelectrical structure, since a 1-D Earth structure would yield no spatial variability in a time-gate plot. Specifically, the amplitude of the G-TEM slingram response (in units of 10^{-10} V/m^2) at the first time-gate is plotted as a function of station number along a profile. Figure 4.6b displays a 1-D model (A) that contains a conductive layer of 100 Ωm between 10-20 m depths in a homogeneous 1000 Ωm background. The 1-D model (A) in Figure 4.6b is motivated by the inversion results of deep-penetrating

40×40 m TX loop TDEM soundings carried out on top of the cliffs several tens of metres inland [Weymer et al., 2020], which revealed such a conductive zone at these depths. Unlike the slingram profiles, the deeper-penetrating, larger-loop sounding curves are readily fit by a 1-D model. This model generates a G-TEM slingram response that has a substantially larger ramp-off voltage amplitude at all time gates than does the model (B) without the conductive layer, as shown in Figure 4.6b. Thus we regard an enhancement of response at the first time gate as indicative of a conductive zone at depth beneath the slingram station. The spatial analysis of time-gate plots is not a conventional approach in TDEM, but it is somewhat analogous to the spatial analysis of apparent resistivity profiles in frequency-domain EM using terrain conductivity meters [Weymer et al., 2016]. This is based on the idea that the G-TEM response at a fixed time-gate carries information similar to that of a terrain conductivity meter response at a fixed frequency.

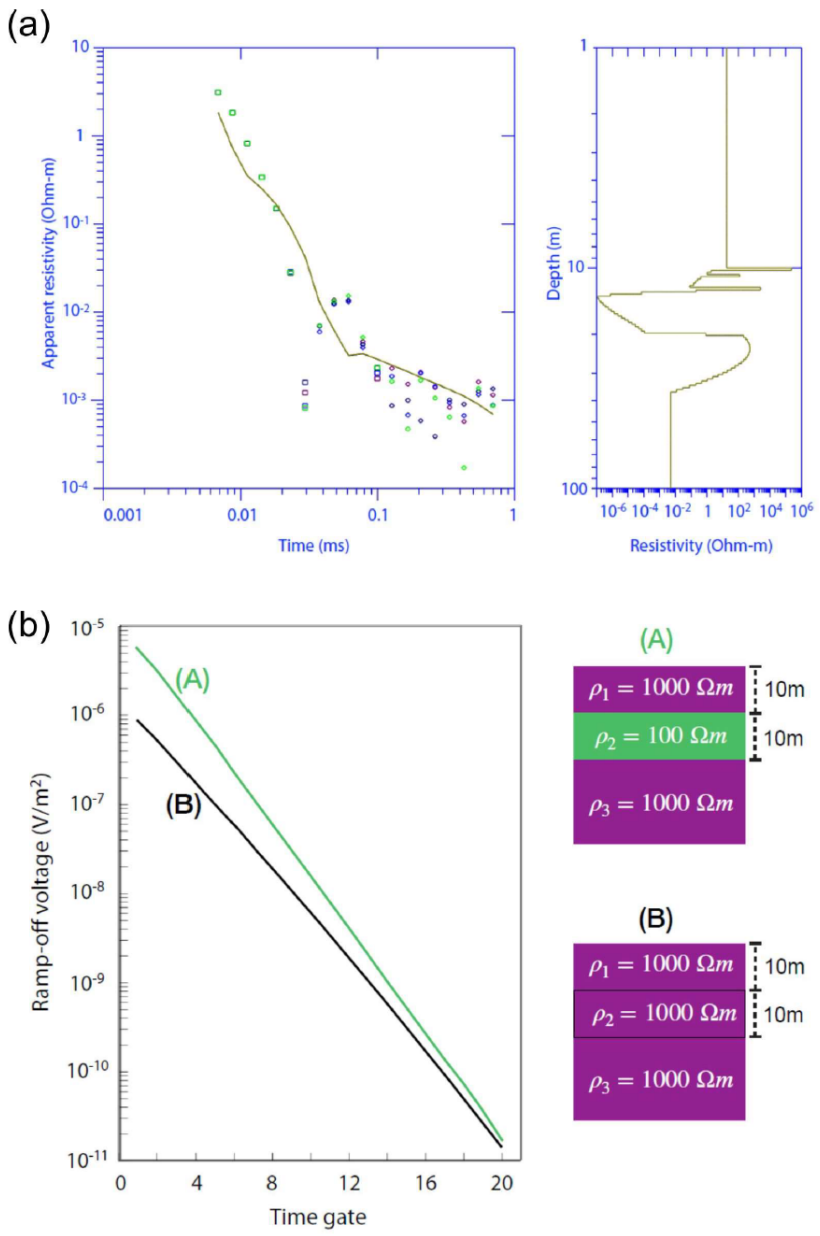

Figure 4.6: (a) 1-D inversion result for data at a station located 6 m from start of Profile May15-1; location can be referred from Figure 4.5b. (b) G-TEM slingram responses for model (A) containing a conductive zone at a depth of 10–20 m, and for model (B) without the conductive zone. Reprinted from Micallef et al. [in review] with permission.

The first-time-gate profile of transect May15-1 is located upslope of small but recently eroded gullies (Figure 4.7a). In this figure, the 'first-time-gate profile' is a plot as a function of distance along the transect of the G-TEM ramp-off voltage at time gate number 1, at the first sampled point

of the transient response immediately after the TX current has been switched off. Near the middle of this transect there is a distinctive peak that is much higher than the background. The peak is ∼20–30 m wide and it appears in a similar fashion on each of the gates 1 through 7 (not shown here), although it cannot be clearly observed after gate 7. Transect May 15-2 is located upslope of recently eroded gullies in the south-west and relatively less active gullies in the north-east of the investigated area (Figure 4.7b). Lateral variations are evident along the 192 m length of the profile. The high amplitude response at the start of the profile (going from the south-west to north-east) is followed by a drop in amplitude near the midpoint of the profile, following which there is continuous fluctuation at a lower amplitude until the end of the profile. The time-gate plots for gates 2 to 7 remain similar in shape to that of the time-gate-1 plot and hence are not shown. After time-gate 7, the time-gate plots start to lose coherence due to the low signal-to-noise ratio of the decaying received voltage at late times after TX ramp-off. G-TEM slingram profile May17-2 was acquired upslope of the tributary of a large gully covered by mature vegetation (Figure 4.7c). The size and location of this gully have been persistent over recent years, in contrast to the neighbouring, smaller gullies that are under active development. Transect May 17-2 shows a lower amplitude response in comparison to the previous two transects (Figure 4.7c).

Based on all three profiles, a general observation that can be made is that the first-time-gate amplitude of the slingram response is higher upslope at the more recently active gullies.

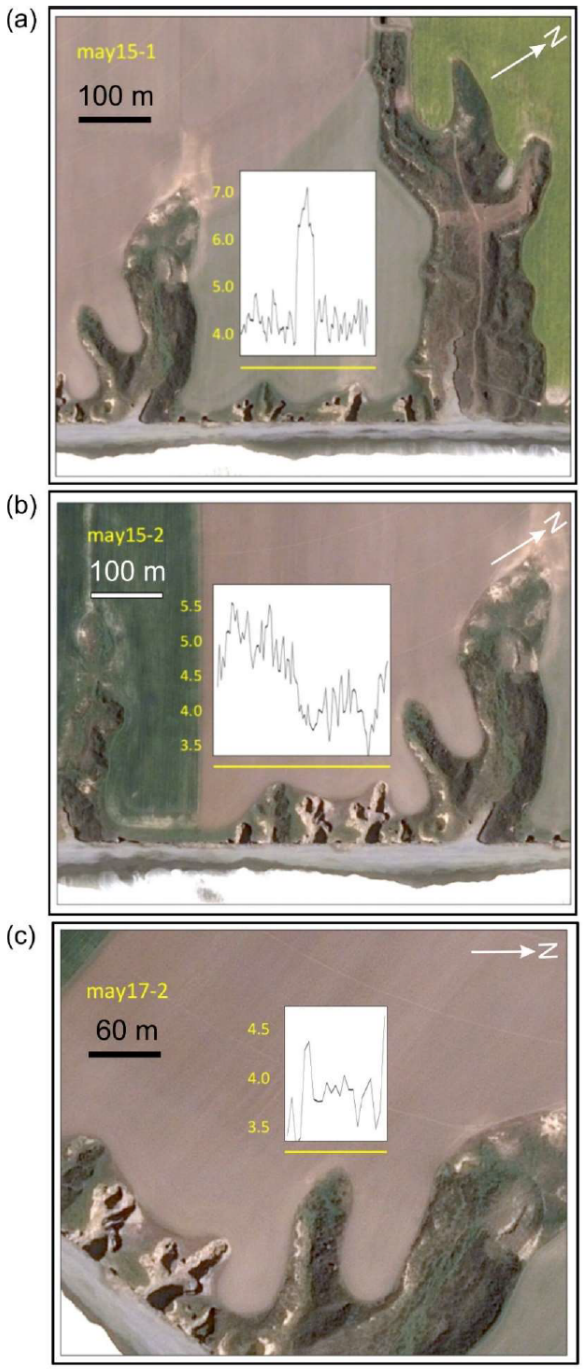

Figure 4.7: (First-time-gate profiles of G-TEM slingram transects (a) May15-1, (b) May 15-2, and (c) May17-2 (units in yellow are 10^{-10} V m^{-2}). Source of background imagery: Google, Maxar Technologies. A yellow line marks a slingram transect, the length of which can be determined from the scale bar. Reprinted from Micallef et al. [in review] with permission.

4.2.3.3 Identification of Location of Coastal Gullies using G-TEM

Gullies are characteristic landforms along the Canterbury coast (Figure 4.5a). They are an important driver of coastal geomorphic change as well as loss of agricultural land. The factor that controls the location of gullies is a hydraulically-conductive zone upslope of the gully is supported by geophysical observations. With regards to the G-TEM slingram time-gate plots (Figure 4.7), we interpret the higher-amplitude responses on the time-gate-1 plots that are preferentially located upslope of recently active gullies as zones of relatively high electrical conductivity in the subsurface at depths of $\sim$10 m. These zones are suggestive of buried groundwater conduits made up of gravel and/or sandy units (e.g. Weymer et al., 2020), or tunnels formed by subsurface groundwater flow in sand units. Further analysis of the G-TEM data, including 2-D modelling and inversion, is required to ascertain the subsurface hydraulic geometry responsible for the along-profile amplitude variations. The above observations confirm the importance of spatial variations in hydrogeological properties as a factor controlling the location of a gully. This had initially been suggested by [Dunne et al., 1990] and has been documented for gullies in bedrock environments [Laity and Malin, 1985, Newell, 1970]. Development of gullies downslope of permeable conduits may also explain why most of the erosion entails elongation of existing gullies, rather than formation of new ones (Figure 4.8 and 4.9). It also agrees with the results of experimental modelling by [Berhanu et al., 2012], which suggest that channels grow preferentially at their tip when the groundwater flow is driven by an upstream flow. If seaward-directed groundwater conduits are responsible for the location of gullies, as the G-TEM results predict that, along the Canterbury coast, we should generally observe active gully development downslope of peaks in slingram time-gate plots. If this is the case, G-TEM could be used to identify locations of incipient and even future gully development.

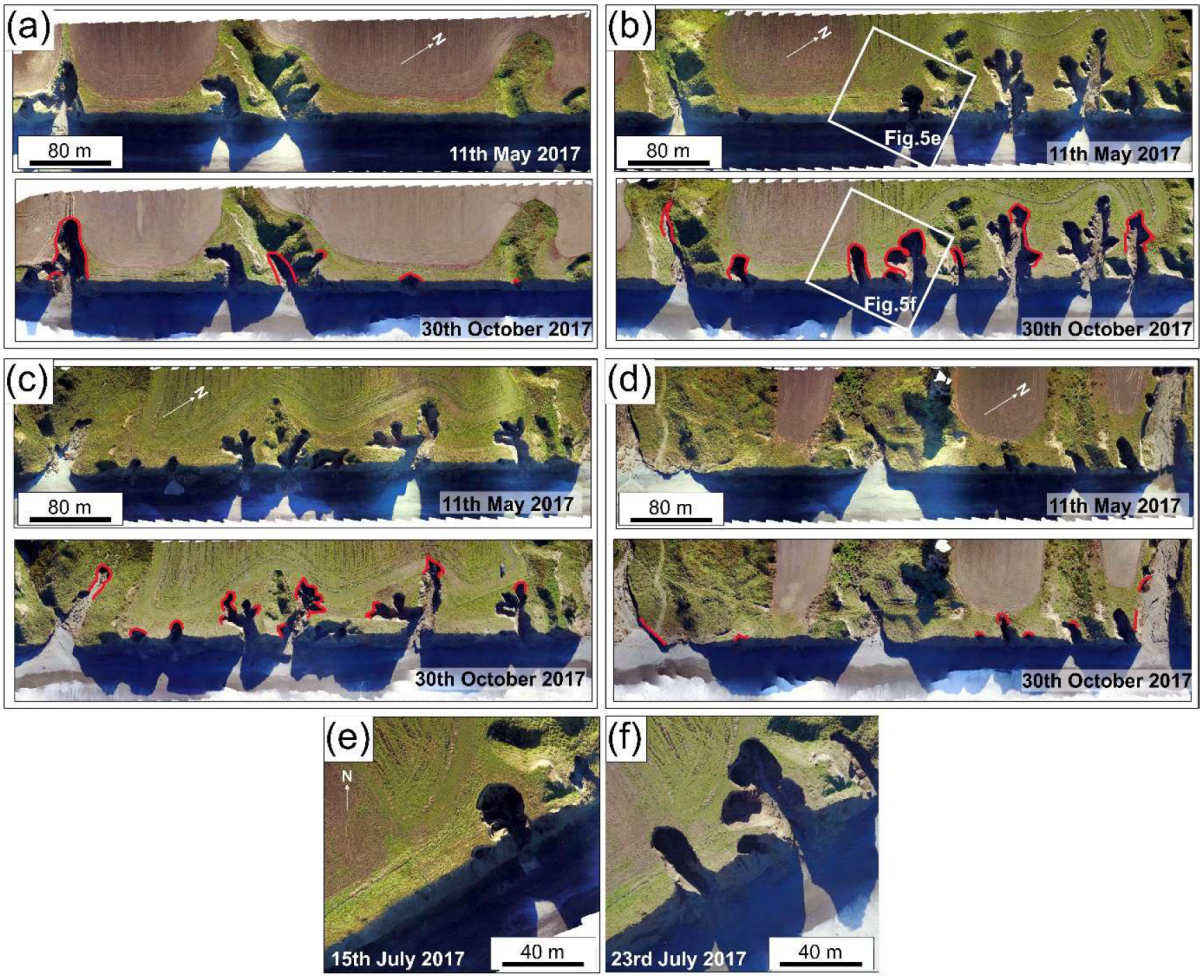

Figure 4.8: (a-d) Orthophotographs of the study area at the start and end of the UAV surveys, ordered from south-west to north-east; refer to Figure 4.5b for location. Red lines mark eroded areas. Orthophographs from a part of the study area on the (e) July 15^{th}, 2017 and the (f) July 23^{rd}, 2017. Reprinted from Micallef et al. [in review] with permission.

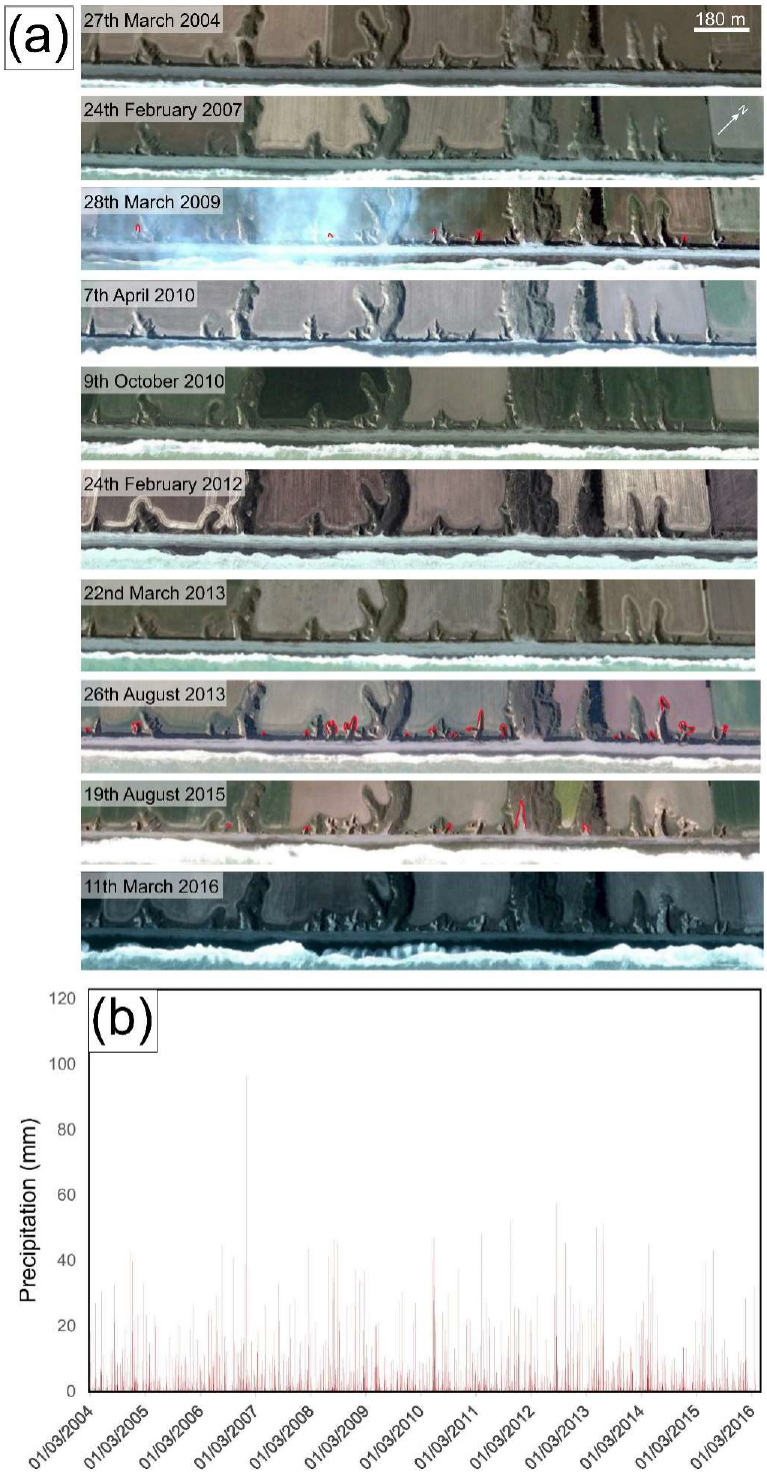

Figure 4.9: (a) Satellite imagery of the study area between the March 27^{th}, 2004 and March 11^{th}, 2016 (source: Google, Maxar Technologies). Eroded areas are marked by red lines. (b) Daily precipitation record for this period for Ashburton Council (source: Environment Canterbury). Reprinted from Micallef et al. [in review] with permission.

5. SUMMARY

This dissertation has described realistic modeling related to imaging onshore-offshore aquifer hydraulic connections and potential groundwater flow paths using a terrestrial inductively-coupled loop source electromagnetic (EM) technique. Near-surface time-domain electromagnetic (TDEM) data were collected using the Geonics G-TEM equipment in the central-loop and slingram-mode configurations. Forward modeling of TDEM responses for subsurface structures has previously been widely used for environmental, hydrological investigations, but rarely in 2-D and 3-D geometries. Geophysical TDEM methods play a prominent role in coastal studies since electrical resistivity is related to important hydrological parameters such as porosity, water saturation, and salinity. The key physical principle is the inductive EM process, which is equivalent to diffusion of an image of the transmitter (TX) loop current into a conducting medium. Unknown connections between onshore and offshore aquifer have been found in many places worldwide. The two locations where I have tested their possible connectivity including the southeastern coast of Malta Island and the eastern coast of the South Island of New Zealand.

A 3D finite element (FE) algorithm used to compute the EM responses is modified from earlier work. The algorithm that solves the governing Maxwell's equations is formulated in terms of Coulomb-gauged potentials in the frequency domain. Previous versions of the program have been validated for 1D, 2D and 3D structures but are capable of calculating responses for only a single frequency at a time. Distribution of subsurface geological structures are assigned dimensions, locations, and conductivities to simple slab-like regions. The code I modified enables the FE algorithm to compute a series of multi-frequency solutions spanning several decades in a single step. I also implemented original codes using an inverse Fourier transform algorithm in order to convert frequency-domain responses into transient response that are directly comparable with the corresponding field measurements.

In chapter 2, the mean sea-level aquifer (MSLA) extension offshore along the coastline of SE Malta is investigated. An image of the geometry and location of the onshore mean sea-level aquifer

within the permeable limestone formations along the SE Malta coast is depicted. 2D and 3D resistivity models are found by iterative adjustments of FE forward modeling from the terrestrial TDEM data based on fieldwork conducted in summer 2018 and 2019. The final 3D forward model provides information to depth of 60 m and shows diagnostic spatial variations in subsurface electrical resistivity. The geophysical modeling helps to better understand the important characteristics of the MSLA that fit field observations such as the decreasing thickness of fresh groundwater bodies towards the coastline. Zones of fresh groundwater have been identified, but these are located preferentially inland from the coast. Thus, there is no indication from the electromagnetic data of a robust offshore extension of the MSLA. However, it is worth mentioning that similar methods can be applied across the entire Maltese archipelago to better constrain the geometry, dimensions and distribution of terrestrial and coastal aquifers. This should provide valuable information for future water management of the stressed groundwater reserves of Malta.

In chapter 3, G-TEM slingram-mode measurements at the Canterbury plains are used to investigate the character and location of freshwater discharge along the Ashburton coast, New Zealand. 2D forward-modeling of TDEM data helps to answer whether groundwater flows in shallow concentrated conduits that are spatially coincident with geomorphic features such as the coastal gullies. Possible scenarios for a groundwater discharge model that matches the G-TEM observations along upslope profile are explored. The model derived from one of the inland TDEM datasets shows that the subsurface geoelectrical distribution is characterized by distinct conducive zones under the plains. These conductive zones in the lower plains are likely caused by relatively fresh water-saturated secondary channel fills that focus groundwater flow offshore under the coastal bluffs. The spatial relationship between the locations of eroded coastal gullies and the G-TEM inferred locations of shallow and deeper groundwater discharge conduits beneath the braidplain alluvial sediments provide evidence of a seepage system that focuses groundwater flow through preferential pathways.

In chapter 4, a stitched 1D resistivity profile up to 80 m deep constructed from a 185 m G-TEM slingram-mode survey conducted in 2019 along the Ashburton beach of the same surveyed

EMI and GPR lines previously collected in 2018 reveals two conductive zones at $\sim$25 m depth. These conductive zones are interpreted as onshore groundwater conduits (gravel channels) that focus flow offshore and may be connected to to the resistive geological background in the offshore environment determined from a recent marine CSEM survey. In addition, three transects of G-TEM slingram data were carried out inland across the heads of coastal gullies on the eastern part of Canterbury plains. It is presumed that the variability of the observed response in the time-gate plot corresponds to lateral heterogeneity in the geoelectrical structure. Based on the first-time-gate profiles for all three transects, a general observation that can be made is that the higher first-time-gate amplitude of the slingram response is preferentially located upslope of recently active gullies, and manifests as zones of relatively high electrical conductivity in the subsurface at depths of $\sim$10 m. These zones are suggestive of buried groundwater conduits comprised of gravel and/or sandy units or else tunnels formed by sub-surface groundwater flow in sand units. Assuming that seaward-directed groundwater conduits are associated with the location of coastal gullies, as the G-TEM results predict, we should generally observe active gully development downslope of the peaks in slingram time-gate plots.

Future work and recommendations are provided in following list.

1. To make available a 3D inversion for land-based TDEM soundings.

2. To extend the TDEM data acquisition into the coastal transition zone (shallow water).

3. To provide information and collaborate with hydrologic modelers to develop hydrological models to explain geophysics results.

4. To test the TDEM imaging method in different places to determine potential sites for onshore-offshore aquifer connectivity (i.e., Prince Edward Island (Canada), La Paz (Mexico), and New Jersey (USA)) and to further examine the connection between groundwater conduits and coastal gullies (e.g., Alaska (USA), Florida Panhandle (USA), Kalahari (South Africa), and Obara area (Japan)).

REFERENCES

[Ansari and Farquharson, 2014] Ansari, S. and Farquharson, C. G. (2014). 3d finite-element forward modeling of electromagnetic data using vector and scalar potentials and unstructured grids. *Geophysics*, 79(4):E149–E165.

[Archie, 1942] Archie, G. (1942). Electrical resistivity log as an aid in determining some reservoir characteristics. *Transactions of the American Institute of Mining and Metallurgical Engineers*, 164:322–323.

[Auken et al., 2003] Auken, E., Jørgensen, F., and Sørensen, K. I. (2003). Large-scale tem investigation for groundwater. *Exploration Geophysics*, 34(3):188–194.

[Badea et al., 2001] Badea, E. A., Everett, M. E., Newman, G. A., and Biro, O. (2001). Finite element analysis of controlled source electromagnetic induction using coulomb-gauged potentials. *Geophysics*, 66:786–799.

[Bakalowicz and Mangion, 2003] Bakalowicz, M. and Mangion, J. (2003). The limestone aquifers of malta: Their recharge conditions from isotope and chemical surveys. *International Association of Hydrological Sciences, Publication*, (278):49–54.

[Bal, 1996] Bal, A. A. (1996). Valley fills and coastal cliffs buried beneath an alluvial plain: evidence from variation of permeabilities in gravel aquifers, canterbury plains, new zealand. *Journal of Hydrology (New Zealand)*, pages 1–27.

[Batayneh, 2008] Batayneh, A. T. (2008). Horizontal-loop electromagnetic signature of a buried dike, al quweira area, southwest jordan. *Geophysical prospecting*, 49(5):540–546.

[Beres et al., 1995] Beres, M., Green, A., Huggenberger, P., and Horstmeyer, H. (1995). Mapping the architecture of glaciofluvial sediments with three-dimensional georadar. *Geology*, 23(12):1087–1090.

[Berhanu et al., 2012] Berhanu, M., Petroff, A., Devauchelle, O., Kudrolli, A., and Rothman, D. H. (2012). Shape and dynamics of seepage erosion in a horizontal granular bed. *Physical Review E*, 86(4):041304.

[Bowling et al., 2005] Bowling, J. C., Rodriguez, A. B., Harry, D. L., and Zheng, C. (2005). Delineating alluvial aquifer heterogeneity using resistivity and gpr data. *Groundwater*, 43(6):890–903.

[Bratton, 2010] Bratton, J. F. (2010). The three scales of submarine groundwater flow and discharge across passive continental margins. *The Journal of Geology*, 118(5):565–575.

[BRGM, 1991] BRGM (1991). Study of the fresh water resources of malta. Technical report, Appendix 7: Water Quality and EnvironmentalAspects, R 33691 EAU 4S 91, BRGM, Orleans.

[Bridge and Lunt, 2006] Bridge, J. S. and Lunt, I. A. (2006). Depositional models of braided rivers. In *Braided rivers: Process, deposits, ecology and management*, volume 36, pages 11–50. Blackwell Publishing Oxford.

[Browne and Naish, 2003] Browne, G. H. and Naish, T. R. (2003). Facies development and sequence architecture of a late quaternary fluvial-marine transition, canterbury plains and shelf, new zealand: implications for forced regressive deposits. *Sedimentary Geology*, 158(1-2):57–86.

[Burnett et al., 2003] Burnett, W. C., Bokuniewicz, H., Huettel, M., Moore, W. S., and Taniguchi, M. (2003). Groundwater and pore water inputs to the coastal zone. *Biogeochemistry*, 66(1-2):3–33.

[Burnett et al., 2001] Burnett, W. C., Taniguchi, M., and Oberdorfer, J. (2001). Measurement and significance of the direct discharge of groundwater into the coastal zone. *Journal of Sea Research*, 46(2):109–116.

[Canterbury, 2019] Canterbury, E. (2019). Environment canterbury regional council: New zealand – river flow data. http://www.ecan.govt.nz/data/riverflow (accessed on 1 September 2020).

[Chave, 1983] Chave, A. D. (1983). Numerical integration of related hankel transforms by quadrature and continued fraction expansion. *Geophysics*, 48:1671–1686.

[Collins and Sitar, 2009] Collins, B. D. and Sitar, N. (2009). Geotechnical properties of cemented sands in steep slopes. *Journal of Geotechnical and Geoenvironmental Engineering*, 135(10):1359–1366.

[Collins and Sitar, 2011] Collins, B. D. and Sitar, N. (2011). Stability of steep slopes in cemented sands. *Journal of geotechnical and geoenvironmental engineering*, 137(1):43–51.

[Constable et al., 1987] Constable, S. C., Parker, R. L., and Constable, C. G. (1987). Occam's inversion: A practical algorithm for generating smooth models from electromagnetic sounding data. *Geophysics*, 52(3):289–300.

[Costabel et al., 2017] Costabel, S., Siemon, B., Houben, G., and Günther, T. (2017). Geophysical investigation of a freshwater lens on the island of langeoog, germany–insights from combined hem, tem and mrs data. *Journal of Applied Geophysics*, 136:231–245.

[Danielsen et al., 2003] Danielsen, J. E., Auken, E., Jørgensen, F., Søndergaard, V., and Sørensen, K. I. (2003). The application of the transient electromagnetic method in hydrogeophysical surveys. *Journal of applied geophysics*, 53(4):181–198.

[Davey, 2004] Davey, G. (2004). Aquidef, a ms access programme to define canterbury plains aquifers and aquitards.

[Davey, 2006] Davey, G. (2006). *Definition of the Canterbury Plains aquifers*. Environment Canterbury.

[Directorate, 1993] Directorate, O. E. (1993). Geological map of the maltese islands. *Office of the Prime Minister, Valletta*.

[Dunne et al., 1990] Dunne, T. et al. (1990). Hydrology, mechanics, and geomorphic implications of erosion by subsurface flow. In *Groundwater Geomorphology: The Role of Subsurface Water in Earth-Surface Processes and Landforms*, volume 252, pages 1–28.

[El-Kaliouby and Abdalla, 2015] El-Kaliouby, H. and Abdalla, O. (2015). Application of time-domain electromagnetic method in mapping saltwater intrusion of a coastal alluvial aquifer, north oman. *Journal of Applied Geophysics*, 115:59–64.

[Evans, 2007] Evans, R. L. (2007). Using csem techniques to map the shallow section of seafloor: From the coastline to the edges of the continental slope. *Geophysics*, 72(2):WA105–WA116.

[Everett, 2012] Everett, M. E. (2012). Theoretical developments in electromagnetic induction geophysics with selected applications in the near surface. *Geophysics*, 33:29–63.

[Everett, 2013] Everett, M. E. (2013). *Near-surface applied geophysics*. Cambridge University Press.

[Everett and Chave, 2019a] Everett, M. E. and Chave, A. D. (2019a). Energy flow in terrestrial controlled-source electromagnetic geophysics. *European Journal of Physics*, 40(6):065202.

[Everett and Chave, 2019b] Everett, M. E. and Chave, A. D. (2019b). On the physical principles underlying electromagnetic induction. *Geophysics*, 84:W21–W32.

[Ezersky and Frumkin, 2017] Ezersky, M. G. and Frumkin, A. (2017). Evaluation and mapping of dead sea coastal aquifers salinity using transient electromagnetic (tem) resistivity measurements. *Comptes Rendus Geoscience*, 349(1):1–11.

[FAO, 2006] FAO (2006). Malta water resources review.

[Fitterman, 1987] Fitterman, D. V. (1987). Examples of transient sounding for ground-water exploration in sedimentary aquifers. *Ground Water*, 25(6):685–692.

[Fitterman, 2015] Fitterman, D. V. (2015). *Tools and Techniques: Active-Source Electromagnetic Methods*, chapter Resourcesin the Near-Surface Earth, Treatise on Geophysics, pages 295–333.

[Fitterman and Hoekstra, 1984] Fitterman, D. V. and Hoekstra, P. (1984). Mapping of saltwater intrusion with transient electromagnetic soundings. In *Proceeding of the NWWA/EPA Conference on Surface and Borehole Geophysical Methods in Ground Water Investigations*, pages 429–454.

[Fitterman and Stewart, 1986] Fitterman, D. V. and Stewart, M. T. (1986). Transient electromagnetic sounding for groundwater. *Geophysics*, 51:995–1005.

[Flatman, 1997] Flatman, M. R. (1997). Cliff erosion and coastal change, mid canterbury. M.S. Thesis, University of Canterbury.

[Flores and Peralta-Ortega, 2009] Flores, C. and Peralta-Ortega, S. A. (2009). Induced polarization with in-loop transient electromagnetic soundings: A case study of mineral discrimination at el arco porphyry copper, mexico. *Journal of Applied Geophysics*, 68(3):423–436.

[Galdies, 2011] Galdies, C. (2011). *The Climate of Malta: Statistics, Trends and analysis, 1951-2010, National Statistics Office, Malta*.

[Ge et al., 2012] Ge, J., Everett, M. E., and Weiss, C. J. (2012). Fractional diffusion analysis of the electromagnetic field in fractured media part i: 2d approach. *Geophysics*, 77(4):WB213–WB218.

[Ge et al., 2015] Ge, J., Everett, M. E., and Weiss, C. J. (2015). Fractional diffusion analysis of the electromagnetic field in fractured media—part 2: 3d approach. *Geophysics*, 80(3):E175–E185.

[Geonics, 2016] Geonics (2016). *G-TEM Operating Manual*. Mississauga, ON, Canada.

[Goldman et al., 1991] Goldman, M., Gilad, D., Ronen, A., and Melloul, A. (1991). Mapping of seawater intrusion into the coastal aquifer of israel by the time domain electromagnetic method. *Geoexploration*, 28(2):153–174.

[Guptasarma and Singh, 2003] Guptasarma, D. and Singh, B. (2003). New digital linear filters for hankel j0 and j1 transforms [link]. *Geophysical prospecting*, 45(5):745–762.

[Gustafson et al., 2019] Gustafson, C., Key, K., and Evans, R. L. (2019). Aquifer systems extending far offshore on the us atlantic margin. *Scientific reports*, 9(1):1–10.

[Hathaway et al., 1979] Hathaway, J. C., Poag, C. W., Valentine, P. C., Manheim, F. T., Kohout, F. A., Bothner, M. H., Miller, R. E., Schultz, D. M., and Sangrey, D. A. (1979). Us geological survey core drilling on the atlantic shelf. *Science*, 206(4418):515–527.

[Herckenrath et al., 2013] Herckenrath, D., Odlum, N., Nenna, V., Knight, R., Auken, E., and Bauer-Gottwein, P. (2013). Calibrating a salt water intrusion model with time-domain electromagnetic data. *Groundwater*, 51(3):385–397.

[Huber and Huggenberger, 2016] Huber, E. and Huggenberger, P. (2016). Subsurface flow mixing in coarse, braided river deposits. *Hydrology & Earth System Sciences*, 20(5).

[Illies, 1981] Illies, J. H. (1981). Graben formation the maltese islands a case history. *Tectonophysics*, 73:151–168.

[Interpex, 2012] Interpex (2012). *IXG-TEM Instruction Manual*.

[Jahandari and Farquharson, 2014] Jahandari, H. and Farquharson, C. G. (2014). A finite-volume solution to the geophysical electromagnetic forward problem using unstructured grids. *Geophysics*, 79(6):E287–E302.

[Jennings and Shulmeister, 2002] Jennings, R. and Shulmeister, J. (2002). A field based classification scheme for gravel beaches. *Marine Geology*, 186(3-4):211–228.

[Jiao and Post, 2019] Jiao, J. and Post, V. (2019). *Coastal hydrogeology*. Cambridge University Press.

[Johannes, 1980] Johannes, R. (1980). The ecological significance of the submarine discharge of groundwater. *Marine Ecology Progress Series*, pages 365–373.

[Jones et al., 2019] Jones, E., Qadir, M., van Vliet, M. T., Smakhtin, V., and Kang, S.-m. (2019). The state of desalination and brine production: A global outlook. *Science of the Total Environment*, 657:1343–1356.

[Kafri et al., 1997] Kafri, U., Goldman, M., and Lang, B. (1997). Detection of subsurface brines, freshwater bodies and the interface configuration in-between by the time domain electromagnetic method in the dead sea rift, israel. *Environ. Geol*, 31:42–49.

[Kalisperi et al., 2018] Kalisperi, D., Kouli, M., Vallianatos, F., Soupios, P., Kershaw, S., and Lydakis-Simantiris, N. (2018). A transient electromagnetic (tem) method survey in north-central coast of crete, greece: Evidence of seawater intrusion. *Geosciences*, 8:107.

[Kamm et al., 2013] Kamm, J., Becken, M., and Pedersen, L. B. (2013). Inversion of slingram electromagnetic induction data using a born approximation. *Geophysics*, 78(4):E201–E212.

[Kaufman et al., 1983] Kaufman, A. A., Keller, G. V., et al. (1983). Frequency and transient soundings. *Chi-Yu King Roberto Scarpa*, 207(7).

[Kline et al., 2014] Kline, S. W., Adams, P. N., and Limber, P. W. (2014). The unsteady nature of sea cliff retreat due to mechanical abrasion, failure and comminution feedbacks. *Geomorphology*, 219:53–67.

[Kooi and Groen, 2001] Kooi, H. and Groen, J. (2001). Offshore continuation of coastal groundwater systems; predictions using sharp-interface approximations and variable-density flow modelling. *Journal of Hydrology*, 246(1-4):19–35.

[Laity and Malin, 1985] Laity, J. E. and Malin, M. C. (1985). Sapping processes and the development of theater-headed valley networks on the colorado plateau. *Geological Society of America Bulletin*, 96(2):203–217.

[Li et al., 2017] Li, J., Farquharson, C. G., and Hu, X. (2017). 3d vector finite-element electromagnetic forward modeling for large loop sources using a total-field algorithm and unstructured tetrahedral grids. *Geophysics*, 82(1):E1–E16.

[Li et al., 2020] Li, J., Li, Y., Liu, Y., Spitzer, K., and Han, B. (2020). 3-d marine csem forward modeling with general anisotropy using an adaptive finite-element method. *IEEE Geoscience and Remote Sensing Letters*.

[Li et al., 2018] Li, J., Lu, X., Farquharson, C. G., and Hu, X. (2018). A finite-element time-domain forward solver for electromagnetic methods with complex-shaped loop sources. *Geophysics*, 83(3):E117–E132.

[LINZ, 2019] LINZ (2019). Land information new zealand. https://www.linz.govt.nz (accessed on 2 August 2020).

[Lippert and Tezkan, 2019] Lippert, K. and Tezkan, B. (2019). On the exploration of a marine aquifer offshore israel by long-offset transient electromagnetics. *Geophysical Prospecting*, 68(3):999–1015.

[Lu, 2020] Lu, X. (2020). Three-dimensional finite-volume time-domain modeling of graphitic fault zones in the athabasca basin using unstructured grids. Ph.D. Thesis, Memorial University of Newfoundland.

[Maher, 1992] Maher, M. (1992). Transient electromagnetic surveys in the okiep district. *Geophysics*, 57(5):736–744.

[Malta and Authority, 2003] Malta, E. and Authority, P. (2003). Minerals subject plan for the maltese islands 2002. Entec UK Ltd.: London, UK.

[Malta and Authority, 2011] Malta, E. and Authority, P. (2011). The water catchment management plan for the maltese islands. Malta Environment and Planning Authority and the Malta Resources Authority: Marsa, Malta. https://era.org.mt/en/Documents/1st%20WCMP_final.pdf (accessed on 16 January 2020).

[Mangion and Sapiano, 2008] Mangion, J. and Sapiano, M. (2008). 19 the mean sea level aquifer, malta and gozo. *Natural Groundwater Quality*, page 404.

[MARCAN, 2020] MARCAN (2020). Topographically-driven meteoric groundwater an important geomorphic agent. http://www.marcan.eu/objectives.html (accessed on 20 September 2020).

[MARSOL, 2015] MARSOL (2015). Demonstrating managed aquifer recharge as a solution to water scarcity and drought characterisationof the sea-level aquifer system in the malta south region. Institution of Applied Geosciences: Darmstadt, Germany. http://www.marsol.eu/files/marsold10-1msla-characterisation.pdf (accessed on 11 January 2020.

[MARSOL, 2016] MARSOL (2016). Demonstrating managed aquifer recharge as a solution to water scarcity and drought characterisation of the sea-level aquifer system in the malta south region. Institution of Applied Geosciences: Darmstadt, Germany. http://www.marsol.eu/files/marsold10-4malta-groundwater-model.pdf (accessed on 14 January 2020).

[Martin-Nagle, 2020] Martin-Nagle, R. (2020). Offshore freshwater aquifers: Toward equitable distribution. *Wiley Interdisciplinary Reviews: Water*, page e1463.

[Martínez-Moreno et al., 2017] Martínez-Moreno, F., Monteiro-Santos, F., Bernardo, I., Farzamian, M., Nascimento, C., Fernandes, J., Casal, B., and Ribeiro, J. (2017). Identifying seawater intrusion in coastal areas by means of 1d and quasi-2d joint inversion of tdem and ves data. *Journal of Hydrology*, 552:609–619.

[Meju et al., 2000] Meju, M., Fenning, P., and Hawkins, T. (2000). Evaluation of small-loop transient electromagnetic soundings to locate the sherwood sandstone aquifer and confining formations at well sites in the vale of york, england. *Journal of Applied Geophysics*, 44(2-3):217–236.

[Micallef et al., 2013] Micallef, A., Foglini, F., Bas, T. L., Angeletti, L., Maselli, V., Pasuto, A., and Taviani, M. (2013). The submerged paleolandscape of the maltese islands: Morphology, evolution and relation to quaternary environmental change. *Marine Geology*, 335:129–147.

[Micallef et al., 2020] Micallef, A., Person, M., Haroon, A., Weymer, B. A., Jegen, M., Schwalenberg, K., Faghih, Z., Duan, S., Cohen, D., Mountjoy, J. J., et al. (2020). 3d characterisation and quantification of an offshore freshened groundwater system in the canterbury bight. *Nature communications*, 11(1):1–15.

[Micallef et al., view] Micallef, A., Timar, A., Marchis, R., Saadatkhah, N., Clavera-Gispert, R., Pondthai, P., Everett, M. E., Avram, A., Timar-Gabor, A., Cohen, D., Trapani, R. P., and Weymer, B. A. (in-review). Groundwater erosion of coastal gullies along the canterbury coast

(new zealand): A rapid and episodic process controlled by rainfall intensity and substrate variability. *Earth Surface Dynamics*.

[Michael et al., 2016] Michael, H. A., Scott, K. C., Koneshloo, M., Yu, X., Khan, M. R., and Li, K. (2016). Geologic influence on groundwater salinity drives large seawater circulation through the continental shelf. *Geophysical Research Letters*, 43(20):10–782.

[Moore, 1996] Moore, W. S. (1996). Large groundwater inputs to coastal waters revealed by 226 ra enrichments. *Nature*, 380(6575):612–614.

[Moreton et al., 2002] Moreton, D. J., Ashworth, P., and Best, J. L. (2002). The physical scale modelling of braided alluvial architecture and estimation of subsurface permeability. *Basin Research*, 14(3):265–285.

[Morgan et al., 2018] Morgan, L. K., Werner, A. D., and Patterson, A. E. (2018). A conceptual study of offshore fresh groundwater behaviour in the perth basin (australia): Modern salinity trends in a prehistoric context. *Journal of Hydrology: RegionalStudies*, 19:318–334.

[Nabighian and Macnae, 1991] Nabighian, M. N. and Macnae, J. C. (1991). *6. Time Domain Electromagnetic Prospecting Methods*, chapter Electromagnetic Methods in Applied Geophysics, pages 427–520.

[Newell, 1970] Newell, M. (1970). Canyonlands—modern history. *Naturalist*, 21:40–47.

[Nielsen et al., 2007] Nielsen, L., Jørgensen, N. O., and Gelting, P. (2007). Mapping of the freshwater lens in a coastal aquifer on the keta barrier (ghana) by transient electromagnetic soundings. *Journal of Applied Geophysics*, 62(1):1–15.

[Okazaki et al., 2013] Okazaki, H., Nakazato, H., and Kwak, Y. (2013). Application of high-frequency ground penetrating radar to the reconstruction of 3d sedimentary architecture in a flume model of a fluvial system. *Sedimentary Geology*, 293:21–29.

[Pedley et al., 1976] Pedley, H. M., House, M. R., and Waugh, B. (1976). The geology of malta and gozo. *Proc. Geol. Ass*, 87:325–341.

[Person et al., 2003] Person, M., Dugan, B., Swenson, J. B., Urbano, L., Stott, C., Taylor, J., and Willett, M. (2003). Pleistocene hydrogeology of the atlantic continental shelf, new england. *Geological Society of America Bulletin*, 115(11):1324–1343.

[Pondthai et al., 2020] Pondthai, P., Everett, M. E., Micallef, A., Weymer, B. A., Faghih, Z., Haroon, A., and Jegen, M. (2020). 3d characterization of a coastal freshwater aquifer in se malta (mediterranean sea) by time-domain electromagnetics. *Water*, 12(6):1566.

[Porsani et al., 2012] Porsani, J. L., Bortolozo, C. A., Almeida, E. R., Sobrinho, E. N. S., and Dos Santos, T. G. (2012). Tdem survey in urban environmental for hydrogeological study at usp campus in são paulo city, brazil. *Journal of Applied Geophysics*, 76:102–108.

[Post, 2005] Post, V. (2005). Fresh and saline groundwater interaction in coastal aquifers: is our technology ready for the problems ahead? *Hydrogeology Journal*, 13(1):120–123.

[Post et al., 2013] Post, V. E., Groen, J., Kooi, H., Person, M., Ge, S., and Edmunds, W. M. (2013). Offshore fresh groundwater reserves as a global phenomenon. *Nature*, 504(7478):71–78.

[Rey et al., 2013] Rey, J., Martínez, J., and Hidalgo, M. (2013). Investigating fluvial features with electrical resistivity imaging and ground-penetrating radar: The guadalquivir river terrace (jaen, southern spain). *Sedimentary Geology*, 295:27–37.

[Rizzo, 2020] Rizzo, E. (2020). personal communication. https://hyfrew.wordpress.com (accessed on 1 May 2020).

[Santos et al., 2008] Santos, I. R., Niencheski, F., Burnett, W., Peterson, R., Chanton, J., Andrade, C. F., Milani, I. B., Schmidt, A., and Knoeller, K. (2008). Tracing anthropogenically driven groundwater discharge into a coastal lagoon from southern brazil. *Journal of Hydrology*, 353(3-4):275–293.

[Sasaki and Meju, 2006] Sasaki, Y. and Meju, M. A. (2006). A multidimensional horizontal-loop controlled-source electromagnetic inversion method and its use to characterize heterogeneity in aquiferous fractured crystalline rocks. *Geophysical Journal International*, 166(1):59–66.

[Schumm and Phillips, 1986] Schumm, S. and Phillips, L. (1986). Composite channels of the canterbury plain, new zealand: A martian analog? *Geology*, 14(4):326–329.

[Scott, 1980] Scott, G. (1980). Near-surface hydraulic stratigraphy of the canterbury plains between ashburton and rakaia rivers, new zealand. *Journal of Hydrology (New Zealand)*, pages 68–74.

[Siemon et al., 2009] Siemon, B., Christiansen, A. V., and Auken, E. (2009). A review of helicopter-borne electromagnetic methods for groundwater exploration. *Near Surf. Geophys*, 7:629–646.

[Smith, 2014] Smith, R. (2014). Electromagnetic induction methods in mining geophysics from 2008 to 2012. *Surveys in Geophysics*, 35(1):123–156.

[Sørensen and Auken, 2004] Sørensen, K. I. and Auken, E. (2004). Skytem-a new high-resolution helicopter transient electromagnetic system. *Exploration Geophysics*, 35(3):191–199.

[Spies, 1989] Spies, B. R. (1989). Depth of investigation in electromagnetic sounding methods. *Geophysics*, 54(7):872–888.

[Stalnaker et al., 2006] Stalnaker, J. L., Everett, M. E., Benavides, A., and Pierce, C. J. (2006). Mutual induction and the effect of host conductivity on the em induction response of buried plate targets using 3-d finite-element analysis. *IeeeTransactions on Geoscience and Remote Sensing*, 44:251–259.

[Stewart and Gay, 1983] Stewart, M. T. and Gay, M. C. (1983). *Evaluation of a Ground Transient Electromagnetic Remote Sensing Method for the Deep Detection and Monitoring of Salt Water Interfaces*. Florida Water Resources Research Center.

[Streich, 2016] Streich, R. (2016). Controlled-source electromagnetic approaches for hydrocarbon exploration and monitoring on land. *Surveys in geophysics*, 37(1):47–80.

[Stuart et al., 2010] Stuart, M., Maurice, L., Heaton, T., Sapiano, M., Sultana, M. M., Gooddy, D., and Chilton, P. (2010). Groundwater residence time and movement in the maltese islands – a geochemical approach. *Applied Geochemistry*, 25(5):609–620.

[Tabbagh, 1986] Tabbagh, A. (1986). Applications and advantages of the slingram electromagnetic method for archaeological prospecting. *Geophysics*, 51(3):576–584.

[Talley et al., 2003] Talley, D. M., North, E. W., Juhl, A. R., Timothy, D. A., Conde, D., Jody, F., Brown, C. A., Campbell, L. M., Garstecki, T., Hall, C. J., et al. (2003). Research challenges at the land–sea interface. *Estuarine, Coastal and Shelf Science*, 58(4):699–702.

[Taniguchi et al., 2002] Taniguchi, M., Burnett, W. C., Cable, J. E., and Turner, J. V. (2002). Investigation of submarine groundwater discharge. *Hydrological Processes*, 16(11):2115–2129.

[Torres-Martinez et al., 2019] Torres-Martinez, J. A., Mora, A., Ramos-Leal, J. A., Morán-Ramírez, J., Arango-Galván, C., and Mahlknecht, J. (2019). Constraining a density-dependent flow model with the transient electromagnetic method in a coastal aquifer in mexico to assess seawater intrusion. *Hydrogeology Journal*, 27(8):2955–2972.

[Ward and Hohmann, 1988] Ward, S. H. and Hohmann, G. W. (1988). Electromagnetic theory for geophysical applications. In *Electromagnetic Methods in Applied Geophysics: Voume 1, Theory*, pages 130–311. Society of Exploration Geophysicists.

[Weymer et al., 2016] Weymer, B. A., Everett, M. E., Houser, C., Wernette, P., and Barrineau, P. (2016). Differentiating tidal and groundwater dynamics from barrier island framework geology: Testing the utility of portable multifrequency electromagnetic induction profilers. *Geophysics*, 81(5):E347–E361.

[Weymer et al., 2020] Weymer, B. A., Wernette, P. A., Everett, M. E., Pondthai, P., Jegen, M., and Micallef, A. (2020). Multi-layered high permeability conduits connecting onshore and offshore coastal aquifers. *Frontiers in Marine Science*.

[Wilson, 1973] Wilson, D. (1973). The significance of geology in some current water resource problems, canterbury plains, new zealand. *Journal of Hydrology (New Zealand)*, pages 103–118.

[Wright and Short, 1984] Wright, L. D. and Short, A. D. (1984). Morphodynamic variability of surf zones and beaches: a synthesis. *Marine geology*, 56(1-4):93–118.

[Yogeshwar and Tezkan, 2017] Yogeshwar, P. and Tezkan, B. (2017). Two-dimensional basement modeling of central loop transient electromagnetic data from the central azraq basin area, jordan. *Journal of Applied Geophysics*, 136:198–210.

[Yu and Michael, 2019] Yu, X. and Michael, H. A. (2019). Offshore pumping impacts onshore groundwater resources and land subsidence. *Geophysical Research Letters*, 46:2553–2562.